

Search for a tensor component in the weak interaction Hamiltonian

CERN-THESIS-2013-437
10/07/2013



Gergely Sóti

Dissertation presented in partial
fulfillment of the requirements for the
degree of Doctor in Sciences

July 2013

Search for a tensor component in the weak interaction Hamiltonian

Gergely SÓTI

Supervisory Committee:

Prof. dr. Mark Huyse, chair

Prof. dr. N. Severijns, supervisor

Prof. dr. Valeri Afanasiev

Prof. dr. Riccardo Raabe

Prof. dr. Kazimierz Bodek

(Jagiellonian University, Krakow, Poland)

dr. Stephanie Rocca

(CSNSM, IN2P3-CNRS, Univ. Paris-Sud,
Orsay Campus, France)

Dissertation presented in partial
fulfillment of the requirements for
the degree of Doctor
in Sciences

July 2013

© KU Leuven – Faculty of Science
Celestijnenlaan 200D box 2418, B-3001 Heverlee (Belgium)

Alle rechten voorbehouden. Niets uit deze uitgave mag worden vermenigvuldigd en/of openbaar gemaakt worden door middel van druk, fotocopie, microfilm, elektronisch of op welke andere wijze ook zonder voorafgaande schriftelijke toestemming van de uitgever.

All rights reserved. No part of the publication may be reproduced in any form by print, photoprint, microfilm or any other means without written permission from the publisher.

D/2013/10.705/55
ISBN 978-90-8649-640-2

Acknowledgments

The four-year-long journey has come to an end, an end that is also a beginning. I find it therefore appropriate to thank all the people who helped me during this journey.

I am greatly indebted to my promoter Nathal Severijns, for all that he taught me about LTNO, precision and errors, and physics in general. Our discussions were always a source of motivation to push further and attack every “issue” that surfaced during my PhD studies.

I am also thankful to the members of the jury: Valerie Afanasiev, Kazimierz Bodek, Mark Huyse, Riccardo Raabe, Stephanie Rocchia and once more Nathal Severijns for their effort of reading the thesis and providing me with valuable suggestions.

It was great pleasure to be a member of the KO/WI group. I would like to thank Frederik for introducing me to the field, Emil for all the lab-related work and Véronique for the theoretical discussions. I would also like to thank Dalibor for all the detector-related work. Thanks are due to the past and present members of the wider WI group as well: Stephanie, Janne, Elise, Michaël, Simon, Martin, Tomica, Paul and Andreas.

Thanks to the IKS administrative and technical team as well: Martine, Fabienne, Isabelle, Sally, Nancy, Luc, Bert, Dries and Willy. Furthermore, I would also like to thank all the IKS members for the Alma lunches and the pleasant working atmosphere.

I am thankful for the support of my friends, both in Leuven and in Serbia; my family for their love and encouragement during my journey. Finally, I would like to thank my wife for our home, for all the “sudden” trips and for her constant love and support.

Gergely

June 2013, Leuven

Abstract

The search for physics beyond the standard model can, besides in high-energy experiments such as the ones at the LHC accelerator, also be carried out at lower energies. Measurements of correlation coefficients in neutron and nuclear β decay constitute a reliable and model-independent method for such efforts.

The topic of this thesis is the precision measurement of the β asymmetry parameter A . It was measured in the decay of ^{67}Cu , which proceeds via a pure Gamow-Teller β transition, thus its A parameter is sensitive to possible tensor type currents in the weak interaction. The experiment was performed at the NICOLE setup in ISOLDE (CERN), using the technique of low temperature nuclear orientation. The β particles were observed with custom made planar high purity germanium detectors operating at around 10 K. The β asymmetry of ^{68}Cu was measured on-line for normalization purposes.

Geant4 simulations were used to gain control over systematic effects such as electron scattering on the particle detectors. As the simulations play such a crucial role in the analysis procedure their quality and reliability was investigated in great detail. Therefore experimental spectra of different radioactive isotopes measured with germanium and silicon detectors are compared to simulated ones. Based on the results, the optimal Geant4 physics model was determined together with fine-tuning the value of several simulation parameters.

The experimental result for the β asymmetry parameter of ^{67}Cu is $\tilde{A} = 0.584(10)$, in agreement with the standard model prediction of $A_{SM} = 0.5998(2)$ when taking into account recoil, radiative and Coulomb corrections. This is one of the most accurate determinations of this parameter to date. The limits obtained for the time-reversal invariant tensor coupling constants are $-0.002 < (C_T + C'_T)/C_A < 0.100$ (90% C.L.) and these are competitive with limits from other measurements of correlations in neutron and nuclear β decay.

Analysis of the error budget of this and previous experiments employing the low temperature nuclear orientation technique leads us to conclude that the

inherent limitations of this technique have been reached. In order to remain competitive as other experiments are approaching the sub-percent precision, a new technique is being developed, i.e. precision β spectrum shape measurements. Its sensitivity to physics beyond the standard model is via the Fierz interference term. Combining a scintillator detector with a multi-wire drift chamber a backscatter-free β spectrum can be obtained. By again choosing a pure Gamow-Teller transition of low endpoint energy the Fierz interference term can be determined with sub percent precision. Part of the feasibility study for this new project is described here as well.

Beknopte samenvatting

De zoektocht naar fysica buiten het standaard model kan, behalve met hoogenergetische experimenten zoals die in de LHC versneller, ook uitgevoerd worden bij lagere energieën. Het meten van correlatie coëfficiënten in neutron en nucleair β verval is een betrouwbare en modelonafhankelijke methode hiervoor.

Het onderwerp van deze thesis is de precisie meting van de β asymmetrie parameter A . De meting gebeurde met het isotoop ^{67}Cu , dat vervalft via een pure Gamov-Teller overgang, zodat zijn A parameter gevoelig is voor mogelijke tensorstromen in de zwakke interactie. Het experiment gebeurde met de NICOLE set-up in ISOLDE (CERN), waarbij gebruik gemaakt werd van kernoriëntatie bij lage temperaturen. De β deeltjes werden geregistreerd met op maat gemaakte dunne germanium detectoren van hoge zuiverheid, die gekoeld werden tot ongeveer 10 K. De β asymmetrie van ^{68}Cu werd eveneens opgemeten voor normalisatie doeleinden.

Geant4 simulaties werden gebruikt om controle te krijgen over systematische effecten zoals bijvoorbeeld verstrooiing van de elektronen aan de detectoren. Omdat simulaties een cruciale rol spelen in de analyse procedure, werd hun kwaliteit en betrouwbaarheid zorgvuldig bestudeerd. Hiervoor werden de experimentele spectra van verscheidene radioactieve isotopen, opgemeten met germanium en silicium detectoren, vergeleken met simulaties. Op basis van de resultaten en het precies afstemmen van verscheidene parameters in de simulatiecode werd het optimale Geant4 fysica model bepaald.

Het experimentele resultaat voor de β asymmetrie parameter van ^{67}Cu is $\tilde{A} = 0.584(10)$. Dit valt binnen de standaard model voorspelling van $A_{SM} = 0.5998(2)$ als er rekening wordt gehouden met terugstoot, stralings- en coulombcorrecties. Dit is een van de meest nauwkeurige bepalingen van deze parameter tot op vandaag. De verkregen limieten voor de tijdsinvariante tensor koppelingsconstanten zijn $0.002 < (C_T + C'_T)/C_A < 0.100$ (90% C.L.) en deze zijn competitief met limieten van andere metingen van correlaties in het neutron

en nucleair β verval.

Uit analyse van de foutenmarge van deze en vorige lage temperatuur kernoriëntatie experimenten kan besloten worden dat de inherente beperkingen van deze techniek bereikt zijn. Om competitief te blijven met andere experimenten, die de sub-procent precisie benaderen, werd daarom een nieuwe techniek ontwikkeld, namelijk precisie β spectrum vorm metingen. Via de Fierz interferentieterm is de β spectrum vorm eveneens gevoelig voor fysica buiten het standaard model. Door de combinatie van een scintillatiedetector en een dradenkamer, kan een verstrooiingsvrij β spectrum worden verkregen. Door opnieuw een pure Gamov-Teller overgang met lage eindpuntenergie te selecteren, kan de Fierz interferentie tot op sub-procent precisie bepaald worden. Een deel van de haalbaarheidsstudie voor dit nieuwe project wordt hier ook beschreven.

Contents

Abstract	iii
Contents	vii
1 Introduction	1
2 Nuclear β decay, a brief overview	3
2.1 Beta decay in the Standard Model	3
2.1.1 GWS theory of electroweak interaction	4
2.1.2 The Hamiltonian of Lee and Yang	5
2.2 Beyond the Standard Model	12
2.2.1 Constrains from LHC	12
2.2.2 Left-right symmetric models	14
2.2.3 Search for tensor currents	15
2.2.4 Experimental status	15
3 Low Temperature Nuclear Orientation	19
3.1 Formalism	20
3.1.1 Angular distribution	21
3.1.2 Orientation mechanism	21

3.1.3	Nuclear relaxation	22
3.1.4	Deorientation	25
3.1.5	Fraction	26
3.1.6	Solid angle effects	26
3.2	Experimental setup	27
3.2.1	Dilution refrigerators	28
3.2.2	Magnetic field	29
3.2.3	Detectors	30
3.2.4	Thermometry	31
4	Geant4 Monte Carlo simulations	33
4.1	Introduction to Geant4	34
4.1.1	Simulation parameters	36
4.2	Article I	37
5	The β asymmetry parameter of ^{67}Cu	63
6	Measurement of the β spectrum shape	99
6.1	Introduction	100
6.1.1	Shape of the β spectrum	101
6.1.2	Fierz interference term	105
6.1.3	Recoil corrections	106
6.2	Experimental requirements	108
6.3	Detector response	111
6.4	Setup	117
6.4.1	Operating principle	119
6.5	Which isotope to measure?	120
6.5.1	Recoil terms	120

6.5.2 Fierz term	121
6.6 Geant4 improvements	122
7 Conclusions	125
A Decay schemes	127
Bibliography	131
List of publications	145

Chapter 1

Introduction

The physicists' way of describing nature is by the usage of models, which are mathematical constructions related to real-world observations. A *good* model not only describes and explains known facts, but also makes several falsifiable predictions. It often happens that a model fails to explain some experimental evidence. In such a case the model is either:

- discarded, e.g. the plum pudding model of the atom;
- extended, e.g. the Rutherford model of the atom was extended and became the Bohr model;
- limited, e.g. the Newtonian mechanics is limited to cases where the speeds of objects are much smaller than the speed of light.

A very successful model in the field of nuclear and particle physics is the Standard Model. It is under constant development since its birth in the middle of the last century. This model describes the world around us at the smallest scale, in terms of 12 fundamental particles: 6 leptons and 6 quarks. The interaction of these particles is modeled by the electroweak and the strong interactions; gravity is not included yet. All of the predicted fundamental particles together with the gauge bosons of the interactions have been experimentally observed in past experiments. The elusive Higgs boson is also believed to be observed at the CMS and ATLAS experiments located in CERN.

Despite the past and present success of the Standard Model, there are several hints that it is not a final theory. One of them is the presence of a vast amount of free parameters, such as particle masses or mixing angles. Furthermore, it

fails to account for several experimental observations, such as the nature of dark matter or the matter-antimatter balance in the universe. The shortcomings of the Standard Model point at the existence of an underlying, more fundamental model. The search for this new physics is carried out at many frontiers. At high energy accelerators particles not included in the Standard Model can be directly produced. Competitive results can also be obtained at the low energy frontier by precision measurements of different experimental observables. Correlation measurements in nuclear β decay also fall into this category of experiments, as they are sensitive to the structure of the weak interaction Hamiltonian.

The topic of this thesis is the precision measurement of the β asymmetry parameter A . It was measured in the decay of ^{67}Cu , which proceeds via a pure Gamow-Teller β transition, thus its A parameter is sensitive to possible tensor type currents in the weak interaction. The low temperature nuclear orientation (LTNO) technique was used to measure this parameter. The experiment was performed at the NICOLE setup in ISOLDE, CERN. The results provide limits on possible tensor type charged currents in the weak interaction Hamiltonian.

Chapter 2 introduces the formalism used in nuclear correlation measurements and also gives a summary of current experimental efforts in this field. In chapter 3 the experimental technique is discussed. As the data analysis procedure relied heavily on Geant4 simulations, chapter 4 is devoted to this topic. The description of the experiment and the results obtained are included in chapter 5 in the form of an article. The analysis of the error budget of this and previous experiments carried out by our group indicates that the inherent limits of the LTNO technique have been reached. A novel method to search for physics beyond the Standard Model is outlined in chapter 6.

Chapter 2

Nuclear β decay, a brief overview

2.1 Beta decay in the Standard Model

Nuclear β decay is the process of emission or capture of a β particle by a nucleus with the emission of an (anti)neutrino. On the nucleon level, the three different types commonly observed are:

- β^- decay: $n \rightarrow p + e^- + \bar{\nu}_e$
- β^+ decay: $p \rightarrow n + e^+ + \nu_e$
- electron capture: $p + e^- \rightarrow n + \nu_e$

Further, depending on the spins J , isospins T and parities π of the mother and the daughter nuclei involved, so-called allowed and forbidden transitions are considered. The allowed transitions are further classified into Fermi and Gamow-Teller transitions, as shown in table 2.1. Transitions where parity change is involved or where the spin change is larger than 1 are called forbidden. A common way of characterizing a β transition is by its $\log ft$ value which depends on weak interaction constants, the energy and the momentum of the β particle and the nuclear matrix elements responsible for the transition, while its experimental determination involves the measurement of the Q_{EC} value, the branching ratio and the half-life of the transition. Its value is around 3-4 for superallowed (pure Fermi) transitions, while for other allowed transitions it

falls between 4 and 6.8. Forbidden decays have even higher $\log ft$ values, up to about 13.

	Fermi	Gamow-Teller
ΔJ	0	0, ± 1 ($0 \nrightarrow 0$)
ΔT	0	0, ± 1 ($0 \nrightarrow 0$)
$\pi_i \pi_f$	+	+

Table 2.1: Selection rules of the Fermi and Gamow-Teller type allowed β transitions.

2.1.1 GWS theory of electroweak interaction

In the framework of the Standard Model, nuclear β decay is described by the unified electroweak interaction developed by Glashow, Weinberg and Salam [1, 2]. The electroweak interaction is based on gauge theory, which yields four massless bosons. Three of them gain mass via the symmetry breaking of the scalar Higgs field becoming the W^+ , W^- and Z^0 bosons, while the fourth, massless boson corresponds to the photon. The masses of the bosons are $M_{W^\pm} \approx 80 \text{ GeV}$ and $M_Z \approx 90 \text{ GeV}$ which explains the weak interaction's extremely short range of about 10^{-18} m .

The unified electromagnetic and weak interactions together with the strong interaction form what is called the standard model. It is a set of theories on the properties and interactions of the 12 fundamental particles which are arranged in doublets:

$$\begin{array}{l} \text{leptons:} \\ \text{quarks:} \end{array} \quad \begin{array}{ccc} \begin{pmatrix} e \\ \nu_e \end{pmatrix} & \begin{pmatrix} \mu \\ \nu_\mu \end{pmatrix} & \begin{pmatrix} \tau \\ \nu_\tau \end{pmatrix} \\ \begin{pmatrix} u \\ d \end{pmatrix} & \begin{pmatrix} c \\ s \end{pmatrix} & \begin{pmatrix} b \\ t \end{pmatrix} \end{array}$$

The particle “families” are arranged vertically, i.e. the first family, which constitutes all matter around us, contains the e , ν_e , u and d . Besides the 12 fermions, there are also 13 gauge bosons: 8 gluons are mediating the strong interaction, the W^+ , W^- and Z^0 mediate the weak interaction, and the photon is responsible for the electromagnetic interaction. Finally, the Higgs boson is responsible for the masses of the particles.

The standard model became widely accepted after the initial experimental confirmation of several predicted particles and processes. The discovery of neutral currents which is mediated by the Z^0 boson confirmed, and the detection of the heavy bosons (W^\pm , Z^0) further established the theory of the electroweak interaction. In the strong sector the situation was not so clear: identifying the quarks with the partons, the constituents of the hadrons, was a bumpy road. However, with the discovery of the heavier quarks (c , t , b) and the development of the asymptotic confinement model, this theory also became widely accepted. The only particle missing so far, the Higgs boson, is believed to be observed by the ATLAS and CMS experiments at the Large Hadron Collider (LHC) in CERN.

The energies involved in nuclear β decay are so low in comparison with the masses of the charged W^\pm bosons that a previous, more phenomenological approach is satisfactory, which will be outlined in the following section.

2.1.2 The Hamiltonian of Lee and Yang

The first theoretical description of nuclear β decay was given by Fermi in 1934 [3, 4]. Using Pauli's neutrino hypothesis, he proposed a direct interaction of four spin- $\frac{1}{2}$ quantum fields (currents), corresponding to the four particles involved. The hamiltonian in this case takes the following form:

$$H_\beta = \frac{G_F}{\sqrt{2}} (\bar{p}\gamma_\mu n)(\bar{e}\gamma^\mu \nu_e) + \text{h.c.} \quad (2.1)$$

where G_F is the Fermi coupling constant, γ_μ are the Dirac matrices, $(\bar{p}\gamma_\mu n)$ is the hadronic and $(\bar{e}\gamma^\mu \nu_e)$ the leptonic current, and h.c. stands for hermitian conjugate. The currents in this hamiltonian are vector type, which successfully explained transitions without spin change. However, soon experimental evidence began to point toward other types of currents as well. Gamow-Teller decays were indicating the presence of an axial vector or a tensor current, while pion decay was pointing toward a pseudoscalar or tensor current, etc. The currently accepted V-A structure was proposed by Marshak and Sudarshan [5]. At the same time, inspired by the ϑ - τ problem, Lee and Yang proposed [6] that parity might not be conserved in the weak interaction, which was soon experimentally verified in nuclear β decay [7, 8] and in pion/muon decay [9]. A more general Hamiltonian, allowing parity violation and all types of currents while still being

Lorentz invariant, has the following form [6]:

$$\begin{aligned}
\mathcal{H}_\beta = & (\bar{p}n) [\bar{e}(C_S + C'_S\gamma_5)\nu] \\
& + (\bar{p}\gamma_\mu n) [\bar{e}\gamma_\mu(C_V + C'_V\gamma_5)\nu] \\
& + \frac{1}{2}(\bar{p}\sigma_{\lambda\mu}n) [\bar{e}\sigma_{\lambda\mu}(C_T + C'_T\gamma_5)\nu] \\
& - (\bar{p}\gamma_\mu\gamma_5n) [\bar{e}\gamma_\mu\gamma_5(C_A + C'_A\gamma_5)\nu] \\
& + (\bar{p}\gamma_5n) [\bar{e}\gamma_5(C_P + C'_P\gamma_5)\nu] + \text{h.c.}
\end{aligned} \tag{2.2}$$

Here the tensor operator is given by $\sigma_{\lambda\mu} = -\frac{i}{2}(\gamma_\lambda\gamma_\mu - \gamma_\mu\gamma_\lambda)$ and $C_{i=S,V,A,T,P}$ are the scalar, vector, axial vector, tensor and pseudoscalar coupling constants. The convention used here, which is also the one that is used by Jackson et al. [10] and in general, the angular correlation formalism is the one where $1 + \gamma_5$ is the left handed chiral projection operator. This also implies that C_A has a negative value.

All coupling constants are complex where the imaginary part is non-zero in the case of a time reversal (\mathcal{T}) violation. The relative size of C_i and C'_i is defining the properties of the different possible weak interaction forms with respect to parity (\mathcal{P}) violation. It can be shown that for the case of nuclear β decay the pseudoscalar component vanishes ($C_P = C'_P = 0$). The Standard Model assumes maximal \mathcal{P} violation ($|C_i| = |C'_i|$) and no \mathcal{T} violation. Furthermore, it assumes a pure V-A structure, meaning that the S, P and T coupling constants are all 0. According to the conserved vector current (CVC) theory [11] the value of $C_V = C'_V$ is equal to 1. The value of the axial vector coupling constant is affected by the nuclear medium, and described by the partially conserved axial vector current theory, with its value $C_A = C'_A = -1.27$ [12] being obtained mainly from neutron decay.

The obvious way of testing the validity of the standard model is to experimentally determine the values of the different coupling constants. Jackson, Treiman and Wyld [10] have provided expressions for the β decays transition probability including all relevant correlation coefficients in function of these coupling constants. For the case of oriented nuclei the transition probability becomes

$$\begin{aligned}
w(\langle \mathbf{J} \rangle | E_e, \Omega_e) dE_e d\Omega_e = & \frac{F(\pm Z, E_e)}{(2\pi)^4} p_e E_e (E_0 - E_e)^2 dE_e d\Omega_e \xi \\
& \cdot \left\{ 1 + b \frac{m}{E_e} + A \frac{\langle \mathbf{J} \rangle}{J} \cdot \frac{\mathbf{p}_e}{E_e} \right\}
\end{aligned} \tag{2.3}$$

where J is the nuclear spin of the mother nucleus, $F(\pm Z, E_e)$ is the Fermi function, E_e , p_e and m are the electron total energy, momentum and mass, respectively with E_0 being the endpoint energy. The dependence on the coupling constants and the nuclear matrix elements is contained in the so-called correlation coefficients, here the β -asymmetry parameter A and the Fierz term b with ξ being given by:

$$\begin{aligned} \xi = & |M_F|^2 (|C_S|^2 + |C_V|^2 + |C'_S|^2 + |C'_V|^2) \\ & + |M_{GT}|^2 (|C_A|^2 + |C_T|^2 + |C'_A|^2 + |C'_T|^2) \end{aligned} \quad (2.4)$$

Here M_F and M_{GT} are the Fermi and Gamow-Teller nuclear matrix elements, respectively. A useful quantity is the Fermi/Gamow-Teller mixing ratio which is defined as:

$$\rho = \frac{M_{GT} C_A}{M_F C_V} \quad (2.5)$$

For a pure Fermi transition $\rho = 0$, while a pure Gamow-Teller transition corresponds to $\rho \rightarrow \infty$.

The two correlation coefficients, b and A will be discussed further in this section. For completeness, the beta-neutrino correlation coefficient $a_{\beta\nu}$ will be also introduced. A more detailed overview of these and other correlations is given in [13].

Fierz interference

The Fierz (interference) term, b is defined by [10]

$$b\xi = \pm 2\gamma\Re \left[|M_F|^2 (C_S C_V^* + C'_S C_V'^*) + |M_{GT}|^2 (C_T C_A^* + C'_T C_A'^*) \right] \quad (2.6)$$

where Z is the atomic number of the daughter nucleus, α the fine structure constant, $\gamma = \sqrt{1 - \alpha^2 Z^2}$ and the upper (lower) sign refers to β^- (β^+) decay. The Fierz term can also be expressed (redefined) in terms of ρ :

$$b' = \frac{m}{E_e} \frac{b\xi}{\xi} = \pm \frac{\gamma m}{E_e} \frac{1}{1 + \rho^2} \left[\Re \left(\frac{C_S + C'_S}{C_V} \right) + \rho^2 \Re \left(\frac{C_T + C'_T}{C_A} \right) \right]. \quad (2.7)$$

This term appears in the majority of correlation measurements, e.g. a measurement of the β -asymmetry parameter A in fact sensitive to $\hat{A} \equiv \frac{A}{1+b'}$. Furthermore it also influences the ft values of nuclei. For superallowed transitions the relation between the Fierz term and the corrected ft values ($\mathcal{F}t$) is given by [14]:

$$2\mathcal{F}t = \frac{K}{2G_F^2 V_{ud}^2 (1 + \Delta_R^V)} \frac{1}{1 + \langle b' \rangle} \quad (2.8)$$

A recent overview of the superallowed β transitions [15] restricted the scalar coupling constants to below the percent level. Limits on the tensor coupling constants however are limited by the β -asymmetry measurements with typically pure Gamow-Teller transitions, where the Fierz term has the following form:

$$b' = \pm \frac{\gamma m}{E_e} \Re \left(\frac{C_T + C'_T}{C_A} \right) \quad (2.9)$$

The β asymmetry parameter

The β asymmetry parameter A can be expressed in function of the coupling constants as [10]:

$$\begin{aligned} A\xi = & |M_{GT}|^2 \lambda_{J'J} \left[\pm 2\Re(C_T C'_T{}^* - C_A C'_A{}^*) + 2 \frac{\alpha Z m}{p_e} \Im(C_T C'_A{}^* + C'_T C_A{}^*) \right] \\ & + \delta_{J'J} M_F M_{GT} \sqrt{\frac{J}{J+1}} \left[2\Re(C_S C'_T{}^* + C'_S C_T{}^* - C_V C'_A{}^* - C'_V C_A{}^*) \right. \\ & \left. \pm 2 \frac{\alpha Z m}{p_e} \Im(C_S C'_A{}^* + C'_S C_A{}^* - C_V C'_T{}^* - C'_V C_T{}^*) \right] \end{aligned} \quad (2.10)$$

where

$$\lambda_{J'J} = \begin{cases} 1 & J \rightarrow J' = J - 1 \\ \frac{1}{J+1} & J \rightarrow J' = J \\ -\frac{J}{J+1} & J \rightarrow J' = J + 1 \end{cases} \quad (2.11)$$

As in the Standard Model all scalar and tensor coupling constants are 0 ($C_S, C_T = 0$) while $C_i = C'_i$ and $\Im(C_i) = 0$ for $i = V, A$, eq. 2.10 simplifies to:

$$\frac{A\xi}{\xi} \equiv A_{SM} = \frac{\mp \lambda_{J'J} \rho^2 - 2\delta_{J'J} \sqrt{\frac{J}{J+1}} \rho}{1 + \rho^2} \quad (2.12)$$

It follows that for a pure Fermi transition ($\rho = 0$) A becomes zero. This is expected since it represents the scalar product of the nuclear spin and the β particle's momentum, and a pure Fermi transition occurs only between spin 0 states. Knowing that the scalar and tensor couplings are small, eq. 2.10 can be

approximated as:

$$A \simeq A_{SM} + \frac{\alpha Z m}{p_e} \left[\frac{\lambda_{J'J} \rho^2 \pm \delta_{J'J} \sqrt{\frac{J}{J+1}} \rho}{1 + \rho^2} \Im \left(\frac{C_T + C'_T}{C_A} \right) \right. \\ \left. \pm \frac{\delta_{J'J} \sqrt{\frac{J}{J+1}} \rho}{1 + \rho^2} \Im \left(\frac{C_S + C'_S}{C_V} \right) \right] \quad (2.13)$$

For pure GT transitions this equation further reduces to

$$A_{GT} \simeq A_{SM} \left[1 - \frac{\alpha Z m}{p_e} \Im \left(\frac{C_T + C'_T}{C_A} \right) \right] \quad (2.14)$$

As was mentioned already, every experiment essentially measures $\tilde{A} = A/(1+b')$ so that the final formula becomes (using eq. 2.9)

$$\tilde{A}_{GT} \simeq A_{SM} \left[1 - \frac{\alpha Z m}{p_e} \Im \left(\frac{C_T + C'_T}{C_A} \right) \mp \frac{\gamma m}{E_e} \Re \left(\frac{C_T + C'_T}{C_A} \right) \right] \quad (2.15)$$

where the approximation $\frac{1}{1+x} = 1 - x$ was used and second order terms were neglected. If one wants to retain the correlation coefficients up to second order one would have:

$$\xi_{GT} = 2|M_{GT}|^2 C_A^2 \left[1 + \frac{|C_T|^2 + |C'_T|^2}{2C_A^2} \right] \quad (2.16)$$

and

$$\tilde{A}_{GT} = A_{SM} \left[1 \mp \Re \left(\frac{C_T C'_T}{C_A^2} \right) - \frac{|C_T|^2 + |C'_T|^2}{2C_A^2} \right. \\ \left. - \frac{\alpha Z m}{p_e} \Im \left(\frac{C_T + C'_T}{C_A} \right) \mp \frac{\gamma m}{E_e} \Re \left(\frac{C_T + C'_T}{C_A} \right) \right. \\ \left. \pm \frac{\alpha Z \gamma m^2}{p_e E_e} \Im \left(\frac{C_T + C'_T}{C_A} \right) \Re \left(\frac{C_T + C'_T}{C_A} \right) \right] \quad (2.17)$$

The time reversal violating component of the tensor current $\Im \left(\frac{C_T + C'_T}{C_A} \right)$ has been restricted below about 1% by an R correlation (triple correlation between the nuclear spin J and the electron's momentum \mathbf{p} and spin $\boldsymbol{\sigma}$, i.e. $R\mathbf{J}(\mathbf{p} \times \boldsymbol{\sigma})$) measurement with the isotope ${}^8\text{Li}$ [16]. A measurement of the β asymmetry parameter is then mostly sensitive to a time reversal conserving tensor current (the real component of the coupling constants), so that

$$\tilde{A}_{GT} \simeq A_{SM} \left[1 - \frac{(C_T \pm C'_T)^2}{2C_A^2} - \frac{\gamma m}{E_e} \frac{C_T + C'_T}{C_A} \right] \quad (2.18)$$

The β - ν correlation coefficient

The beta-neutrino correlation coefficient $a_{\beta\nu}$ is written as [10]:

$$\begin{aligned} a\xi = |M_F|^2 & \left[-|C_S|^2 + |C_V|^2 - |C'_S|^2 + |C'_V|^2 \mp 2\frac{\alpha Z m}{p_e} \Im(C_S C_V^* + C'_S C'_V^*) \right] \\ & + \frac{|M_{GT}|^2}{3} \left[|C_T|^2 - |C_A|^2 + |C'_T|^2 - |C'_A|^2 \pm 2\frac{\alpha Z m}{p_e} \Im(C_T C_A^* + C'_T C'_A^*) \right] \end{aligned} \quad (2.19)$$

The Standard Model value is

$$\frac{a\xi}{\xi} \equiv a_{SM} = \frac{1 - \rho^2/3}{1 + \rho^2} \quad (2.20)$$

leading to values of $-1/3$ for a pure GT transition and 1 for a pure Fermi transition. If one allows for scalar and tensor type currents in the weak interaction Hamiltonian, the expression for a becomes (up to first order):

$$a \simeq a_{SM} + \frac{\alpha Z m}{p_e} \frac{1}{1 + \rho^2} \left[\mp \Im \left(\frac{C_S + C'_S}{C_V} \right) \pm \frac{\rho^2}{3} \Im \left(\frac{C_T + C'_T}{C_A} \right) \right] \quad (2.21)$$

or, if also terms up to second order are retained:

$$\begin{aligned} a \simeq a_{SM} + \frac{\alpha Z m}{p_e} \frac{1}{1 + \rho^2} & \left[\mp \Im \left(\frac{C_S + C'_S}{C_V} \right) \pm \frac{\rho^2}{3} \Im \left(\frac{C_T + C'_T}{C_A} \right) \right] \\ & - \frac{1}{(1 + \rho^2)^2} \left[\left(1 + \frac{\rho^2}{3} \right) \frac{|C_S|^2 + |C'_S|^2}{C_V^2} + \frac{\rho^2}{3} (1 - \rho^2) \frac{|C_T|^2 + |C'_T|^2}{C_A^2} \right] \end{aligned} \quad (2.22)$$

Sensitivity factors

The two sensitivity factors, $\frac{\gamma m}{E_e}$ and $\frac{\alpha Z m}{p_e}$ that appear in the above equations for a , b and A are important if one wants to extract limits on the scalar or tensor coupling constants from a correlation measurement. The values of these factors, which depend on the e^\pm energy, must be taken as a weighted average over the part of the spectrum under investigation. It is useful then to introduce two new quantities,

$$W \equiv \frac{E_e}{m} = \frac{E_{kin}}{m} + 1 \quad \text{and} \quad q \equiv \frac{p_e}{m} = \sqrt{W^2 - 1}. \quad (2.23)$$

where the electron mass m is expressed in units of energy. Using this notation the sensitivity factors become $\gamma \langle W^{-1} \rangle$ and $\alpha Z \langle q^{-1} \rangle$. The energy dependence of $\frac{\gamma m}{E_e}$ is shown in figure 2.1 showing that it is decreasing with energy.

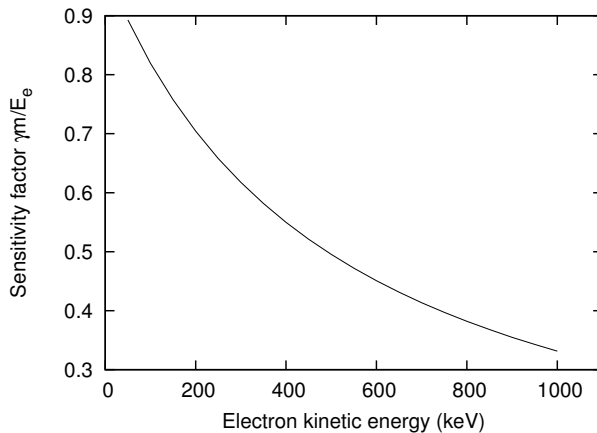


Figure 2.1: Dependence of the $\gamma m/E_e$ sensitivity factor on the kinetic energy of the β particle. γ was fixed at 0.98 to represent an element with Z around 20-30.

Recoil corrections

Taking the standard model form of the Hamiltonian of Lee and Yang (2.2), and after some rearranging one arrives to

$$\mathcal{H} = (\bar{u}\gamma_\mu(C_V - C_A\gamma_5)d)(\bar{e}\gamma^\mu(1 + \gamma_5)\nu) \quad (2.24)$$

which accurately describes the decay of the fundamental particles, quarks and leptons. Applying this to the simplest nuclear β decay, i.e. free neutron decay, the situation gets more complicated since the decaying quark is interacting with the other two spectator quarks. This influences the decay itself, replacing $\gamma_\mu C_V$ with the hadronic vector current $V_\mu = g_V(q^2)\gamma_\mu$ and $\gamma_\mu\gamma_5 C_A$ with the axial-vector current $A_\mu = g_A(q^2)\gamma_\mu\gamma_5$, where q is the momentum transfer. Furthermore, the decay is described with four additional *induced* coupling constants, all of which are functions of the momentum transfer: g_M (weak magnetism), g_S (scalar), g_T (tensor), g_P (pseudoscalar). Going still one step further, the β decay of a nucleus requires ten form factors ($a, b, c, d, e, f, g, h, j_2, j_3$) as described by Holstein¹ [17, 18]. These form factors are connected to nuclear matrix elements and coupling constants by the impulse approximation. The form factors are also called recoil terms because of their $1/M$ dependence although they have no relation to the recoiling nucleus after decay. Holstein also gave formulas for the correlation coefficients as well as for the β spectrum

¹It is important to note that Holstein follows the notation of particle physics where $1 - \gamma_5$ is the left handed chiral projection operator.

shape in terms of these form factors. The differences with equations not taking into account the induced form factors can be significant when the precision of the experimental values approaches 1%. An overview of the experimentally available information on these form factors to date is in preparation [19].

2.2 Beyond the Standard Model

Despite the success of the standard model, there are many reasons to believe that it is not a complete theory. The neutrino oscillations prove that they must have non-zero mass, while the current theory assumes them massless. The observed matter-antimatter asymmetry also can not be explained by the CP violation incorporated in the standard model. Furthermore, the huge amount of free parameters (particle masses, CKM matrix elements, etc.) imply that there could be a more fundamental theory.

Numerous extensions of the standard model exist, many of which have already been greatly restricted by the newest results from the experiments performed at the LHC. The advantage of this direct approach is that if a new particle is found, then the theory predicting it is immediately confirmed. Another approach is by precision measurements of different experimental observables, such as branching ratios or correlation coefficients. The values obtained can be compared to those predicted by the standard model, with any significant difference then indicating the presence of new physics. The advantage of the latter method is that it is model-independent.

A more detailed discussion on the possible extensions of the standard model from the viewpoint of nuclear β decay can be found in the articles by Herczeg² [20] and Severijns et al. [13].

2.2.1 Constrains from LHC

The high energy available at the LHC enables the direct search for new particles of much higher masses than before. In order to compare the results obtained at the LHC with those from precision measurements in neutron and nuclear β decay we will follow the articles by Cirigliano [21] and Bhattacharya [22].

It can be shown that if the particles related to new physics can not be directly produced at the LHC then the underlying theory can be transformed into

²Note that Herczeg uses the convention where all the coupling constants C_i have the opposite sign to the ones used in this work.

an effective field theory which is then comparable to the low energy results. Cirigliano et al. use the following hamiltonian:

$$\begin{aligned}
\mathcal{L} = & -\frac{G_F V_{ud}}{\sqrt{2}} [(1 + \epsilon_L) \bar{e} \gamma_\mu (1 - \gamma_5) \nu \cdot \bar{u} \gamma^\mu (1 - \gamma_5) d \\
& + \tilde{\epsilon}_L \bar{e} \gamma_\mu (1 + \gamma_5) \nu \cdot \bar{u} \gamma^\mu (1 - \gamma_5) d \\
& + \epsilon_R \bar{e} \gamma_\mu (1 - \gamma_5) \nu \cdot \bar{u} \gamma^\mu (1 + \gamma_5) d + \tilde{\epsilon}_R \bar{e} \gamma_\mu (1 + \gamma_5) \nu \cdot \bar{u} \gamma^\mu (1 + \gamma_5) d \\
& + \epsilon_S \bar{e} \gamma_\mu (1 - \gamma_5) \nu \cdot \bar{u} d + \tilde{\epsilon}_S \bar{e} \gamma_\mu (1 + \gamma_5) \nu \cdot \bar{u} d \\
& - \epsilon_P \bar{e} \gamma_\mu (1 - \gamma_5) \nu \cdot \bar{u} \gamma_5 d - \tilde{\epsilon}_P \bar{e} \gamma_\mu (1 + \gamma_5) \nu \cdot \bar{u} \gamma_5 d \\
& + \epsilon_T \bar{e} \sigma_{\mu\nu} (1 - \gamma_5) \nu \cdot \bar{u} \sigma^{\mu\nu} (1 - \gamma_5) d + \tilde{\epsilon}_T \bar{e} \sigma_{\mu\nu} (1 + \gamma_5) \nu \cdot \bar{u} \sigma^{\mu\nu} (1 + \gamma_5) d]
\end{aligned} \tag{2.25}$$

with the $1 - \gamma_5$ being the left-handed chiral projection operator. The coupling constants ϵ_i involve left-handed neutrinos, while $\tilde{\epsilon}_i$ are associated to right-handed neutrinos. Going from the quark to the nucleon level, the coupling constants from equation 2.2 can be expressed via the ϵ parameters in the following way:

$$\begin{aligned}
C_i &= G_F V_{ud} \bar{C}_i / \sqrt{2} & \bar{C}_S &= g_S (\epsilon_S + \tilde{\epsilon}_S) \\
\bar{C}_V &= g_V (1 + \epsilon_L + \epsilon_R + \tilde{\epsilon}_L + \tilde{\epsilon}_R) & \bar{C}'_S &= g_S (\epsilon_S - \tilde{\epsilon}_S) \\
\bar{C}'_V &= g_V (1 + \epsilon_L - \epsilon_R - \tilde{\epsilon}_L - \tilde{\epsilon}_R) & \bar{C}_P &= g_P (\epsilon_P - \tilde{\epsilon}_P) \\
\bar{C}_A &= -g_A (1 + \epsilon_L - \epsilon_R - \tilde{\epsilon}_L + \tilde{\epsilon}_R) & \bar{C}'_P &= g_P (\epsilon_P + \tilde{\epsilon}_P) \\
\bar{C}'_A &= -g_A (1 + \epsilon_L - \epsilon_R + \tilde{\epsilon}_L - \tilde{\epsilon}_R) & \bar{C}_T &= 4g_T (\epsilon_T + \tilde{\epsilon}_T) \\
& & \bar{C}'_T &= 4g_T (\epsilon_T - \tilde{\epsilon}_T)
\end{aligned}$$

Here $g_V = 1$ with additional second-order isospin breaking corrections. The determination of $g_{i=A,S,T,P}$ from first principles, however, requires lattice QCD calculations. Since the $\tilde{\epsilon}_i$ appear in nuclear correlation coefficients quadratically or with the rather small factor m_ν/E_ν , the low energy measurements will mostly limit the ϵ_i couplings.

CKM unitarity tests, which from this perspective essentially measure C_V , provide the strongest limits on $(\epsilon_L + \epsilon_R)$ [23]. Only ϵ_R is accessible separately, in the β asymmetry measurement of the neutron (see section 2.2.4):

$$A^n \sim \frac{C_A}{C_V} \simeq (1 - 2\epsilon_R) \frac{g_A}{g_V} \tag{2.26}$$

However, the extraction of ϵ_R involves lattice QCD calculations of g_A/g_V which have not reached the sub-percent precision yet. The already mentioned overview

of the superallowed β transitions [15] provide limits on ϵ_S [21] via the Fierz term:

$$-0.001 < g_S \epsilon_S < 0.0032 \text{ at } 90\% \text{ CL} \quad (2.27)$$

which are similar to the ones obtained from the LHC. The tensor couplings are restricted by the radiative pion decay $\pi \rightarrow e\nu\gamma$ [21]

$$-2.0 \times 10^{-4} < g_T \epsilon_T < 2.6 \times 10^{-4} \text{ at } 90\% \text{ CL} \quad (2.28)$$

however, they are also similar to LHC limits. Future high precision correlation measurements in neutron and nuclear decay at the 10^{-3} level will limit the scalar and tensor coupling constants on the 5×10^{-4} level. Further improvements in this sector could mean that the low energy searches will outperform the LHC results. However, if one allows right-handed couplings via $\tilde{\epsilon}_S$ and $\tilde{\epsilon}_T$, the LHC bounds are better by an order of magnitude.

2.2.2 Left-right symmetric models

Some of the popular extensions of the standard model are left-right symmetric models, which provide a natural framework for the parity violation observed in β decay. These introduce new, purely right-handed leptons, but also new bosons. The W_1 and Z_1 mass eigenstates are predominantly left-handed, while W_2 and Z_2 are mostly right-handed. The weak eigenstates W_L and W_R are mixed, similarly to the concept of quark mixing:

$$\begin{aligned} W_L &= W_1 \cos \zeta + W_2 \sin \zeta \\ W_R &= e^{i\omega} (-W_1 \sin \zeta + W_2 \cos \zeta) \end{aligned} \quad (2.29)$$

where ζ is the mixing angle and ω is a CP-violating phase. We also introduce $\delta = m_1/m_2$ where m_1 and m_2 as the masses of W_1 and W_2 . Further, by using the simple limit of the manifest left-right symmetry one arrives to the expressions for the coupling constants of equation 2.2 [13]:

$$\begin{aligned} C_V &= g_V a_{LL} (1 - 2\zeta + \delta) \\ C'_V &= g_V a_{LL} (1 - \delta) \\ C_A &= g_A a_{LL} (1 + 2\zeta + \delta) \\ C'_A &= g_A a_{LL} (1 - \delta) \end{aligned} \quad (2.30)$$

where a_{LL} is defined by Herczeg [20]. The sensitivity of the β asymmetry parameter A to these models is given in the review by Severijns et al. [13].

2.2.3 Search for tensor currents

Over the years numerous experiments set the goal of verifying the standard model by correlation measurements in nuclear β decay. The most recent survey by Severijns, Beck and Naviliat-Cuncic [13] contains several fits of the coupling constants (eq. 2.2) to the experimental data available. The 2σ confidence levels of the coupling constants requiring only \mathcal{T} conservation (all parameters are considered real) are:

$$\begin{aligned}
 -1.40 &< C_A/C_V < -1.17 \\
 0.87 &< C'_V/C_V < 1.17 \\
 0.86 &< C'_A/C_A < 1.16 \\
 -0.065 &< C_S/C_V < 0.070 \\
 -0.067 &< C'_S/C_V < 0.066 \\
 -0.076 &< C_T/C_A < 0.090 \\
 -0.078 &< C'_T/C_A < 0.089
 \end{aligned} \tag{2.31}$$

Note that the standard model assumes $C'_i/C_i = 1$, $C_V = 1$ and $C_S = C_T = 0$. Further, the value of C_A/C_V is determined experimentally, since the axial vector current is only partially conserved. The limits presented are in agreement with the standard model, however, the relatively large limits on the tensor and scalar coupling constants creates a lot of interest in this field. Since the publication of these results new experiments have produced more accurate results which exclude the scalar and tensor currents on the several percent level. Some of them will be outlined in section 2.2.4.

2.2.4 Experimental status

Besides the β asymmetry parameter A several other correlation coefficients are sensitive to the tensor coupling constants C_T and C'_T . The ones measured with sufficient precision are the β - ν correlation $a_{\beta\nu}$ and the R triple correlation [13].

In table 2.2 the most accurate measurements of A are summarized. A more extensive table can be found in Wauters et. al [24].

Nucleus	Transition	A_{exp}	A_{SM}	Reference
^{60}Co	$5^+ \rightarrow 4^+$	-0.972(34)	-0.987(9)	[25]
		-1.01(2)		[26]
		-1.014(20)		[24]
^{114}In	$1^+ \rightarrow 0^+$	-0.990(14)	-0.996(3)	[27]
^{19}Ne	$1^+ \rightarrow 0^+$	-0.0391(14)	-0.0417(10)	[28]

Table 2.2: Overview of the recent highest precision measurements of the β -asymmetry parameter in nuclear decays. The uncertainties on the A_{SM} of ^{60}Co and ^{114}In are mainly due to the uncertainty of the recoil corrections while for ^{19}Ne it is due to the uncertainty of the Fermi/Gamow-Teller mixing ratio.

The β asymmetry parameter of the neutron

Extended overviews of the lifetime and correlation measurements in neutron decay was given by Abele [29], Nico [30], and Konrad [31]. Here we will focus only on some correlation measurements. The β decay of a free neutron proceeds via a mixed Fermi/Gamow-Teller transition so that a measurement of A essentially determines the ratio C_A/C_V (using $M_{GT} = \sqrt{3}$ and $M_F = 1$ for the neutron):

$$\rho = \frac{M_{GT}C_A}{M_FC_V} = \sqrt{3}\frac{C_A}{C_V} \equiv \sqrt{3}\lambda \quad (2.32)$$

This is used together with the neutron lifetime τ_n (current world average is 880.0(11) s [32]) to determine the $|V_{ud}|$ element of the Cabibbo-Kobayashi-Maskawa (CKM) quark mixing matrix [33, 14]. Usually $|V_{ud}|$ is calculated from the converted $\mathcal{F}t$ values of the superallowed $0^+ \rightarrow 0^+$ nuclear β transitions [15], which yields for now a much more accurate value. Turning the situation around, one can calculate λ_{SM} for the neutron and thus the standard model value of $A_{SM} = -0.1194(9)$ where the uncertainty is dominated by the neutron lifetime. It was noted by Severijns and Naviliat-Cuncic [34] that the results of older measurements of λ (essentially A) are systematically lower and were subject to rather large corrections on the final value. The authors recommend taking the average of only the latest four experiments which are summarized in table 2.3.

The expression for the β asymmetry parameter of the neutron, neglecting the scalar coupling constants C_S and C'_S , can be derived from eq 2.10:

$$\tilde{A}^n = \tilde{A}_{SM}^n \left[1 - \gamma \langle W^{-1} \rangle \frac{\rho^2}{1 + \rho^2} \Re \frac{C_T + C'_T}{C_A} \right] \quad (2.33)$$

As can be seen from this equation, the average value of \tilde{A}^n can not be used to extract limits on the tensor currents since the sensitivity factor $\gamma \langle W^{-1} \rangle$ (see

section 2.1.2) is different for each experiment. The separate limits on $(C_T + C'_T)$ that are obtained are also shown in table 2.3.

Measurement	A_{exp}^n	$\gamma\langle W^{-1} \rangle$	$(C_T + C'_T)/C_A$
Mostovoi et al. [35]	-0.1168(17)	0.526	-0.050(37)
Abele et al. [36]	-0.1189(7)	0.522	-0.010(23)
Mund et al. [37]	-0.11972($^{+53}_{-65}$)	0.529	0.006(21)
Mendenhall et al. [38]	-0.1195(11)	0.545	0.002(27)

Table 2.3: Overview of the most recent β -asymmetry measurements in free neutron decay. The sensitivity factor was estimated based on the region used for analysis so limits on the tensor currents could be obtained. The tensor coupling constants are assumed real.

The β - ν correlation coefficient in Gamow-Teller decays

The accurate determination of $a_{\beta\nu}$ also provides limits on the tensor coupling constants. In the past this correlation coefficient has been measured mainly in superallowed decays which are only sensitive to scalar currents. For pure Gamow-Teller transitions, the most accurate measurement was performed by Johnson et al. [39] 50 years ago on ${}^6\text{He}$ resulting in $a_{\beta\nu} = -0.3343(30)$.

The LPCTrap setup at GANIL is aiming to improve this result, using ${}^6\text{He}$ ions which are trapped in a Paul trap. After β decay both the electron and the recoiling nucleus are detected, which allows the reconstruction of the full decay kinematics. The result, $a_{\beta\nu} = -0.3335(104)$ [40] is only 3% precise but much more statistics is in the meantime already available and is now being analysed. A measurement of the mirror transition of ${}^{35}\text{Ar}$ has already been performed as well and a measurement of ${}^{19}\text{Ne}$ is in preparation [41].

Another precision measurement of $a_{\beta\nu}$ in the decay of ${}^8\text{Li}$ was carried out using the the Beta-decay Paul Trap at Argonne National Laboratory [42]. The experiment does not measure the recoiling nucleus because in this particular case the daughter nucleus ${}^8\text{Be}$ immediately decays into two α particles. By observing these together with the β particle one can reconstruct the decay kinematics. Their limit on the tensor coupling constant is $|C_T/C_A| \leq 0.18$ (95% C.L.), assuming maximal parity violation ($C'_T = C_T$).

Other relevant measurements

Several older measurements were summarized by Severijns et al. [13] and by Wauters [43] therefore here we will focus on the newer ones.

The R (triple correlation between the nuclear spin and the electron's momentum and spin; see section 2.1.2) and N (correlation between the nuclear and electron spin, i.e. $N\mathbf{J}\boldsymbol{\sigma}$) correlation coefficients in neutron decay were determined with high precision in a recent experiment [44, 45] performed at the FUNSPIN neutron beamline at the Paul Scherrer Institute in Switzerland. It requires the simultaneous observation of the electron's momentum and spin, as well as of the initial neutron's spin. The R correlation coefficient is zero to first approximation within the standard model while $N_{SM} = 0.068$ [44]. The limits on new physics obtained from the N correlation result are less stringent because of the uncertainties on its standard model value. However, the R correlation measurement limits the \mathcal{T} violating scalar and tensor currents to a level of several percents:

$$-0.218\Im\frac{C_S + C'_S}{C_V} + 0.335\Im\frac{C_T + C'_T}{C_A} = 0.004(13) \quad (2.34)$$

The D correlation (requiring the observation of the electron and proton momentum as well as of the initial spin) was recently measured in neutron decay by Chupp et al. [46]. It is mainly sensitive to the imaginary part of the V - and A - coupling constants, as can be seen from equation 2.35.

$$\begin{aligned} (-0.94 \pm 2.11) \cdot 10^{-4} = & \frac{1}{1 + 3\lambda^2} \left[-2 \frac{\Im(C_V C_A^*)}{|C_V|^2} + \frac{\Im(C_S C_T^* + C'_S C_T'^*)}{|C_V|^2} \right. \\ & \left. + \frac{\alpha m}{p_e} \Re \left(\lambda^* \frac{C_T^* + C_T'^*}{C_A^*} - \lambda^* \frac{C_S + C'_S}{C_V} \right) \right] \end{aligned} \quad (2.35)$$

The limits on the time reversal violating part of the scalar and tensor coupling constants are at the level of several percent.

The neutron decays via a mixed Fermi/Gamow-Teller transition therefore its beta-neutrino correlation coefficient $a_{\beta\nu}$ is sensitive to possible tensor currents. The aSPECT setup uses a retardation spectrometer to measure the proton spectrum from the neutron decay, and set the goal of extracting the $a_{\beta\nu}$ parameter with a sub-percent accuracy [47, 48].

Chapter 3

Low Temperature Nuclear Orientation

The magnetic moment of a nucleus interacts with a magnetic field B according to the Hamiltonian $\mathcal{H} = -\mu B$. The magnetic field provides a quantization axis for the nuclear spin and due to the interaction mentioned these sublevels split with energies $E_m = -m\mu B/J$, where $m = -J, \dots, J$. The spacing between the Zeeman splitted sublevels is constant. The population of these spin substates is uniform if the thermal energy of the nuclei is higher than the splitting of the levels $\Delta E = \mu B/J$. The distribution of the spins at temperature T is given by the Boltzmann distribution as:

$$p_m = \frac{\exp \frac{-m\Delta E}{k_B T}}{\sum_{m=-J}^J \exp \frac{-m\Delta E}{k_B T}} \quad (3.1)$$

In order to achieve appreciable asymmetry in the spin state distribution the fraction $\frac{\mu B}{k_B J T}$ needs to be close to unity, which requires magnetic fields of the order of several Tesla and temperatures in the milliKelvin region. The high magnetic fields can be reached by two methods:

- *Low Temperature Nuclear Orientation* (LTNO) exploits the fact that many nuclei when implanted in a ferromagnetic host foil experience strong hyperfine fields of the order of tens of Tesla. A table of measured hyperfine fields for various host-impurity combinations can be found in [49, 50].
- *Brute Force Nuclear Orientation* uses a strong superconducting magnet to deliver the required magnetic fields. More information about this technique can be found in [51].

In this work the low temperatures were obtained with a ^3He - ^4He dilution refrigerator. The typical base temperature of such devices is around 5 mK, which in combination with the hyperfine magnetic fields enables reaching high degrees of orientation.

3.1 Formalism

The formalism of LTNO is covered in great detail in [52]. Here we focus on the part relevant to this work.

Radiation originating from oriented nuclei is, in general, anisotropic. The experimentally observed anisotropy can be described by the following formula, assuming an axially symmetric system.

$$W(\theta) = 1 + f \sum_{\lambda=1}^{2J} A_{\lambda} B_{\lambda} U_{\lambda} Q_{\lambda} P_{\lambda}(\cos \theta) \quad (3.2)$$

Here f represents the fraction of the nuclei that feel the hyperfine interaction μB , the A_{λ} coefficients describe the angular distribution of the emitted radiation and so depend on the type of transition, and the B_{λ} account for the degree of nuclear orientation. Further, the deorientation coefficients U_{λ} take into account the effect of any unobserved radiation, while Q_{λ} are the solid angle coefficients and P_{λ} are the Legendre polynomials. All these coefficients are covered in more detail in the following sections. For allowed β decay only the first term of the sum is kept, while for γ decay the sum goes over the even values of λ .

In the formalism of Jackson, Treymen and Wyld [10] the expression for the angular distribution of electrons for an allowed beta transition is

$$W(\theta) = 1 + f \tilde{A} P \frac{v}{c} Q_1 \cos \theta \quad (3.3)$$

where $\frac{v}{c}$ is the electron speed relative to the speed of light, \tilde{A} is the β -asymmetry parameter and P is the degree of polarization. This is equivalent to equation 3.2 with the following relations between the parameters:

$$A_1 = -\frac{v}{c} \sqrt{\frac{J+1}{3J}} \tilde{A} \quad B_1 = -\sqrt{\frac{3J}{J+1}} P \quad (3.4)$$

3.1.1 Angular distribution

β -decay

The angular distribution of the β particles for an allowed transition is determined by the A_1 parameter, which is linked to the β asymmetry parameter \tilde{A} by equation 3.4. For pure Gamow-Teller transitions as considered in this work one has

$$A_1 = \begin{cases} -\frac{v}{c} \sqrt{\frac{J+1}{3J}} \tilde{A} & \text{for } J \rightarrow J-1 \\ \frac{v}{c} \sqrt{\frac{J}{3(J+1)}} \tilde{A} & \text{for } J \rightarrow J+1 \end{cases} \quad (3.5)$$

γ -decay

The asymmetry of γ rays is described by the even A_λ parameters where typically only the A_2 and A_4 parameters need to be considered as $A_4 < A_2$ and $A_6 \ll A_4$. The odd terms vanish since the electromagnetic interaction conserves parity. The A_λ are completely determined by the initial and final spin J_i and J_f and by the multipolarity of the transition L . For a mixed transition the multipole mixing ratio δ is required to calculate an effective A_λ :

$$A_\lambda = \frac{F_\lambda(L, L, J_f, J_i) + 2\delta F_\lambda(L, L', J_f, J_i) + \delta^2 F_\lambda(L', L', J_f, J_i)}{1 + \delta^2} \quad (3.6)$$

The F_λ functions are tabulated in [53], and are 0 for $\Delta J = 0$ or $J_i < 1$. Since the angular distribution of γ rays depends only on the spin sequence and the multipolarity, they are suitable for nuclear thermometry (see subsection 3.2.4) as well as for fraction determination (see subsection 3.1.5).

3.1.2 Orientation mechanism

The orientation parameters B_λ describe the spin state distribution of the nuclei. As such, they depend on the temperature of the lattice (here we assume thermal equilibrium between the lattice and the implanted nuclei) and on the size of the splitting of the spin states ($\sim \mu B$). One can simply take the average of the z projection of the nuclear spin J using eq. 3.1 in the following manner

$$\langle J_z \rangle / J = \sum_m (m/J) p_m = P(J) \quad (3.7)$$

which describes the degree of polarization of the nuclei. Of the higher order parameters we can consider the second order $\langle J_z^2 \rangle / J^2$ which is equal to $(J +$

1)/(3J) for an unoriented sample and gives the nuclear alignment. It can be easily proven that the odd-order parameters change sign when the spins change direction, while the even ones remain constant.

These orientation parameters are intuitively easily understood, nevertheless the NO formalism uses the B_λ coefficients so taking into account the fact that the actual decay under investigation occurs between the spin substates. This effect can be accounted for by using the Wigner 3-j symbols which restrict λ to be smaller than $2J$.

$$B_\lambda = \sqrt{(2\lambda + 1)(2J + 1)} \sum_{m=-J}^J (-1)^{J+m} \begin{pmatrix} J & J & \lambda \\ -m & m & 0 \end{pmatrix} p_m \quad (3.8)$$

Since the orientation parameter is the only temperature dependent factor in eq 3.2, it is possible to perform a two-parameter fit of the anisotropy curve $W(\theta)$ versus temperature to obtain the value of μB and a second, temperature independent parameter (typically the fraction f).

3.1.3 Nuclear relaxation

The orientation parameters introduced in section 3.1.2 are valid under the assumption of thermal equilibrium between the host foil and the nuclei one is observing. This requires a strong enough coupling between the nuclear spins and the host lattice enabling the nuclei to relax and reach thermal equilibrium after a certain time. In non-metallic systems the nuclear relaxation time at milliKelvin temperatures can be of the order of years, but in ferromagnetic metals it is typically of the order of seconds and minutes [54]. In classical LTNO experiments this is rarely an issue, but in the case of on line LTNO (OLNO), where the nuclei are implanted into a cooled host foil and measured at the same time, relaxation often causes attenuation of the observed orientation compared to the full thermal equilibrium effect. However, the possibility to investigate with OLNO nuclei with much shorter halfives than before (typically as small as 1 s vs. several hours in classical LTNO) outweighs by far the complications arising from relaxation effects.

For a precision experiment detailed knowledge of the relaxation mechanism is required. A detailed discussion can be found in [54], here only the relevant sections are emphasized, following mostly [55]. Relaxation theories always work with the “standard case”, which means dilute impurities subject to a purely magnetic static hyperfine interaction. Under the assumption that the heat capacity of the thermal reservoir (in our case of the host foil) is much larger than that of the nuclear spin system two idealized cases appear:

1. *Single impurity limit.* The spin of the nucleus in question is coupled only to the host lattice. This is valid for concentrations of a few ppm or less.
2. *Spin temperature limit.* The spins of the implanted nuclei interact and they establish a Boltzmann distribution corresponding to a spin temperature. This becomes valid at concentrations around the percent level.

In the case of OLNO the amount of implanted ions is so low (typically $< 10^{12}$ to at most 10^{13} at/cm²) that the single impurity limit is considered to be valid at all times. In this case the nuclei relax independently, and the spin state populations p_m can be described by the following expression

$$\frac{dp_m}{dt} = \sum_n (W_{n,m}p_n - W_{m,n}p_m) \quad (3.9)$$

where $W_{m,n}$ stands for the transition probability $|m\rangle \rightarrow |n\rangle$. These probabilities can be derived by assuming a weak coupling between the nuclear spins and the lattice so it can be treated in perturbation theory. The nuclei relax by exchanging energy with the conduction electrons in the host lattice. These electrons are represented by their wave vector \mathbf{k} and spin s . A nuclear transition $|m\rangle \rightarrow |n\rangle$ will be associated with an electron transition $|\mathbf{k}s\rangle \rightarrow |\mathbf{k}'s'\rangle$. The transition probabilities from the initial state $|m\mathbf{k}s\rangle$ to the final $|n\mathbf{k}'s'\rangle$ can be found using Fermi's golden rule:

$$W_{m\mathbf{k}s, n\mathbf{k}'s'} = \frac{2\pi}{\hbar} |\langle m\mathbf{k}s | \hat{H}_{SL} | n\mathbf{k}'s' \rangle|^2 \delta(E_m + E_{\mathbf{k}s} - E_n - E_{\mathbf{k}'s'}) \quad (3.10)$$

where \hat{H}_{SL} is the spin-lattice interaction Hamiltonian and the δ function ensures energy conservation. This Hamiltonian can be written in terms of the nuclear spin ladder operator \hat{I} and the effective spin operator \hat{S} :

$$\hat{H}_{SL} = AI_z S_z + \frac{1}{2}A(S_+ I_+ + S_- I_-) \quad (3.11)$$

The weak coupling between the nuclear spins (S) and the lattice (L) means that the above equation can be broken up into a nuclear spin part and an electronic part, finally arriving at the only non-zero transition probabilities

$$\begin{aligned} W_{m+1,m} &= \frac{T_i}{2C_K} \frac{J(J+1) - m(m+1)}{1 - \exp(-T_i/T_L)} \\ W_{m,m+1} &= \frac{T_i}{2C_K} \frac{J(J+1) - m(m+1)}{\exp(T_i/T_L) - 1} \end{aligned} \quad (3.12)$$

Here the interaction temperature is defined as $T_i = \Delta E_m/k_B$, T_L is the lattice temperature and C_K is the relaxation constant. In the high temperature

limit ($T_L \gg T_i$) both transition probabilities are equal and proportional to T_L , while in the low temperature limit ($T_L \ll T_i$) only the “downward” transitions $W_{m+1,m}$ are non-zero, driving all the spins toward the same state ($m = -J$).

The set of $2J + 1$ equations (eq. 3.9) can be written in matrix form as $\frac{d\mathbf{p}}{dt} = \mathbf{R}\mathbf{p}$. The general solution is of the form $\mathbf{p}(t) = \exp(\mathbf{R}t)\mathbf{p}(t = 0)$. To further investigate the solution, a diagonal matrix \mathbf{D} (with the matrix elements $D_{mn} = \delta_{mn} \exp(-E_m/2k_B T_L) = d_m$) is used to transform \mathbf{R} into a symmetric matrix $\mathbf{R}^S = \mathbf{D}^{-1}\mathbf{R}\mathbf{D}$. Using its eigenvalues k_l (and the matrix \mathbf{K} with $K_{lm} = \delta_{lm}k_l$) and its matrix of eigenvectors \mathbf{U}^S the solution becomes

$$\mathbf{p}(t) = \mathbf{D}\mathbf{U}^S\mathbf{e}^{\mathbf{K}t}(\mathbf{U}^S)^{-1}\mathbf{D}^{-1}\mathbf{p}(0) \quad (3.13)$$

which can be written in component form as:

$$p_m = \sum_{l=1}^{2J} r_{ml} e^{k_l t}, \quad \text{where} \quad r_{ml} = d_m U_{ml}^S \sum_n U_{nl}^S d_n^{-1} p_n(0) \quad (3.14)$$

The relaxation time constants $\tau_l = 1/k_l$ can be found for the two limiting cases. In the high temperature limit the relaxation curves contain only one exponential with a time constant $T_1 = \tau_1 = C_K/T_L$, while in the low temperature limit the time constants are defined by $\tau_l = \frac{2C_K}{l(2J+1-l)T_i}$ where the “slowest” exponential has a time constant of $\tau_1 = \frac{C_K}{JT_i}$. In both cases however all the spin state populations will reach equilibrium values when $t \rightarrow \infty$. For practical purposes we consider $t > 5T_1$ or $t > 5\tau_1$ to be in equilibrium.

Under the assumption that all the $p_n(0)$ are equal (which is the case for OLNO experiments) the relaxation is fully characterized by the C_K . A table of measured C_K values can be found in [54]. For a given isotope C_K can be estimated knowing that:

- For an isotope chain $\frac{\mu^2}{J^2} C_K$ is constant, where μ is the nuclear spin.
- An empirical estimate is given by $T_i^2 C_K = 1.4 \times 10^{-4} \text{ sK}^3$ for impurities in Fe host. Knowing that $\tau_l \propto C_K/T_i \propto 1/T_i^3$, nuclei with larger interaction temperature thus relax faster.

Equation 3.9 describes the time dependent spin state populations considering only relaxation. In an OLNO experiment new nuclei are, however, constantly being implanted (with isotropic spin orientation) and the nuclei are decaying with a lifetime τ , which can be described as:

$$\frac{dp_m}{dt} = \underbrace{\sum_n R_{mn} p_n}_{\text{relaxation}} - \underbrace{\frac{p_m}{\tau}}_{\text{decay}} + \underbrace{\frac{1}{\tau(2J+1)}}_{\text{implantation}} \quad (3.15)$$

Such a system will reach secular equilibrium, and for each m state the following equation can be written:

$$\frac{dp_m}{dt} = 0 = \sum_n (\tau R_{mn} - \delta_{mn}) p_n + \frac{1}{2J+1} \quad (3.16)$$

where

$$R_{mn} = \begin{cases} W_{n,m} & n \neq m, \\ -(W_{m,m+1} + W_{m,m-1}) & n = m \end{cases} \quad (3.17)$$

After solving the above system of linear equations we finally arrive to the spin state distribution p_m which are used in equation 3.8 to calculate the secular equilibrium values of the B_λ coefficients. Usually an attenuation factor ρ is introduced in the following manner $B_\lambda^{sec} = \rho(J, T_i/T_L, \tau T_i/C_K) B_\lambda$. Intuitively the factor $\tau T_i/C_K$ is the measure of the ratio of the nuclear lifetime to the relaxation time. When the lifetime is much longer than the relaxation time we have $\rho \rightarrow 1$ (i.e. full relaxation), and when it is much shorter we have $\rho \rightarrow 0$ (there is no time for the nuclei to orient). A table of calculated ρ values can be found in [55] and an extension to it in [56].

3.1.4 Deorientation

In general the radiation for which the angular distribution is observed does not originate directly from the oriented state J_0 , but is preceded by (possibly several) unobserved transitions. Since these transitions tend to equalize the spin state populations the orientation of the parent state J_i will be less than that of J_0 . This can be accounted for by introducing the deorientation coefficients U_λ which depend solely on the spin sequence and multipolarity of the transition, using the Wigner 6-j symbols, in the following manner:

$$U_\lambda(J_1, J_2, L) = (-1)^{J_1+J_2+L+\lambda} \begin{Bmatrix} J_1 & J_1 & \lambda \\ J_2 & J_2 & L \end{Bmatrix} \quad (3.18)$$

Mixed multipolarity transitions are accounted for by taking a weighted average of the deorientation coefficients with the multipole mixing ratios as weights. If several transitions are connecting J_i and J_0 (a cascade) the equivalent deorientation coefficient is just a product of the individual transitions' coefficients. If there are several branches then one needs to calculate a weighted average of the deorientation coefficients with the branching ratios as weights. A more detailed description can be found in [52] and the U_λ coefficients are tabulated in [53].

3.1.5 Fraction

The nuclei in a ferromagnetic host foil experience the magnetic hyperfine field which is responsible for the Zeeman splitting of the spin states. However, the magnitude of the hyperfine field is dependent on the position of the impurity atom in the lattice. In general, one would need to expand the orientation parameters (which depend on the magnetic field) in the following manner:

$$B_\lambda = \sum_i f_i B_\lambda(B_{HF,i}) \quad (3.19)$$

However, the field strengths at other than substitutional positions are almost negligible. Furthermore if one prepares a sample by ion implantation at low temperature and low dose most of the impurities will be at substitutional sites. Thus we can approximate the previous expression using the so-called two site model: a fraction f of the nuclei feel the full orienting hyperfine field, while the rest $(1 - f)$ feel no field at all. Since this is an approximation, it is only applicable when the fraction is high. A low fraction indicates bad implantation conditions.

The fraction depends on many factors, e.g. the sample foil surface preparation and the sample preparation method (implanted or diffused source) and it should be determined for every sample separately. The easiest way is to observe the anisotropy of a γ ray following or preceding the β transition one is measuring. This, however, requires accurate knowledge of the γ -ray multipole mixing ratios (best is therefore to use pure transitions) while there are also some conditions on the spin sequence (see subsection 3.1.1).

Lacking a suitable γ transition another isotope of the same element can be measured. In the case of an OLNO experiment two isotopes can be implanted, one for the β asymmetry measurement and the other for fraction determination. In this case a γ transition, but also a high endpoint energy β transition can be used. The high endpoint energy means small sensitivity to non-standard model physics (see eq. 2.15) so that a fit of the β asymmetry to the fraction (see subsection 3.1.2) is possible to high precision.

3.1.6 Solid angle effects

The Q_λ coefficients account for the reduction of anisotropy due to the geometry (integration over a finite solid angle) of the experiment. The finite size of the source and the detector both reduce the observed anisotropy. The scattering of β particles changes both the initial emission angle θ as well as the emission energy. The magnetic field influences the electron trajectories, having also an

effect on the initial emission angle. The β and γ particles are affected differently so we will deal with them separately.

γ detectors

For the measurement of γ anisotropies one integrates the full energy peak in the spectrum, which means that the γ ray traveled in a straight line to the detector, and so the initial emission angle was not affected. Furthermore γ detectors are axially symmetric and usually well characterized. In a typical LTNO experiment with a source diameter of 5 mm and a source-detector distance of 10 cm the solid angle correction for the source size is below 0.1%, while for the detector it is of order 1%, so that only the latter correction is taken into account. For such conditions the Q_λ factors are given by [52]:

$$Q_\lambda^{detector} = \frac{\int_0^\xi \varepsilon(x) P_\lambda(\cos x) \sin x \, dx}{\int_0^\xi \varepsilon(x) \sin x \, dx} \quad (3.20)$$

where $\xi = \arctan \rho/d$ with d the source-detector distance and ρ the detector radius; ε is the detector efficiency.

Particle detectors

The β particles scatter in the source, on the detector and on the surrounding material. Furthermore, their trajectories are affected by the magnetic field, meaning that the formalism for γ detection can not be applied. Instead a Monte Carlo simulation is used to account for these effects. The entire experiment is simulated using the Geant4 software framework in order to arrive to the factor $\frac{z}{c} Q_1 \cos \theta$ (eq. 3.3). The procedure is described in more detail in chapter 5.

3.2 Experimental setup

Both isotopes of Cu investigated here were produced at the ISOLDE facility at CERN. There, 1.4 GeV protons from the Proton Synchrotron Booster bombard a ZrO_2 felt target inducing spallation and fragmentation reactions. The reaction products diffuse out of the target into the ion source. In this work a laser ion source was used with a two step excitation of ground state Cu into an autoionizing state. A 60 kV electrostatic potential extracts the ions which are guided through the General Purpose Separator of about 1/600 mass resolution.

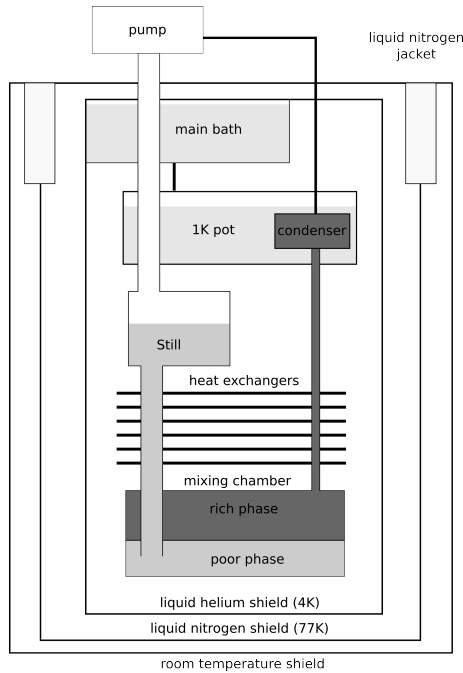


Figure 3.1: Scheme of a ^3He - ^4He dilution refrigerator.

The particular isotope selected is then further guided through several tens of meters of beamline into the NICOLE setup which is used for the measurement.

NICOLE (Nuclear Implantation into Cold On Line Equipment) is a ^3He - ^4He dilution refrigerator coupled to the ISOLDE beamline. A split-coil superconducting magnet is installed around the sample holder capable of providing magnetic fields up to 2T. Up to three particle detectors can be placed inside the liquid helium radiation shield, facing the sample directly.

3.2.1 Dilution refrigerators

The basic idea behind the ^3He - ^4He dilution refrigerators is the fact that a mixture of liquid ^3He and ^4He spontaneously separates into a ^3He rich and ^3He poor (6 – 7%) phase. The energy required to transport ^3He from the rich to the poor phase is taken from the environment, providing cooling power. A simplified scheme is displayed in figure 3.1 showing the main components of such refrigerators.

The main bath contains liquid helium (4 K) and is connected to the 1 K pot, which is pumped to reach 1.2 K, hence the name. The mixture is condensed by the condenser in the 1 K pot, and through a series of heat exchangers it reaches the mixing chamber. Here the temperature is low enough so the mixture separates into two phases. The part of the mixing chamber filled with the dilute phase is connected to the still. The vapor containing mainly ^3He is pumped away from the still, thus lowering the ^3He concentration in the dilute phase in the mixing chamber, which forces transport of ^3He from the rich phase. Radiation shields (at 4 K, 77 K and room temperature) help reduce the thermal load.

Such a refrigerator is capable of keeping the sample at mK temperatures for weeks. There is no theoretical lower limit to the base temperature, however for practical design reasons it is usually above 2 mK. At NICOLE the typical lowest temperature is around 5 mK. When performing an OLNO experiment the base temperature is slightly higher, due to thermal radiation from the beamline and the radioactive heating of the sample (at NICOLE, during the ^{68}Cu experiment the base temperature was 8 mK). The process of cooling the refrigerator from room temperature to base temperature is outlined next:

- Pump all vacuum chambers so no impurities from the atmosphere condense on the inside.
- Fill the liquid nitrogen jacket, cooling the whole apparatus to 77 K.
- Fill the main bath with liquid He, also cooling the superconducting magnet to operating temperatures.
- Pump the 1 K pot further lowering the temperature to 1.2 K.
- Start the circulation of the mixture. By pumping the still the mixture temperature will drop, reaching the base temperature.

3.2.2 Magnetic field

The magnetic field in the NICOLE setup is provided by a split coil superconducting magnet positioned around the sample holder with the field lines parallel to the plane of the sample foil. It can provide magnetic fields up to 2 T, although for the experiments only 0.1 T field was used. This reduces its effect on the electron's trajectories while still maintaining close to full magnetization of the Fe foil. The total field B_{tot} the implanted nuclei experience can be written in the following form

$$B_{tot} = B_{ext} + B_{hf} + B_{dem} + B_{KS} \quad (3.21)$$

and has several components:

- the *external field* (B_{ext}) which was set to 0.100(2) T at all times.
- the *hyperfine field* (B_{hf}) is the magnetic field induced by the atomic electrons. Its value for Cu impurities in a Fe foil was recently determined to be $-21.794(10)$ T [57]. The same article also gives an upper limit of 3×10^{-3} for the hyperfine anomaly for the three Cu isotopes: 59, 69 and 71. Earlier a measurement of ^{63}Cu and ^{65}Cu gave an upper limit of 5×10^{-5} [58]. Based on the measurements of magnetic moments of the Cu isotope chain [59] we can estimate the hyperfine anomaly between two isotopes ${}^1\Delta^2$ using the following relation:

$${}^1\Delta^2 = \frac{A_1 J_1 \mu_2}{A_2 J_2 \mu_1} - 1 \quad (3.22)$$

where J_1 and J_2 are the spins and μ_1 and μ_2 the magnetic moments of the nuclei, while A_1 and A_2 are the hyperfine parameters. Calculating with respect to ^{63}Cu , for both isotopes the hyperfine anomaly is less than 1.5×10^{-4} which is two times smaller than the relative error of the magnetic moments of the isotopes in question and 4 times smaller than the relative error of the hyperfine field and so can be neglected.

- the *demagnetization field* (B_{dem}) arises when a piece of ferromagnetic material is magnetized and is induced by the free magnetic poles at the edges of the material. It is proportional to the external field with an opposite sign. For a thin foil with dimensions $a > b \gg c$ (c being the foil thickness) analytical expressions can be found in [60, 61]. For the foil used in our Cu experiment the B_{dem} field was $-0.018(4)$ T, with a 20% error in order to account for the approximations made in deriving the analytical formulas in [60].
- the *Knight shift* (B_{KS}) describes the reaction of the conduction electrons to the external magnetic field and is proportional to this. Its value has never been determined for copper in iron at low temperatures. However, a 5% upper limit induces a 5 mT systematic error on the total magnetic field.

Combining all the above effects, the total magnetic field becomes $-21.712(12)$ T.

3.2.3 Detectors

Three custom made planar HPGe detectors [62, 63] were used for the detection of the β particles. They were mounted at 15° (Right), 90° (Bottom) and 175°

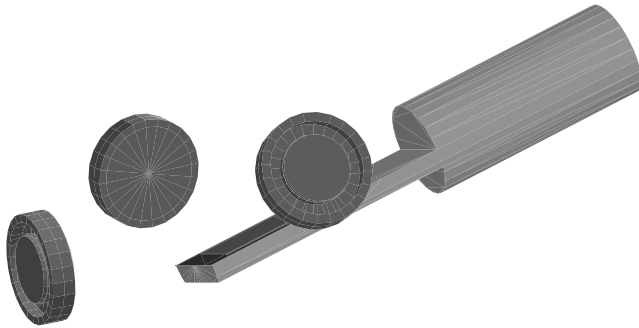


Figure 3.2: The three planar HPGe detectors surrounding the sample foil which is soldered to the sample holder.

(Left) with respect to the external magnetic field. The position of the Right and Left detectors, from the perspective of the asymmetry measurement, should have been 0° and 180° respectively. However, in that case the electrons arriving to them would have been subject to much more scattering in the sample foil. Therefore the Bottom detector is also rotated by 15° with respect to the plane of the foil, perpendicular to the horizontal external magnetic field. All three detectors are shown on figure 3.2 together with the sample holder and the foil. They were extensively characterized in previous test measurements [43].

3.2.4 Thermometry

In precision LTNO measurements knowledge of the sample temperature is crucial since the degree of polarization and so the value of B_1 coefficient depends on it. While the measurement of the β -asymmetry is used to search for exotic physics, the γ -asymmetry, which is governed by the electromagnetic interaction, can be used for temperature determination. The degree of orientation is determined by the temperature via the Boltzmann distribution thus providing an absolute thermometer. A more detailed discussion on NO thermometers can be found in [64].

In this experiment a $^{57}\text{Co}(\text{Fe})$ nuclear thermometer was used. It is pure electron capture decay and so does not contribute to the β spectrum observed by the particle detectors. The thermometer was prepared by diffusing the Co activity into an 99.99% pure Fe foil. Such a thermometer needs to be calibrated, since the fraction (see subsection 3.1.5) of the nuclei which feel the orienting interaction in a priori unknown. A $^{60}\text{Co}(\text{Co})$ thermometer, produced by neutron activation of a single crystal of ^{59}Co , so that the fraction of ^{60}Co nuclei at substitutional

lattice sites is exactly 1, was used for calibration. By recording the temperature dependence of the the asymmetry of the γ -rays of both isotopes the fraction of the $^{57}\text{Co}(\text{Fe})$ was determined to be 0.9340(30). The thermometer is soldered to the back of the sample holder, close to the sample foil.

Usually the asymmetry of the 136.5 keV γ -line of ^{57}Co is used for thermometry. This is a pure E2 transition, and the high accuracy of the deorientation and angular distribution coefficients outweighs its relatively weak intensity compared to that of the mixed M1/E2 122 keV γ transition.

Chapter 4

Geant4 Monte Carlo simulations

Monte Carlo methods are computational algorithms that rely on random sampling to compute their results. As such, they can provide numerical solutions to problems which can be described as the time evolution of objects interacting with other objects based on their object-object interaction mechanisms. The Geant4 (Geometry and Tracking) software framework [65, 66] relies on this technique to simulate the passage of particles through matter. Using databases and theoretical models of cross sections and other quantities, it can successfully reproduce the response of detectors to different types of radiation thus providing information necessary in the processes of data analysis, detector design, etc. Geant4 is developed by an international collaboration and its main purpose is the simulation of detector response in a typical high energy experiment, such as the ones situated at the Tevatron and LHC accelerators. However, its modular nature and the broad scope of its physics models enables its use in other related areas: nuclear physics, nuclear medicine, etc.

As the accuracy of experiments focusing on low energy tests of the Standard Model increases, a more detailed investigation of the related systematic effects is necessary. This process frequently includes Monte Carlo simulations, often employing the Geant4 software framework. A significant amount of these experiments measure correlations in neutron and nuclear β decay, therefore they are focusing on tracking and detection of β particles. One of the dominant systematic effects in such experiments is the electron scattering on energy sensitive detectors, therefore often the entire experimental apparatus is modeled within Geant4. The flexibility of the software toolkit allows quick and easy

modifications to the geometrical model of the experimental setup, permitting the user to completely assess the related systematic effects. Therefore, with the help of Geant4 simulations a deeper understanding can be obtained about the setup thus increasing the confidence in one's results. Furthermore, detailed studies can be performed for optimization purposes at the design stage of an experiment (see e.g. chapter 6).

Geant4 simulations played a crucial role in the analysis of β -asymmetry parameter measurements such as the one presented in chapter 5 or in Refs. [27, 24]. Therefore a more detailed investigation of the performance of Geant4 in simulating the response of particle detectors is necessary. After an introduction to Geant4 a paper submitted to Nuclear Instruments and Methods is included which presents the results of our investigation.

4.1 Introduction to Geant4

A more detailed introduction to the Geant4 framework can be found on the Geant4 website [66]. Here, only the details and modifications required for the simulation of a precision low energy experiment will be outlined.

As Geant4 simulates the transport of particles through matter, its core is a collection of models of (detailed) particle-particle and (more general) particle-matter interactions. The interaction processes can be assigned to the particles as desired, i.e. one can register only the bremsstrahlung process to electrons for testing purposes. Considering the precision correlation measurements in neutron and nuclear β decay, the β particles typically have around 1 MeV of kinetic energy, therefore the only relevant processes are of electromagnetic nature. All these models rely on a mixture of experimentally determined cross sections, interpolations and theoretical models. Detailed descriptions of each process can be found in the Geant4 Physics Reference Manual [67].

A set of processes is called a *Physics List* and several of them are maintained by the Geant4 developers:

- Standard - used for high energy physics experiments [68, 69] and applicable to energies as low as 1 keV.
- Livermore - extends the validity of the electromagnetic processes down to 250 eV, with more accurate descriptions of atomic effects and direct use of cross section data (the Standard physics list uses a parameterisation of these). This package used to be called the Low Energy physics list in version 9.0 and earlier [70].

- Penelope - being developed based on the Penelope simulation package [71]. Note that this package does not include the Penelope-specific electron multiple scattering algorithm.

It is to be noted that both Livermore and Penelope physics lists provide their own versions of several processes, such as ionization or bremsstrahlung [67, 72]. However, the multiple scattering processes are shared with the Standard physics list.

The multiple Rutherford scattering of electrons in matter is described by multiple scattering theories developed by Goudsmit and Saunderson [73] and later Lewis [74]. Both of these theories describe the individual scattering events by using Legendre polynomials, with their additive properties leading to an analytical solution of the final deflection angle after several scattering events. The Lewis theory provides the moments of the spatial displacement distribution as well. Simulation of the individual Rutherford scattering events in Geant4 is possible by registering the Single Scattering [75, 76] process to electrons and positrons. However, this is only practical for situations where the number of electron-electron collisions is low, e.g. for thin foils or low energy electrons. Since these conditions are in general not fulfilled, the multiple scattering (MSC) models were also implemented [77, 67]. These models average out the individual scattering events thus allowing the steps to be longer and the simulation to run faster. The MSC models should therefore provide information about the angular deflection, true path length correction and spatial displacement of the electron. These models are not exact and are responsible for most of the electron transport uncertainties [67], affecting quantities such as the backscattering coefficient.

The recent MSC models implemented in Geant4 are specific to a particle type, i.e. electrons, hadrons and muons. In this paper we will focus on the electron MSC models available in Geant4 version 9.5:

- Single Scattering - simulates individual Rutherford scattering events, based on screened nuclear potentials, according to the Penelope code [78].
- Urban MSC model - the default model within Geant4 is based on the Lewis MSC theory [74], and is applicable to all particles. Its performance has been validated against data obtained in thin foil transmission experiments [79]. However, the majority of these experiments were carried out using primary beams of energies above 1 MeV.
- Goudsmit-Saunderson MSC model - based on the theory developed by Goudsmit and Saunderson [73] and is applicable only to electrons and positrons. It uses a database of cross sections generated by the ELSEPA code [80].

It is to be noted that the choice of the MSC model is independent of the physics list.

An *event* is the basic unit of a simulation, which consists of several primary particles with user-defined properties, such as kinetic energy, momentum direction, position and others. A beam of monoenergetic electrons would be best modeled with one primary electron in each event, recording the deposited energy in the detector after every event. A more complex event, e.g. the decay of ^{60}Co , would involve 3 primary particles: an electron (with random kinetic energy according to the β spectrum shape) and two γ rays of 1173 and 1332 keV. If one records the deposited energy in the detector after each event, the true coincidences between any three primary particles would be correctly taken into account.

Geant4 tracks the primary particles throughout the geometry, taking into account the registered processes for each type of particle. A particle's track is composed of *steps* - straight line segments. The length of each step, which is intuitively connected to the accuracy of the simulation, is defined dynamically, i.e. it is determined by polling the processes active for the given particle. All these processes propose a step length (certainly a function of particle energy, material, etc.), and the tracking mechanism selects the shortest one of these. There is no built in cut for tracking, therefore Geant4 tracks all particles down to zero kinetic energy.

4.1.1 Simulation parameters

Like any simulation software, Geant4 also has several simulation parameters which can be optimized for good accuracy in a given energy region. In what follows the parameters relevant to our simulations will be discussed briefly.

The way Geant4 handles the creation of secondary particles (typically via the ionisation process) is controlled by the *Cut For Secondaries* (CFS) parameter, expressed in units of length. If a secondary particle would traverse in a given material a distance less than the CFS, it is not created but its energy is deposited locally. This reduces the amount of low energy secondaries created, speeding up the simulation. It is recommended to keep the value of this parameter below the linear dimensions of the smallest "sensitive" detector.

The parameter F_G determines the minimum amount of steps in every volume a particle enters. The parameters F_R and $Skin$ are used in electron multiple scattering models. F_R sets upper limits to the step length of electrons to a fraction of the electron mean free path. $Skin$ defines a region near volume

boundaries, in units of the electron mean free path, where the single Coulomb scattering process is used instead of multiple scattering.

4.2 Article I

In this section an article submitted to Nuclear Instruments and Methods, Section A will be included. It discusses in great detail the influence of the different physics lists and simulation parameters on the response of particle detectors to β radiation. The results of this investigation are relevant to the analysis of the β asymmetry parameter of ^{67}Cu , presented in chapter 5.

As precision experiments require the input of different persons with different sets of skills and expertise, so is the presented paper a result of a collective effort. My main contribution lies in the section on backscattering (section 3) and PIPS detector measurements (section 6). The section on HPGe detectors (section 5) is based on earlier but as yet unpublished results [43]. Furthermore, I drafted the full article and prepared it for submission. The manuscript has in the meantime been accepted for publication.

Performance of Geant4 in simulating semiconductor particle detector response in the energy range below 1 MeV

G. Soti^{a,*}, F. Wauters^{a,1}, M. Breitenfeldt^a, P. Finlay^a, I. S. Kraev^a, A. Knecht^{a,b}, T. Porobić^a, D. Zákoucký^c, N. Severijns^a

^a*Instituut voor Kern- en Stralingsfysica, KU Leuven, Celestijnenlaan 200D, B-3001 Leuven, Belgium*

^b*PH Department, CERN, CH-1211 Geneva 23, Switzerland*

^c*Nuclear Physics Institute, ASCR, 250 68 Rež, Czech Republic*

Abstract

Geant4 simulations play a crucial role in the analysis and interpretation of experiments providing low energy precision tests of the Standard Model. This paper focuses on the accuracy of the description of the electron processes in the energy range between 100 and 1000 keV. The effect of the different simulation parameters and multiple scattering models on the backscattering coefficients is investigated. Simulations of the response of HPGe and passivated implanted planar Si detectors to β particles are compared to experimental results. An overall good agreement is found between Geant4 simulations and experimental data.

Keywords:

Geant4, PIPS detectors, HPGe particle detectors, electron backscattering

1. Introduction

The search for physics beyond the Standard Model takes many forms. At the high energy frontier accelerators such as the LHC are able to produce new particles which could point toward new physics. The other, precision frontier relies on measurements of different observables, as e.g. in neutron and nuclear β decay, where a deviation from the Standard Model value is an unambiguous and model independent sign of new physics [1–6]. In order to further increase the precision of such measurements all possible systematic effects need to be evaluated, which often include Monte Carlo simulations such as the Geant4 software framework [7]. Among others it is widely used in neutron and nuclear correlation measurements [8–11] and in searches for neutrinoless double- β decay [12].

The majority of these experiments are focusing on tracking and detection of electrons with typical β decay energies (100 keV - 1 MeV) where one of the dominant systematic effects is the electron scattering from energy sensitive detectors. With the relative precision

*Corresponding author: gergelj.soti@fys.kuleuven.be

¹Current address: Department of Physics and Center for Experimental Nuclear Physics and Astrophysics, University of Washington, Seattle, Washington 98195, USA

of the Standard Model tests in neutron and nuclear β decay reaching the sub-percent level the accuracy of the Geant4 models needs to be re-evaluated and compared to new, high precision and high quality experimental data.

This work focuses on the influence of the various Geant4 models and their parameters on the simulated values of the backscattering coefficients. It also investigates the quality with which experimental spectra of different β decaying isotopes are reproduced. The results can be used to assign systematic errors to the simulations and also to estimate the systematic difference between simulated and experimental spectra.

2. Relevant Geant4 processes

Geant4 [7] is a toolkit for simulating the passage of particles through matter. It was developed with the experiments at the LHC accelerator in mind and is therefore tuned to simulate high energy physics experiments. However, low-energy weak interaction experiments in neutron and nuclear β decay that are dealing with β particles of around 1 MeV kinetic energy typically, can also benefit from information provided by Geant4. At these low energies the physical processes involved are greatly reduced in number: practically only the electromagnetic interaction remains active. In this paper we will therefore focus on the electromagnetic processes of Geant4 [13, 14]. Furthermore, we will focus on electron and γ ray related processes. The relevant processes for this energy range used in Geant4 are the photoelectric effect, Compton-scattering and pair creation for γ rays, while for electrons ionization, bremsstrahlung and scattering processes are included. Naturally all these processes are described by models, based on our current understanding of nature, but for practical purposes there will always be a compromise between realistic calculation time and the desired accuracy. A set of these models is called a physics list, and since version 9.3 of the Geant4 code these come in three flavors:

- Standard - used for high energy physics experiments [15, 16], but applicable to energies as low as 1 keV;
- Livermore - extends the validity of the electromagnetic processes down to 250 eV. This package used to be called the Low Energy physics list in version 9.0 and earlier [17];
- Penelope - being developed based on the Penelope simulation package [18].

The Standard electromagnetic packages have been already extensively tested in the energy range from 1 keV to 10 TeV [13], with the majority of the tests having been carried out at energies above 1 MeV.

When simulating low energy experiments as e.g. β decay, one first has to verify that the values of the various simulation parameters are suited for this energy range. The relevant parameters are [19–21]:

- Cut for Secondaries (CFS) - controls the way secondary particles are created, i.e. if a secondary particle would traverse in a given material a distance less than the CFS, it is not created but its energy is deposited locally. Therefore the value of this parameter

should be smaller than the linear dimensions of the smallest “sensitive” geometrical volume. Its default value is 1 mm, however, with typical detector thicknesses of about 1 mm as used in low energy experiments this value is obviously too large and a CFS value of e.g. 1 μm is more suited, as was observed before [22];

- F_R - limits the length of steps to a fraction of the electron mean free path. The default value is 0.04;
- F_G - determines the minimum amount of steps in a given volume. The default value is 2.5;
- Skin - region near volume boundaries where single Coulomb scattering is applied. The default value is 3 in units of the particle mean free path.

The scattering of electrons in matter is mainly an electron-electron process. Simulation of individual scattering events in Geant4 is possible by registering the Single Scattering [21, 23] process to electrons and positrons. However, this is only practical for situations where the number of electron-electron collisions is low, e.g. for thin foils or low energy electrons. Since these conditions are in general not fulfilled, several *condensed* multiple scattering (MSC) models were developed. These average out the individual scattering events thus allowing the steps to be longer and the simulation to run faster. However, the accurate sampling of the scattering angle, energy loss and lateral displacement is of paramount importance to the accuracy of the electron tracking, affecting quantities such as the backscattering coefficient. The recent MSC models are specific to a particle type, i.e. electrons, hadrons and muons. In this paper we will focus on the electron MSC models available in Geant4 version 9.5, i.e. the Urban, Goudsmit-Saunderson, and Single Scattering models [24, 25].

First, the performance of Geant4 with respect to electron backscattering will be investigated, considering the different physics lists, multiple scattering models and simulation parameters. Next, simulated spectra for different isotopes will be compared to experimental data obtained with both planar high purity germanium (HPGe) detectors and passivated implanted planar silicon (PIPS) detectors.

3. Backscatter comparisons

3.1. Introduction and literature review

In order to validate the Geant4 electron processes one needs simple experiments (both in terms of geometry and of the physics involved) and high-quality data. The best way to evaluate the Geant4 MSC models would be electron transmission experiments through thin foils [26]. We are in the process of preparing such an experiment.

Another, rather simple experimental observable related to electron processes is the backscattering coefficient. When an electron backscatters from the detector it deposits only part of its energy and then escapes from the detector, thereby distorting the shape of the measured electron spectrum. By simulating such a rather straightforward experiment the obtained backscattering coefficients can be directly compared to values cited in the literature.

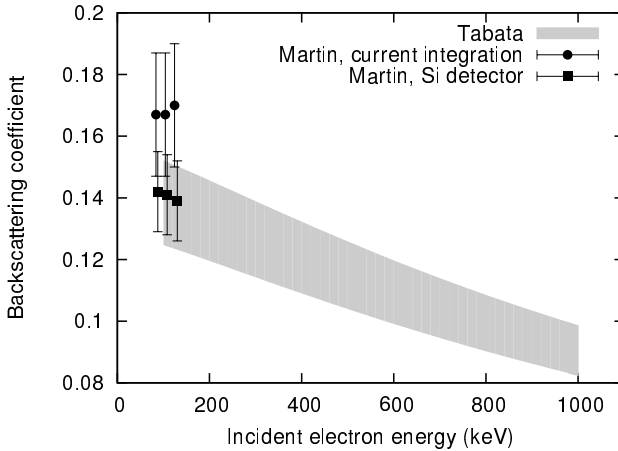


Figure 1: Backscattering coefficients for normal incidence electrons on Si. The shaded region marked Tabata is the 1σ interval of the backscattering coefficient calculated using the formulas given by Tabata [27]. The data points are experimental results from Martin et al. [28], where the “current integration” and “Si detector” refer to the methods used to arrive to the results.

Tabata et al. [27] gave an empirical formula based on available experimental data (see Ref. [27] and the references therein). The resulting backscattering coefficients for Si are shown as the shaded band in Figure 1. Note that the uncertainties of the fitted parameters listed in Ref. [27] induce relative uncertainties on the backscattering coefficients of about 10% (width of the shaded band). Seltzer et al. [29] presented backscattering and transmission results for foils of various materials. The Geant4 MSC models were validated against these data. However, no data for Si or Ge were included in Ref. [29]. The most recent papers about backscattering of low energy electrons are by Martin et al. [28, 30]. These authors measured the electron backscattering coefficients for silicon, beryllium and organic scintillators in the energy range from 40 keV to 130 keV, and their results for Si are also shown on Figure 1. It should be noted that no high-precision backscattering or transmission data for Si and Ge in the energy range between 150 keV and 1000 keV are currently available. However, the results from Martin et al. [28, 30] as well as our own previous work [8, 22, 31, 32] give good confidence in Geant4’s ability to reproduce experimental data with a precision that is typically of the order of 1 %.

3.2. Simulations

As a first step in investigating the performance of Geant4 with respect to electron backscattering we simulated a monoenergetic electron beam hitting a 1 mm thick slab of pure Si. Simulations were performed using Geant4 version 9.5 for all MSC models and the influence of the different simulation parameters listed in Section 2 were investigated as well.

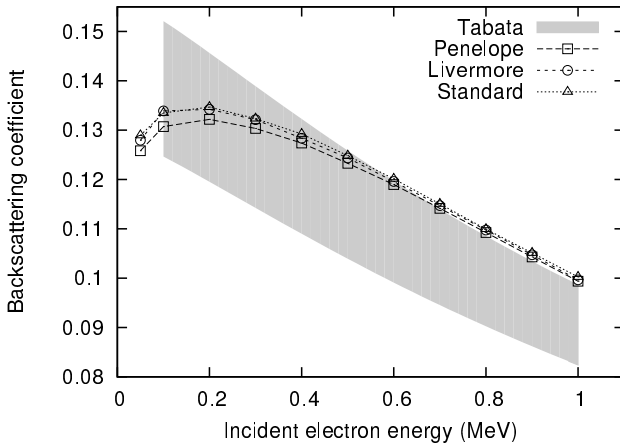


Figure 2: Backscattering coefficient in function of the incoming electron energy. Data are shown for the Standard, Livermore and Penelope physics lists, using the default MSC model.

3.2.1. Physics lists

The backscattering coefficient as a function of energy obtained for the different physics lists is shown in Figure 2. The differences are very small, with the Livermore and Standard physics lists providing almost identical results. A notable feature of all three curves is the decrease of the backscattering coefficient below 200 keV, which is unrealistic. This is an artifact of the Urban MSC model, as will be demonstrated further on.

3.2.2. Multiple scattering models

As the backscattering results do not significantly depend on the physics list used, we will further use the Standard physics list to study the different MSC models. The results for all four models are shown in Figure 3. For the Urban model a decrease in the backscattering coefficient is observed below 200 keV. This trend limits the usability of this model to energies above 100 keV. Further, a constant offset is visible compared to the other models as well as to the empirical relation; the reason for this is unclear. The Single Scattering model shows more stable behavior and also yields values closer to the central values obtained from the empirical relation of Tabata et al. [27], although the 10% uncertainty on the values calculated with this relation does not exclude the two other models. The Goudsmit-Saunderson model is found to exhibit a clear “staggering” effect which is not expected from physics grounds, rendering this model less interesting for applications that require high precision.

3.2.3. Simulation parameters

To investigate the effect of the different simulation parameters on the backscattering coefficient the Urban MSC model was used as it is the default model and also requires

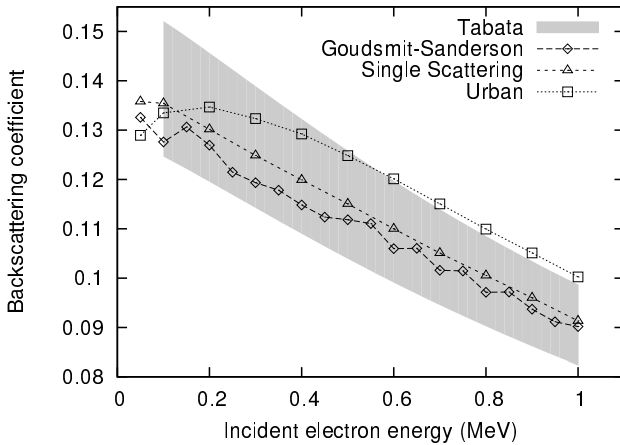


Figure 3: Backscattering coefficient as a function of the incoming electron energy, calculated with the Urban, Goudsmit-Saunderson and Single Scattering models within the Standard physics list.

the smallest calculation time. The dependence of the backscattering coefficients on the CFS value is shown in Figure 4. The fact that the backscattering coefficient increases with decreasing CFS value is expected (the smaller the CFS the more low energy secondaries are created). However, for a value of $1 \mu\text{m}$ it reaches the edge of the 1σ band of Tabata. To further investigate this difference, spectra of deposited energies for the backscattered events are shown in Figure 5 for the extreme cases $\text{CFS} = 1 \mu\text{m}$ and $\text{CFS} = 1 \text{mm}$. The effect of the different values of the CFS parameter is as expected, i.e. for smaller CFS values the probability for the electron to deposit a higher fraction of its initial energy increases (feature “A” on Figure 5). Despite the slightly worse agreement between the Tabata values [27] and the simulated data for $\text{CFS} = 1 \mu\text{m}$ we will for the time being continue to use the value of $1 \mu\text{m}$ for this parameter as it is considered more realistic for our purposes (e.g. the detector dead layer thicknesses are typically of the order of several 100 nm).

Simulation results for different values of the F_R parameter are shown on Figure 6. The backscattering coefficient is found to saturate when the F_R parameter drops below 0.002 (see Figure 6). The corresponding spectrum of deposited energies for the backscattered electrons (Figure 7) shows less events for incident electrons depositing only a small fraction of their initial energy (feature “A” in Figure 7) in the detector before being backscattered. Further, for $F_R = 0.04$ a sharp drop is observed below about 30 keV, which is not physical. Therefore, an F_R value between 0.01 and 0.002 seems realistic. A dedicated experiment focusing on these effects, so as to determine the best value, would be welcome.

Simulations performed for different values of the F_G and Skin parameters did not result in significant changes of the backscattering coefficient. Therefore, in subsequent simulations their default values (see Section 2) were used.

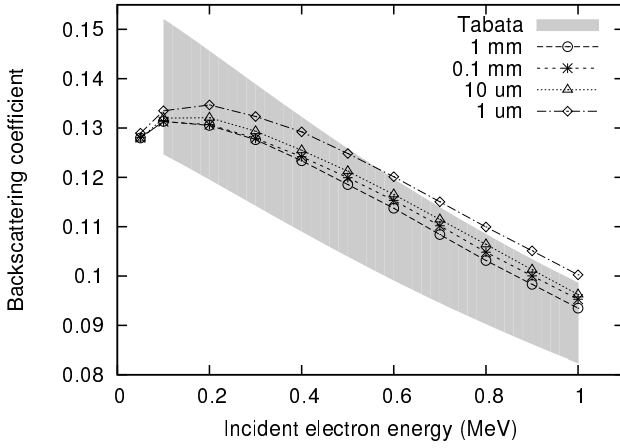


Figure 4: Backscattering coefficient as a function of the incoming electron energy for different values of the CFS parameter. Simulations were performed using the Standard physics list with the Urban MSC model.

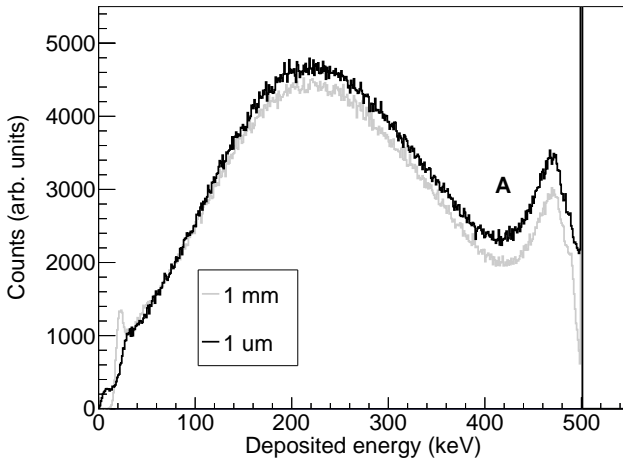


Figure 5: Spectrum of deposited energies for 500 keV incoming electrons. The default value for CFS of 1 mm is compared to our recommended value of 1 μm .

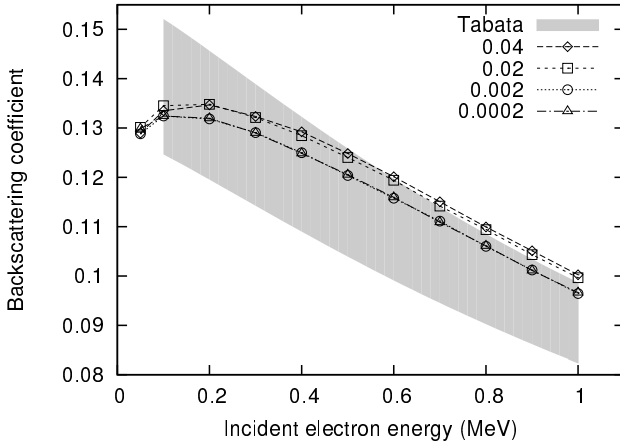


Figure 6: Backscattering coefficient as a function of the incoming electron energy for different values of the F_R parameter. Simulations were performed using the Standard physics list with the Urban MSC model.

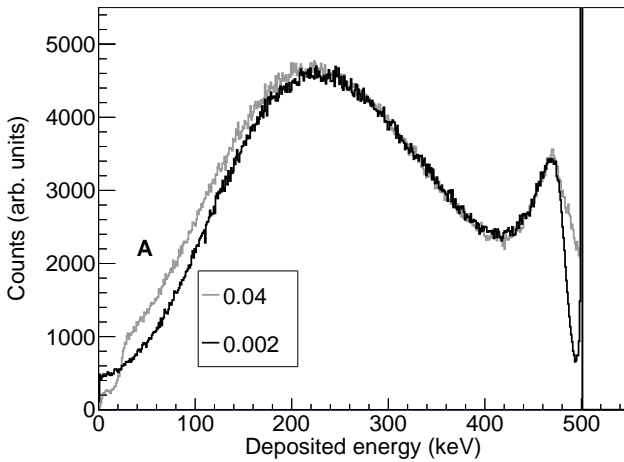


Figure 7: Spectrum of deposited energies for pure backscatter events for 500 keV normal incident electrons. The default value for F_R of 0.04 is compared to the value of 0.002.

3.3. Conclusions on the backscattering coefficients

The different MSC models and simulation parameters influence the backscattering coefficient at the 10% level, which is approximately equal to the uncertainty of the empirical relation of Tabata et al. [27]. The default value of the CFS parameter of 1 mm is too large if one uses typical particle detectors with thicknesses up to several mm. Furthermore, the typical dead layer thicknesses are much smaller, such that a more realistic value is around 1 μm . Simulations using this value for the CFS parameter produce backscattering coefficients in agreement with the results from the empirical relation. Based solely on the backscattering coefficients the best value for F_R can not be determined unambiguously. We therefore fix it for the time being at the default value of 0.04. The Single Scattering model agrees the best with the empirical equation of Tabata, but unfortunately it requires approximately 10 times more computer time than the Urban or the Goudsmit-Saunderson models.

4. Simulation of detector response

A Geant4 simulation records the energy deposited in a specified geometrical volume. Such a simulated spectrum, however, can not be directly compared to the measured spectrum since several instrumental effects as well as the decay scheme of the isotope considered still have to be taken into account.

4.1. Energy resolution

Geant4 does not take into account effects such as charge trapping in the detector or noise originating in the preamplifier and in the amplifier, all of which determine the energy resolution observed. Although Geant4 provides built-in classes to address these issues, we prefer another approach. The net effect of these random changes to the signal is best described by a Gaussian spread of the final simulated spectrum from Geant4. For the width of the Gaussian used to convolute that spectrum we use a value determined by a χ^2 fit to the conversion electron peaks from the decay of ^{207}Bi at 482 and 976 keV.

4.2. Pile-up

As will be seen in the following sections, even for a pure β spectrum, i.e. with no γ -rays being present in the decay scheme, often events above the endpoint energy are observed (see e.g. Figure 11). This is due to detector event pile-up, an artifact of signal processing. This effect can be accounted for in several ways. We prefer to deal with this in post processing, since it is then easy to change the pile-up probability thus accounting for changes in the source activity as, e.g., occurs in on-line experiments. One then introduces a probability that two random events from the spectrum are summed together. The magnitude of this probability is determined by the best fit to the region of the experimental spectrum above the β endpoint energy, or if a pulser peak is present, by the pulser peak-to-tail ratio.

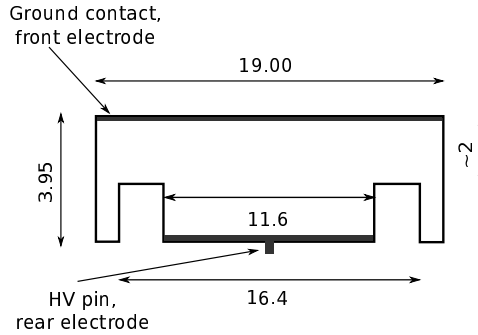


Figure 8: Dimensions of the 15/4 HPGe particle detector. All numbers are in units of mm.

4.3. Geant4 Radioactive Decay

Geant4 handles nuclear decays via the *G4RadioactiveDecay* process. This includes the different decay modes with their branching ratios and automatically generates decay products, such as α or β particles. Considering β -decay, besides the phase space factors only the Fermi function is implemented however. Therefore, in the studies concerning β decaying isotopes a custom made code was used [22] with the Fermi function and all higher order corrections implemented according to the prescriptions of Wilkinson [33–36].

5. Geant4 performance for planar HPGe detectors

Custom made planar HPGe detectors were developed [37, 38] for low temperature nuclear orientation β -asymmetry measurements. They were used in an experiment with ^{114}In [31] and in the $^{67/68}\text{Cu}$ experiment at ISOLDE, CERN [39]. All of them were extensively tested [40], and in this paper we will focus on the 15/4 detector. Figure 8 shows a sketch of the detector with all its dimensions noted. The detector has its front electrode made with boron implantation and the thickness of this dead layer is estimated to be ~ 100 nm. The thickness of the Li diffused dead layer at the rear electrode side of the detector was measured to be in the range of 0.7–0.9 mm. Simulations showed that a variation of 0.1 mm in this thickness does not change the response of the detector significantly. The sensitive area of the detector was modeled according to the results of a series of measurements with collimators of different size, further supported by COMSOL-Multiphysics [41] simulations.

The detector was positioned inside a vacuum chamber and a 1 mm thick Cu collimator with a 12 mm diameter circular hole was mounted in front of it. The role of this collimator is to stop the electrons arriving at the edge of the detector where the electric field might not be uniform and thus not all the charge created would be collected. The response of the detector was extensively tested at a temperature of 77 K with four different radioactive sources, i.e. ^{60}Co , ^{85}Kr , ^{90}Y and ^{207}Bi . The ^{207}Bi source was sandwiched between two $5.325 \mu\text{m}$ thick Ti foils in which the conversion electrons lose only about 2 keV energy. The ^{60}Co source was sandwiched between two, 10 μm thick mylar foils, leading to an energy loss for electrons of

about 3-4 keV. The ^{85}Kr source was a 0.05 mm thick iron foil in which the radioactive nuclei were implanted up to a depth of around 15 nm. The ^{90}Y source was prepared in-house by drying a small drop of liquid solution containing ^{90}Sr (which decays to ^{90}Y) inside a hole in a piece of aluminum of $25 \times 10 \times 1\text{mm}^3$. Thereafter the activity was covered with a 0.1 mm thin layer of epoxy.

5.1. Comparisons with Geant4

The detailed geometry of the entire setup (vacuum chamber, support structures, sources and detectors, see Figure 9) used to measure electron spectra with the different sources was implemented in Geant4. Simulations were then performed for each detector-source combination and the resulting histograms were normalized to the number of counts in an energy range depending on the isotope. For comparing the experimental to the simulated spectra we used the reduced χ^2 defined as:

$$\chi_{red}^2 = \frac{1}{\nu} \sum_i \frac{(y_i^{exp} - y_i^{sim})^2}{\sigma_{i,exp}^2 + \sigma_{i,sim}^2} \quad (1)$$

with ν the number of degrees of freedom, y_i^{exp} and y_i^{sim} the content of the i th bin in the experimental and simulated spectrum, respectively, and σ the associated uncertainty. In the ideal case χ_{red}^2 should be equal to unity. However, the measurements presented in this paper were performed to investigate the impact of the different Geant4 parameters, so that differences between experimental data and simulations larger than the statistical uncertainties can be expected. Although the χ_{red}^2 value can thus not be expected to be around unity, it can, however, still be considered as a relative figure of merit between simulations for different parameters or models being used.

5.1.1. ^{207}Bi

Reproducing the experimental spectrum obtained for this isotope is the most demanding job for Geant4 as the decay of ^{207}Bi produces X-rays, conversion electrons and γ rays over a wide energy range. Spectra obtained with these thin detectors are dominated by the conversion electrons, while the γ rays contribute mainly via the Compton effect. As this isotope decays via electron capture and because of its relatively complex decay scheme the standard radioactive decay module of Geant4 was used in the simulations. In Figure 10 the experimental and simulated spectra for the 15/4 detector are compared. Although the overall features are well reproduced for energies above 150 keV, clear differences between simulation and experiment are observed in some parts, especially near the Compton edges which are overestimated by the simulation.

5.1.2. ^{85}Kr

This isotope is suitable to check detector response to relatively low energy β particles (the endpoint energy of the ^{85}Kr decay is $E_0 = 687$ keV), without any disturbance from γ rays. However, the radioactive decay module of Geant4 does not generate the correct spectrum shape for this isotope as it does not decay via an allowed β transition but via a

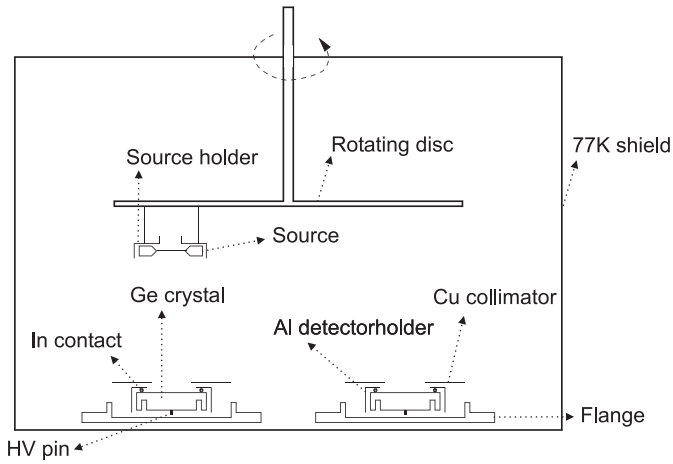


Figure 9: Sketch of the experimental setup used to measure electron spectra of different isotopes with HPGe detectors. The bottom plate of the vacuum chamber is connected to a liquid nitrogen bath allowing the detectors to be cooled to 77 K. The radioactive source is mounted on a rotating plate so it can be positioned above any of the detectors without the need for opening the system.

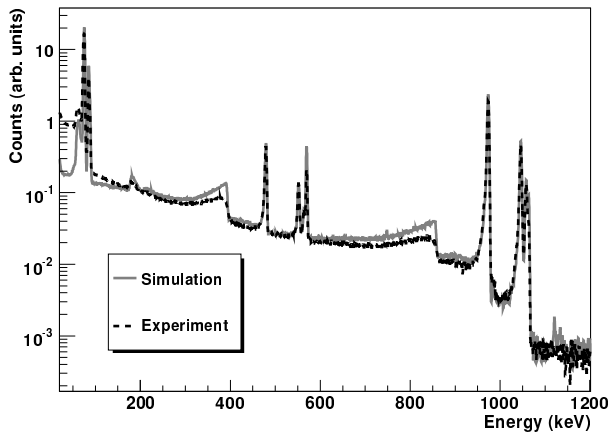


Figure 10: Comparison between experimental and simulated spectra of ^{207}Bi , for the 15/4 detector. The two main γ lines (at 569.7 keV and 1063 keV) are visible (highest energetic peak of the groups around 500 keV and 1000 keV), together with their K, L (and M) conversion electrons. Both γ rays generate Compton edges which are located at 394 and 857 keV, respectively. The $K\alpha$ and $K\beta$ X-ray lines are at 74 keV and at 85 keV. The spectra were normalized in the energy region from 50 to 1200 keV.

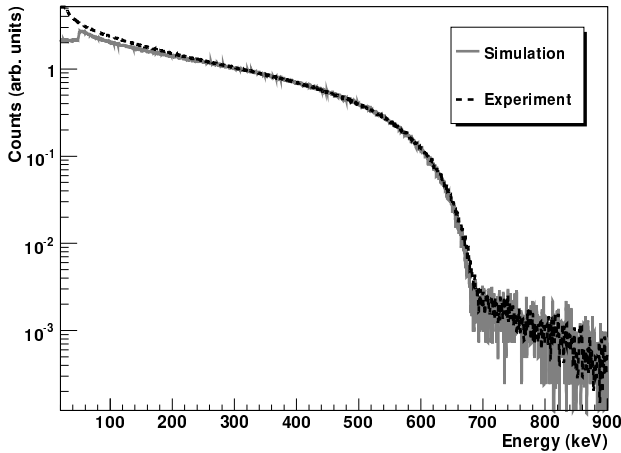


Figure 11: Comparison between the simulated and measured ^{85}Kr spectra for the 15/4 detector. The normalization region is 300-600 keV. In this region $\chi^2_{red} = 1.4$ with 74 degrees of freedom and simulation and experiment agree within 2%.

so-called first forbidden unique β transition, the spectrum shape of which is not included in Geant4. For this type of transitions the spectrum shape differs from the allowed one by a factor [42]

$$(W^2 - 1) + (W_0 - W)^2 \quad (2)$$

with W the total energy of the β particle and W_0 the total endpoint energy, both in units of the electron rest mass $m_e c^2$. After implementing the necessary correction factors the experimental and simulated spectra are found to agree within 2% (see Figure 11).

5.1.3. ^{90}Y

The isotope ^{90}Y (β endpoint energy $E_0 = 2.2$ MeV) was obtained as the decay product of ^{90}Sr (β endpoint energy $E_0 = 546$ keV). Only the decay of ^{90}Y was simulated and simulation and experiment were only compared in the part of the ^{90}Y β spectrum above the ^{90}Sr β endpoint energy. As ^{90}Y decays via a first forbidden unique β transition the same correction factors were applied to the Geant4 spectrum generator as in the case of ^{85}Kr . The accuracy of the simulations is rather limited for energies below 1 MeV (Figure 12). The upper 1 MeV of the spectrum can be reproduced with $\sim 5\%$ precision. Besides the fact that this is a first forbidden unique transition this observed difference could be in part due to the fact that the exact geometry of the source was known with much less precision compared to the other sources. Previous measurements [22] with ^{60}Co have shown that the measured spectrum is indeed rather sensitive to the detailed geometry of the source.

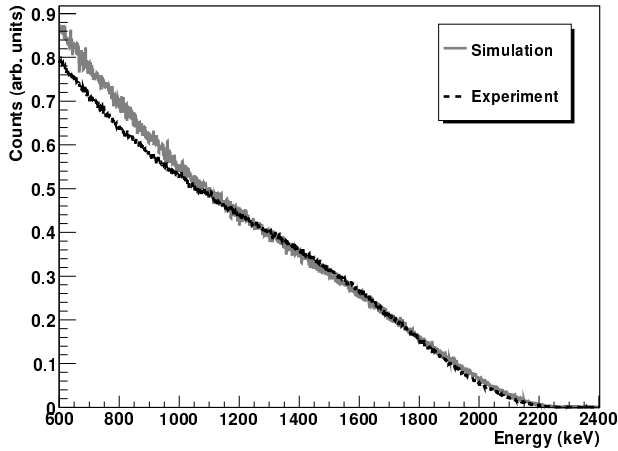


Figure 12: Comparison between the simulated and measured ^{90}Sr spectra for the 15/4 detector. The normalization region is 1200-2000 keV. In this region $\chi^2_{red} = 2.3$ with 532 degrees of freedom.

5.1.4. ^{60}Co

This isotope is very well suited to test the performance of the Geant4 code for low energy β particles due to its relatively simple decay scheme. The β endpoint energy is 318 keV which is much lower than the energies of the two strong γ lines (1.173 and 1.332 MeV) in the decay of this isotope. The problem of subtracting the Compton background caused by these γ rays significantly contributed to the error budget in past experiments [8].

Figure 13 shows the upper part of the beta spectrum together with part of the Compton background. In the “A” region (from 150 keV to 300 keV) the difference between simulation and experiment is around 5%. At energies below 150 keV the difference becomes much larger. This can be due to several reasons:

- a problem with simulating the backscattering of low energy electrons (see sec. 3), or
- the Compton plateau not well being reproduced by the simulations (see sec. 6.2.1).

A significant difference between simulation and experiment can be observed in the intensity of the Compton background (region “C”), where the simulation shows a clear excess of counts. This effect was observed before with Si detectors [8, 22] as well.

5.2. Conclusions for HPGc detectors

The general features of all measured spectra are rather well reproduced by the Geant4 simulations. The high energy part of the β spectra are typically reproduced at the 2-3% level. However, the lower half of the β spectra are typically much less well reproduced

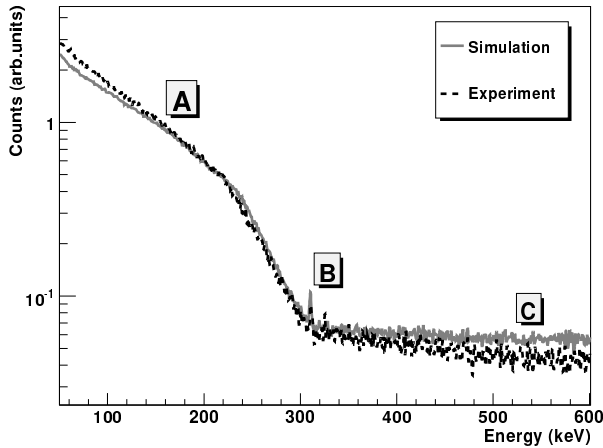


Figure 13: Comparison between the simulated and measured ^{60}Co spectra for the 15/4 detector. The small peak (marked “B”) at 310 keV is the double escape peak of the 1332 keV γ line. The normalization region is 150-300 keV. In this region $\chi_{red}^2 = 2.8$ with 150 degrees of freedom.

in simulations. A possible reason for this could be the inaccuracy of the backscattering coefficients at these energies, see Section 3.

The distinct difference between simulation and experiment in the spectrum of ^{207}Bi near the Compton edge of the two γ rays points toward the inaccuracy of the Compton scattering cross sections, which is further emphasized by the relatively high Z value of Ge.

The observed differences between the experimental and simulated spectra for a HPGe detector are found to be much larger than the small effects related to the choice of values for the Geant4 parameters. Therefore, unfortunately, no additional information on the best values of these parameters can be obtained in this case.

6. Geant4 performance for PIPS detectors

A 1.5 mm thick, fully depleted pure PIPS detector (MSX03-1500, from Micron Semiconductor) was recently tested by our group, in part to replace the Hamamatsu 0.5 mm thick PIN diode detectors [8, 31]. The front dead layer of this detector is 100 nm thick. The entrance window consists of a 300 nm thick Al grid with a 3% coverage. This detector is well suited for precision β spectroscopy because the low Z values of Al and Si limit the probability for electron backscattering from the entrance window. It is further able to fully stop up to 800 keV electrons.

The detector was tested in the same vacuum chamber used for testing the HPGe detectors and again at 77 K (see Section 5 for more details). A 0.8 mm thick Cu collimator with a 9 mm diameter circular hole was mounted in front of the detector.

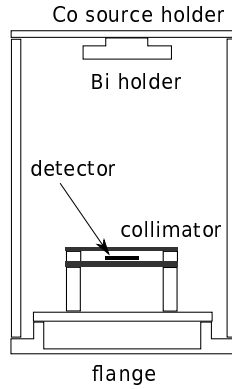


Figure 14: Sketch of the experimental setup used to measure ^{207}Bi and ^{60}Co spectra with the PIPS detector. The detector-source distance is 71 mm. The entire setup was positioned in a cryostat and cooled to 77 K in order to reach full detector depletion.

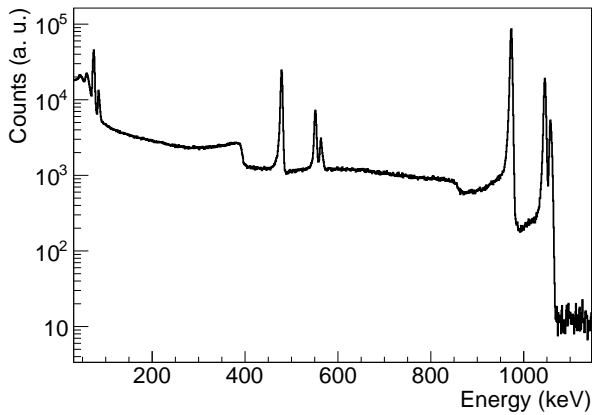


Figure 15: The ^{207}Bi spectrum registered with the PIPS detector operating at 77 K. The two main γ lines (at 569.7 keV and 1063 keV) are not visible, but their K, L and M conversion electrons generate the two groups of peaks. The Compton edges of both γ rays are also visible. The $K\alpha$ and $K\beta$ X-ray lines are visible at 74 keV and at 85 keV, respectively. Detector resolution (FWHM) is 4 keV at 482 keV.

Table 1: Simulated ratio of the ^{207}Bi conversion electron peaks K_{1063}/K_{569} for different depletion layer thickness of the PIPS detector. The χ_{red}^2 value shown is calculated according to Equation 1 when comparing the simulated spectra and the experimental spectrum taken at 77 K, for the energy region between 100 and 1100 keV. The statistical uncertainties on the simulated peak ratios are of the order of 1%. The experimental ratio is 3.78(11).

Depletion (mm)	Peak ratios	χ_{red}^2
1.39	3.71	23.1
1.43	3.83	17.1
1.47	3.94	13.5
1.50	3.98	11.5

6.1. Depletion

The spectra of ^{207}Bi measured with the detector at room temperature showed signs that the detector was not fully depleted. The conversion electron peaks were not of the expected intensity. Indeed, the experimental ratio of the K conversion electron lines K_{1063}/K_{569} was 0.998(14), in clear disagreement with the expected value of about 3.8, when assuming full depletion and taking into account the detection efficiency and backscattering probability at the different energies. The results of Geant4 simulations were supporting the assumption of partial depletion at room temperature, allowing to estimate the depletion thickness to be around 0.8 to 0.9 mm. After cooling the setup to 77 K (Figure 15) the experimental conversion peak ratio became 3.78(11), fully consistent with the expected value and with the error being dominated by the uncertainties of the conversion coefficients [43]. In order to confirm full depletion, simulations were performed for slightly different depletion layer thicknesses. The comparison of these with experiment is summarized in Table 1. Values for the K conversion peak ratio very close to the experimental one are found. The best χ_{red}^2 for the comparison of simulated and experimental spectra is obtained for depletion thicknesses of about 1.50 mm, thus confirming the probably full depletion. Note that it was observed that this detector can also be operated with no significant drop in performance at liquid helium temperature (4 K) making it suitable for e.g. future β -asymmetry measurements using the low temperature nuclear orientation technique.

6.2. Comparisons with Geant4

Two spectrum measurements were performed with the PIPS detector (at 77 K), one with ^{60}Co , the other with ^{207}Bi , since the source geometry was best known for these two cases. For simulating the spectra for these isotopes, the vacuum chamber with support structures as well as detailed detector and source descriptions were again modeled in Geant4 version 9.5. In all cases the Standard physics list was used.

6.2.1. ^{60}Co

A Si detector is suitable for precision β decay measurements with ^{60}Co since the low energy β -rays of this isotope will be fully stopped if the detector is at least 0.5 mm thick. The two gamma lines at 1.173 and 1.332 MeV will not create visible peaks, although their

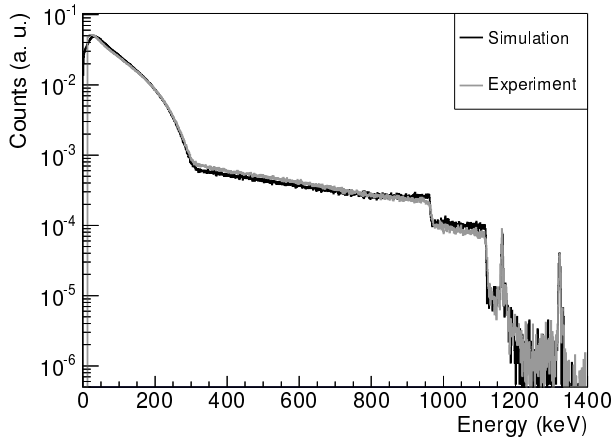


Figure 16: Comparison between the simulated and measured spectra of ^{60}Co for the PIPS detector. The β endpoint energy is 317.9 keV. The two peaks at 1162 and 1320 keV are the conversion electrons of the two γ -rays at 1173.2 and 1332.5 keV, respectively. The γ peaks are estimated to be ~ 20 times weaker than the conversion peaks. The simulation was performed with the Standard physics list and the Urban MSC model, while the simulation parameter values were set according to Section 2 with CFS fixed at $1\ \mu\text{m}$. Both spectra were normalized to the number of counts in the energy region of 150-300 keV.

conversion electrons do appear in the spectrum obtained with the 1.5 mm thick Si detector. Figure 16 shows the experimental and the simulated spectrum of ^{60}Co for the PIPS detector. The simulations were obtained using the Standard physics list and the Urban MSC model with the default values for the simulation parameters mentioned in Section 2 (i.e. $\text{CFS} = 1\ \mu\text{m}$, $F_R = 0.04$, $F_G = 2.5$ and $\text{Skin} = 3$). The clear difference in the region of the spectrum dominated by Compton events (i.e. above 320 keV) was further investigated by positioning a 3 mm thick plastic (PVC) absorber between the detector and the source in order to block the β rays. Keeping in mind that the PVC absorber slightly increases the Compton background in both simulations and experiment, one can subtract the spectrum with absorber from the regular one by normalizing the spectra in the energy region above the β decay endpoint (i.e. between 350 and 600 keV). This procedure reduces the influence of the Compton events to a second order effect, so that the difference between simulation and experiment is now below 5% in the region from 50 to 318 keV and below 3% when normalizing between 150 and 300 keV (see figure 17).

6.2.2. Comparison of MSC models, physics lists and Geant4 parameters

The fact that simulated and experimental spectra agree up to 3% for the case of ^{60}Co (Figure 17) allows comparing the effect of different types of Geant4 simulation parameters on the simulated spectra. We therefore investigated the influence of the different physics

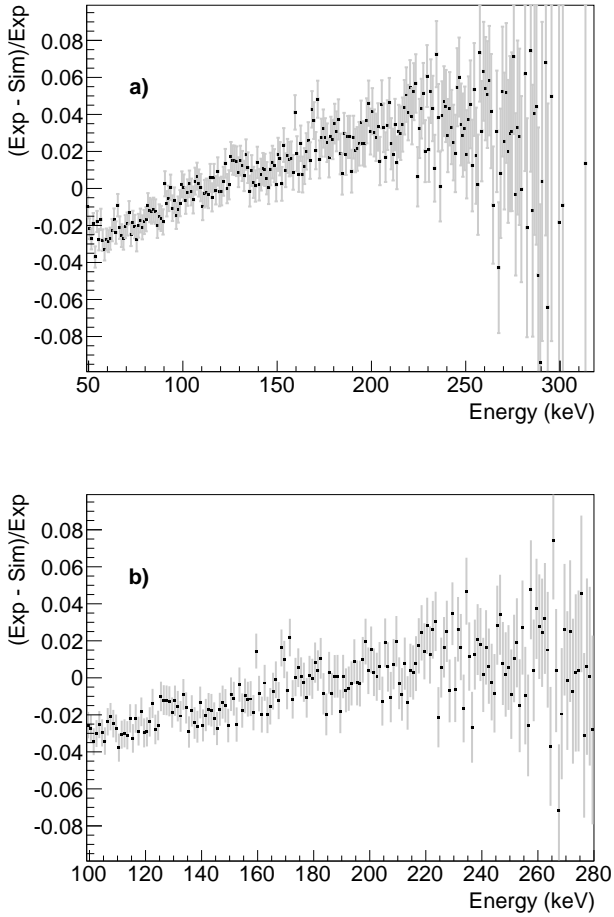


Figure 17: Relative difference between simulated and experimental spectra of ^{60}Co for the 1.5 mm PIPS detector. The experimental and simulated results were obtained by subtracting spectra with and without a 3 mm thick PVC absorber between the source and the detector. Simulations used the Single Scattering model, while the other parameters were set according to Section 2, with CFS fixed at $1\ \mu\text{m}$. Panel a) was normalized in the region between 50 and 318 keV yielding $\chi_{red}^2 = 4.1$ for 268 degrees of freedom. Panel b) was normalized between 100 and 280 keV with $\chi_{red}^2 = 1.6$ for 180 degrees of freedom.

lists and MSC models, as well as of the values of the different simulation parameters.

Performing simulations with the different physics lists it was found that, similar to the backscattering coefficients, the simulated spectra of ^{60}Co were not significantly influenced by the choice of the physics list, i.e. similar χ_{red}^2 values were obtained for both energy regions and for all three physics lists; see Table 2. The amount of computing time required for physics lists other than the Standard one is found to be roughly two times larger.

In simulations performed using the different MSC models the χ_{red}^2 values listed in Table 3 were obtained. The Single Scattering and the Goudsmit-Saunderson models clearly outperform the Urban MSC model, yielding a χ_{red}^2 value that is up to about 50% smaller when the larger energy region from 50 to 318 keV is considered. The Goudsmit-Saunderson model performs similar to the Single Scattering model, but because of the straggling in the backscattering coefficients (see Figure 3) it can not be recommended.

Comparing simulations performed with different CFS values the results that are summarized in Table 4 were obtained. Keeping in mind that a CFS value of 1 mm is too large when simulating the performance of detectors which are only several mm thick, the best value for the CFS is found to be around 10 μm to 0.1 mm, with a preference for the smaller value in view of this size issue.

Finally, simulations were performed for $F_R = 0.002$ and for the default value of 0.04, resulting in $\chi_{red}^2 = 6.3$ and 7.75, respectively, for the energy region of 50 to 318 keV. This difference being less significant than the differences in χ_{red}^2 obtained when varying the physics lists, the MSC models or the CFS value we suggest to keep the default value for F_R . The F_G and Skin parameters were found not to influence significantly the simulated spectra.

In order to investigate the accuracy of the electron processes within Geant4 in greater detail, experimental data for pure ground state to ground state β transitions are required so that no Compton effect has to be considered.

Table 2: χ_{red}^2 values obtained by comparing experimental and simulated spectra of ^{60}Co in two different energy regions, using the Standard (Std.), Penelope (Pen.) and Livermore (Liv.) physics lists. The CFS was set to 1 μm , while the F_R , F_G and Skin simulation parameters were set at their default values given in Section 2.

Region (keV)	Std.	Pen.	Liv.
150–300	1.53	1.13	1.31
50–318	7.75	7.14	7.97

6.2.3. ^{207}Bi

This isotope is the most demanding for Geant4, as was already discussed in Section 5.1. Figure 15 shows the experimentally obtained spectrum, while Figure 18 shows the difference between simulation and experiment. In the region of the spectrum dominated by the X-rays (at 75 and 85 keV) the difference increases to 40%, while in the higher energy region it is around 10%.

The most significant difference is observed in the region of the Compton plateau of the 569.7 keV γ line, i.e. the energy region up to about 400 keV. Further, the Compton edge

Table 3: χ_{red}^2 values obtained by comparing experimental and simulated spectra of ^{60}Co in two different energy regions, using the Standard physics list with the Urban, Goudsmit-Saunderson (G-S) and Single Scattering (SS) MSC models. The CFS was set to $1\ \mu\text{m}$, while the F_R , F_G and Skin simulation parameters were set at their default values given in Section 2.

Region (keV)	Urban	G-S	SS
150–300	1.53	1.25	1.10
50–318	7.75	3.71	4.76

Table 4: χ_{red}^2 values obtained by comparing experimental and simulated spectra of ^{60}Co in two different energy regions, using the Standard physics list with the Urban MSC model, for values of the CFS parameter ranging from $1\ \mu\text{m}$ to 1 mm. The F_R , F_G and Skin simulation parameters were set at their default values given in Section 2.

Region (keV)	$1\ \mu\text{m}$	$10\ \mu\text{m}$	0.1 mm	1 mm
150–300	1.53	1.03	1.07	1.13
50–318	7.75	4.83	3.09	3.28

in the simulated spectrum is much sharper and more intense by $\sim 15\%$. Using different physics lists was found to yield slightly different results. E.g. the spectrum generated with the Livermore physics list displays a smoother Compton edge than the Standard one, in better agreement with the experimental spectrum (see Figure 19). However, the difference in the intensity of the Compton edge is still of the order of 10%. The Penelope physics list was found to produce very similar results.

7. Conclusions and outlook

The influence of the various Geant4 physics lists, MSC models and parameters on simulated electron backscattering coefficients from Si for energies in the range of nuclear β decay was investigated. It was found that for the energy region of typical low energy experiments in neutron and nuclear β decay the usage of the low energy physics lists - Livermore and Penelope - is not absolutely required. Best agreement between the simulated results and experimental data is found for the Single Scattering model, although the other MSC models are also within the (still rather large) experimental uncertainty. The default value for CFS, which is 1 mm, should be lowered for geometrical reasons and our recommended value is around $10\ \mu\text{m}$. Our recommended value for the F_R parameter is in the range between 0.01 and 0.002. High precision experimental data on backscattering, but also on transmission through thin foils, in the energy range of 100 and 1000 keV would be very useful for further investigation. Such a project is currently being prepared using a β spectrometer which combines an energy sensitive detector and a multi-wire drift chamber similar to the one described in Refs. [44, 45].

Simulations of the response of semiconductor particle detectors (3 mm thick HPGe and 1.5 mm thick PIPS) were also compared to experimental data. A general good agreement

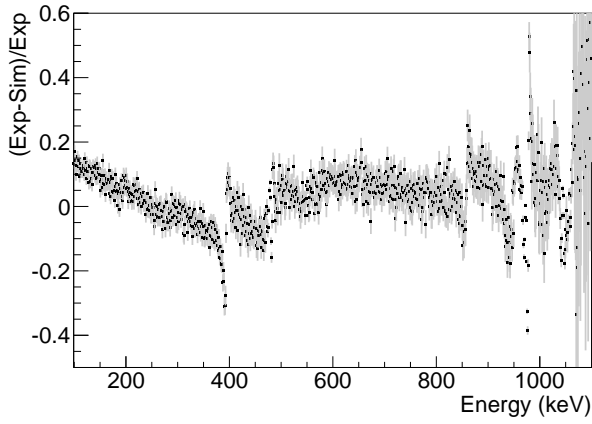


Figure 18: Relative difference between the experimental and simulated spectrum for ^{207}Bi . Simulation parameters were set according to Section 2. The normalization region is from 100 to 1100 keV. The spikes visible at around 400 and 860 keV are the differences near the Compton edges; see text and Figure 19 for details.

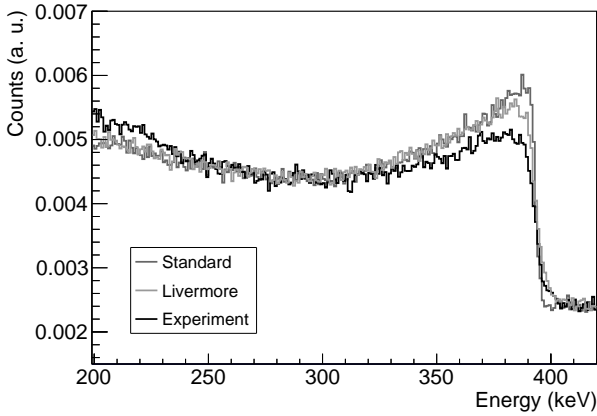


Figure 19: The Compton edge of the 569.7 keV γ line of ^{207}Bi , measured using the PIPS detector. The simulated spectra were obtained using the Standard and the Livermore physics list with the Urban MSC model.

was found for electron processes, while for γ processes significant differences were observed in the region of the Compton edge. The overall worse agreement for HPGe detectors is not surprising due to the higher Z value of Ge, since both electron and γ processes are Z dependent.

The observed good accuracy that was found for the electron processes in Geant4 now allows for direct precision measurements of the β spectrum shape. For the case of a pure β emitter, with no γ rays in its decay, the dominant systematic effect remaining is the backscattering from the energy sensitive detector. Combining then the detector with a system that identifies backscattered events (such as the multi-wire drift chamber mentioned above [44, 45]) enables performing high precision measurements of the β spectrum shape. Such experiments are currently being prepared. These would allow to address the Fierz interference term that is sensitive to scalar and tensor type components in the weak interaction [46], and to study the effect of the so-called recoil terms [47] in nuclear β decay.

Acknowledgments

This work was supported by the Fund for Scientific Research Flanders (FWO), Projects GOA/2004/03 and GOA/2010/10 of the K. U. Leuven, the Interuniversity Attraction Poles Programme, Belgian State Belgian Science Policy (BriX network P6/23), and Grant LA08015 of the Ministry of Education of the Czech Republic.

- [1] N. Severijns, M. Beck, O. Naviliat-Cuncic. *Reviews of Modern Physics* 78 (2006) 991–1040
- [2] H. Abele. *Progress in Particle and Nuclear Physics* 60 (2008) 1–81
- [3] J. S. Nico. *Journal of Physics G: Nuclear and Particle Physics* 36 (2009) 104001
- [4] G. Konrad, *et al.* In R. V. H. V. Klapdor-Kleingrothaus, I. V. Krivosheina, ed., *Physics Beyond the Standard Models of Particles, Cosmology and Astrophysics (Proc. 5th Int. Conf., Beyond 2010)* (2010)
- [5] N. Severijns, O. Naviliat-Cuncic. *Annual Review of Nuclear and Particle Science* 61 (2011) 23–46
- [6] N. Severijns, O. Naviliat-Cuncic. *Physica Scripta* T152 (2013) 014018
- [7] S. Agostinelli, *et al.* *Nuclear Instruments and Methods in Physics Research, Section A: Accelerators, Spectrometers, Detectors, and Associated Equipment* 506 (2003) 250 – 303
- [8] F. Wauters, *et al.* *Physical Review C* 82 (2010) 055502
- [9] D. Rodríguez, *et al.* *The European Physical Journal A* 42 (2009) 397–400. 10.1140/epja/i2009-10733-6
- [10] B. Plaster, *et al.* *Physical Review C* 86 (2012) 055501
- [11] G. Li, *et al.* *Physical Review Letters* 110 (2013) 092502
- [12] M. Bauer, *et al.* *Journal of Physics: Conference Series* 39 (2006) 362
- [13] J. Apostolakis, *et al.* *Journal of Physics: Conference Series* 219 (2010) 032044
- [14] K. Amako, *et al.* *Nuclear Science, IEEE Transactions on* 52 (2005) 910 – 918
- [15] H. Burkhardt, *et al.* *IEEE Symposium Conference Record Nuclear Science 2004*. 3 (2004) 1907–1910
- [16] J. Apostolakis, *et al.* In *CHEP’06* (2006)
- [17] S. Chauvie, *et al.* In *Nuclear Science Symposium Conference Record, 2004 IEEE*, volume 3 (2004) 1881–1885 Vol. 3
- [18] J. Sempau, *et al.* *Nuclear Instruments and Methods in Physics Research, Section B: Beam Interactions with Materials and Atoms* 132 (1997) 377 – 390
- [19] O. Kadri, *et al.* *Nuclear Instruments and Methods in Physics Research, Section B: Beam Interactions with Materials and Atoms* 258 (2007) 381 – 387
- [20] S. Elles, *et al.* *Journal of Physics: Conference Series* 102 (2008) 012009
- [21] V. N. Ivanchenko, *et al.* *Journal of Physics: Conference Series* 219 (2010) 032045

- [22] F. Wauters, *et al.* Nuclear Instruments and Methods in Physics Research, Section A: Accelerators, Spectrometers, Detectors, and Associated Equipment 609 (2009) 156 – 164
- [23] J. Apostolakis, *et al.* Journal of Physics: Conference Series 119 (2008) 032004
- [24] O. Kadri, *et al.* Nuclear Instruments and Methods in Physics Research, Section B: Beam Interactions with Materials and Atoms 267 (2009) 3624 – 3632
- [25] Geant4 Physics Reference Manual. <http://geant4.cern.ch/support/userdocuments.shtml>
- [26] L. Urbán. *private communication*
- [27] T. Tabata, R. Ito, S. Okabe. Nuclear Instruments and Methods 94 (1971) 509 – 513
- [28] J. W. Martin, *et al.* Physical Review C 68 (2003) 055503
- [29] S. M. Seltzer, M. J. Berger. Nuclear Instruments and Methods 119 (1974) 157 – 176
- [30] J. W. Martin, *et al.* Physical Review C 73 (2006) 015501
- [31] F. Wauters, *et al.* Physical Review C 80 (2009) 062501
- [32] F. Wauters, *et al.* Nuclear Instruments and Methods in Physics Research, Section A: Accelerators, Spectrometers, Detectors, and Associated Equipment 604 (2009) 563 – 567
- [33] D. Wilkinson. Nuclear Instruments and Methods in Physics Research, Section A: Accelerators, Spectrometers, Detectors, and Associated Equipment 275 (1989) 378 – 386
- [34] D. Wilkinson. Nuclear Instruments and Methods in Physics Research, Section A: Accelerators, Spectrometers, Detectors, and Associated Equipment 290 (1990) 509 – 515
- [35] D. Wilkinson. Nuclear Instruments and Methods in Physics Research, Section A: Accelerators, Spectrometers, Detectors, and Associated Equipment 365 (1995) 497 – 507
- [36] D. Wilkinson. Nuclear Instruments and Methods in Physics Research, Section A: Accelerators, Spectrometers, Detectors, and Associated Equipment 401 (1997) 275 – 280
- [37] D. Vénos, *et al.* Nuclear Instruments and Methods in Physics Research, Section A: Accelerators, Spectrometers, Detectors, and Associated Equipment 365 (1995) 419 – 423
- [38] D. Vénos, *et al.* Nuclear Instruments and Methods in Physics Research, Section A: Accelerators, Spectrometers, Detectors, and Associated Equipment 454 (2000) 403–408
- [39] G. Soti. *to be published*
- [40] F. Wauters. Search for tensor type weak currents by measuring the β -asymmetry parameter in nuclear decays. Ph.D. thesis, K.U. Leuven (2009)
- [41] COMSOL Multiphysics simulation environment. <http://www.comsol.com/products/multiphysics/>
- [42] L. M. Langer, H. C. Price. Physical Review 76 (1949) 641–646
- [43] F. Kondev, S. Lalkovski. Nuclear Data Sheets 112 (2011) 707 – 853
- [44] G. Ban, *et al.* Nuclear Instruments and Methods in Physics Research Section A: Accelerators, Spectrometers, Detectors and Associated Equipment 565 (2006) 711–724
- [45] K. Lojek, K. Bodek, M. Kuzniak. Nuclear Instruments and Methods in Physics Research, Section A: Accelerators, Spectrometers, Detectors, and Associated Equipment 611 (2009) 284 – 288
- [46] J. Jackson, S. Treiman, J. H. Wyld. Physical Review 106 (1957) 517 – 521
- [47] B. R. Holstein. Reviews of Modern Physics 46 (1974) 789–814

Chapter 5

The β asymmetry parameter of ^{67}Cu

As it was discussed in chapter 2, the value of the β asymmetry parameter A is sensitive to possible tensor type currents in the weak interaction Hamiltonian. Therefore the topic of this chapter is the measurement of the A parameter in the decay of ^{67}Cu . The experiment employed the method of low temperature nuclear orientation, which was outlined in chapter 3. Geant4 simulations were used in the data analysis, the quality of which was discussed in chapter 4. The experiment and the results obtained will be presented in the form of an article, which is to be submitted to Physical Review C.

Although the data for this experiment were collected before I started my PhD studies, I performed the analysis of these data, the Geant4 simulations, the investigation of the systematic error budget, and the interpretation of the final result. During my PhD studies I took part in another similar experiment to learn about the details of low temperature nuclear orientation method, which provided me with valuable information for the analysis of my own data. Finally I also drafted the full paper and prepared it for submission.

Measurement of the β -asymmetry parameter of ^{67}Cu in search for tensor type currents in the weak interaction

G. Soti,^{1,*} F. Wauters,^{1,†} M. Breitenfeldt,¹ P. Finlay,¹ A. Knecht,^{1,2} U. Köster,³ I. S. Kraev,¹ T. Porobic,¹ I. S. Towner,⁴ D. Zákoucký,⁵ and N. Severijns¹

¹*Instituut voor Kern- en Stralingsfysica, KU Leuven,*

Celestijnenlaan 200D, B-3001 Leuven, Belgium

²*PH Department, CERN, CH-1211 Geneva 23, Switzerland*

³*Institut Laue Langevin, 6 rue Jules Horowitz, F-38042 Grenoble Cedex, France*

⁴*Cyclotron Institute, Texas A&M University,*

College Station, Texas 77843, USA

⁵*Nuclear Physics Institute, ASCR, 250 68 Řež, Czech Republic*

(Dated: June 21, 2013)

Abstract

The β -asymmetry parameter \bar{A} for the pure Gamow-Teller decay of ^{67}Cu was measured by the low temperature nuclear orientation method. A ^3He - ^4He dilution refrigerator cooled down to milliKelvin temperatures an iron sample foil into which the radioactive nuclei were implanted. An external magnetic field of 0.1 T in combination with the internal hyperfine magnetic field oriented the nuclei. The anisotropic β radiation was observed with planar high purity germanium detectors operating at a temperature of about 10 K. An on-line measurement of the β -asymmetry of ^{68}Cu was also performed for normalization purposes. Systematic effects were investigated using Geant4 simulations. The result, $\bar{A} = 0.584(10)$ is in agreement with the Standard Model value of 0.5998(2) and is interpreted in terms of physics beyond the Standard Model. The limits obtained on possible tensor type charged currents in the weak interaction hamiltonian are $-0.002 < (C_T + C'_T)/C_A < 0.100$ (90% C.L.).

* Corresponding author: gergelj.soti@fys.kuleuven.be

† Current address: Department of Physics and Center for Experimental Nuclear Physics and Astrophysics, University of Washington, Seattle, Washington 98195, USA

I. INTRODUCTION

In their original paper Lee and Yang [1] formulated the most general β decay Hamiltonian supposing only Lorentz invariance. Apart from vector and axial-vector weak interaction components observed in nature it also contains scalar, tensor and pseudoscalar terms. The latter does not contribute to experimental observables in nuclear β -decay or neutron decay at the present level of precision as the pseudoscalar hadronic current vanishes in the non-relativistic treatment of nucleons. Scalar and tensor terms are components that can in principle occur. However, experimental limits from nuclear β decay and neutron decay restrict their potential contribution to 7% and 8%, respectively (95.5% C.L.) [2]. Many recent experimental efforts try to improve the sensitivity to these non-standard model weak currents in searches for differences of experimental observables from their standard model predictions in both neutron decay [3–6] and nuclear β decay [2, 7–14].

Measurements of the angular distribution of β particles emitted in the decay of polarized nuclei are potentially very sensitive to deviations from the Standard-Model [11, 12]. The angular distribution is given by [15]:

$$W(\theta) \propto \left[1 + b \frac{m}{E_e} + \frac{\mathbf{p}_e}{E_e} \cdot A\mathbf{J} \right], \quad (1)$$

with E_e and \mathbf{p}_e the total energy and momentum of the β particle, m the rest mass of the electron, \mathbf{J} the nuclear vector polarization and b the Fierz interference term. The actual quantity that is determined experimentally is not A but

$$\tilde{A} = \frac{A}{1 + \langle b' \rangle} \quad (2)$$

with $b' \equiv (m/E_e)b$ and where $\langle \rangle$ stands for the weighted average over the observed part of the β spectrum.

For an allowed pure Gamow-Teller β transition this can be written as (assuming maximum parity violation and time-reversal invariance for the axial-vector part of the interaction) [15]:

$$\begin{aligned} \tilde{A}_{GT}^{\beta\mp} &\simeq A_{SM} \left[1 - \frac{\alpha Z m}{p_e} \Im \left(\frac{C_T + C'_T}{C_A} \right) \right. \\ &\quad \mp \frac{\gamma m}{E_e} \Re \left(\frac{C_T + C'_T}{C_A} \right) \\ &\quad \left. \mp \Re \left(\frac{C_T C'_T}{C_A^2} \right) - \frac{|C_T|^2 + |C'_T|^2}{2C_A^2} \right] \\ &\simeq A_{SM} \left[1 \mp \frac{\gamma m}{E_e} \Re \left(\frac{C_T + C'_T}{C_A} \right) \right], \end{aligned} \quad (3)$$

with C_T , C'_T and C_A coupling constants of the tensor and axial-vector parts of the weak interaction and with primed (unprimed) coupling constants for the parity conserving (violating) parts of the interactions, respectively. Further, the upper (lower) sign refers to β^- (β^+) decay, and $\gamma = [1 - (\alpha Z)^2]^{1/2}$ with α the fine structure constant and Z the atomic number of the daughter isotope. The Standard Model value of the asymmetry parameter for pure GT transitions is $A_{SM} = -1$ for $J \rightarrow J - 1$ transitions, $A_{SM} = -1/(J + 1)$ for $J \rightarrow J$ and $A_{SM} = J/(J + 1)$ for $J \rightarrow J + 1$.

For the approximation in the last line of Eq. (3) the imaginary term, $\Im(C_T + C'_T)/C_A$, was neglected as existing limits for it are already at the 1% level [16], and the couplings C_T/C_A and C'_T/C_A are known to be sufficiently small [2] in order that second-order terms such as $|C_T|^2/|C_A|^2$ can be neglected compared to first-order terms. Any departure in the measured value \tilde{A} from the Standard-Model value A_{SM} is then sensitive to the tensor couplings ($C_T + C'_T$). Further, with the factor γ being of order unity, the sensitivity to these tensor couplings is enhanced for low endpoint energy β decays.

As precisions of the order of 1% or better are obtained for the β -asymmetry parameter \tilde{A} , higher order corrections to the value predicted by the Standard Model become potentially significant (e.g. Ref. [12]). Both recoil corrections, induced by the strong interactions between the quarks, and radiative corrections are discussed in Sec. VII.

The sensitivity of the low temperature nuclear orientation method (LTNO) [17] for this type of measurements has been shown recently in experiments with ^{60}Co [12] and ^{114}In [11] which constitute the most precise measurements of this type in nuclear β decay to date. Here we present the results of an experiment using the same method for the pure Gamow-Teller β^- decay of ^{67}Cu . The isotope ^{68}Cu , with a much higher β -endpoint energy and therefore much smaller sensitivity to tensor weak currents, was used for normalization purposes.

II. EXPERIMENTAL METHOD

A. The isotopes ^{67}Cu and ^{68}Cu

The isotope ^{67}Cu has a spin-parity $I^\pi = 3/2^-$ and a magnetic moment $\mu = +2.5142(6)\mu_N$ [18], with a half-life of 61.83(12) h and a β -endpoint energy of 561.7 keV ($\log ft = 6.3$) [19]. It decays via a pure Gamow-Teller transition to the ground state of ^{67}Zn . A simplified decay

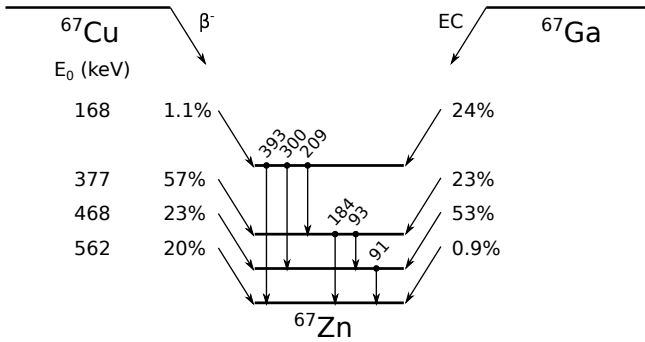


Figure 1. Simplified decay scheme of ^{67}Cu and ^{67}Ga . For ^{67}Cu the β intensities and endpoint energies (E_0) are shown, while for ^{67}Ga the EC transition intensities are indicated. The accompanying γ rays in ^{67}Zn are also shown.

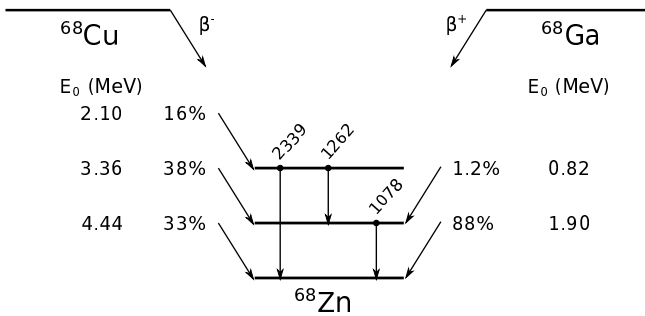


Figure 2. Simplified decay scheme of ^{68}Cu and ^{68}Ga with β branch intensities, β endpoint energies (E_0) and accompanying γ rays being shown. For clarity, two branches in the decay of ^{68}Cu (with total intensity of 5%) decaying to levels in ^{68}Zn between the two higher lying ones, as well as other, low endpoint branches are not shown.

scheme is shown in Figure 1.

The isotope ^{68}Cu has a spin-parity $I^\pi = 1^+$ and a magnetic moment $\mu = 2.3933(6)\mu_N$ [18], with a half-life of 31.1(15) s and a β -endpoint energy of 4.440 MeV [20]. It decays via a pure Gamow-Teller transition to the ground state of ^{68}Zn . A simplified decay scheme is shown in Figure 2.

B. Sample preparation

Both isotopes were produced at ISOLDE (CERN) with a 1.4 GeV proton beam from the Proton Synchrotron Booster, bombarding a ZrO_2 felt target (6.3 g Zr/cm^2) [21] connected to the RILIS [22, 23] which provided the required element selectivity. After ionization and acceleration to 60 keV, the ion beams were mass-separated by the General Purpose Separator, transported through the beam distribution system, and implanted into a polished and annealed 99.99% pure Fe foil (size $13.1 \text{ mm} \times 15.5 \text{ mm}$, original thickness $250 \mu\text{m}$) soldered onto the cold finger of the NICOLE $^3\text{He-}^4\text{He}$ dilution refrigerator [24, 25]. This foil had been polished with diamond-base paste with grain sizes of $3 \mu\text{m}$ and $1 \mu\text{m}$. It is estimated that this procedure reduced the thickness of the foil to $90 \pm 20 \mu\text{m}$. The average implantation depth of $^{67,68}\text{Cu}$ ions with an energy of 60 keV in this foil was calculated to be about 20 nm. The corresponding energy loss for β particles leaving the foil is only of the order of 100 eV, which is negligible in comparison to the β -endpoint energies of these isotopes. Prior to the measurements the foil was magnetized to saturation in a 0.5 T horizontal external magnetic field generated by a superconducting split-coil magnet. During the measurements this field was reduced to $B_{\text{app}} = 0.100(2) \text{ T}$ so as to minimize its influence on the trajectories of the β particles.

C. Detection setup

The angular distribution of the electrons emitted during the β^- decay of ^{67}Cu and ^{68}Cu was observed with two planar high purity Ge (HPGe) particle detectors with a sensitive diameter of 16 mm and a thickness of 4 mm produced in the Nuclear Physics Institute in Řež, Prague [26–28]. They were selected to fully stop the high-endpoint energy β electrons from ^{68}Cu and installed at a distance of 37.7 mm from the sample, inside the 4 K radiation shield of the refrigerator. The fact that they were looking directly at the radioactive source assured good counting rates and at the same time avoided effects of scattering or absorption (energy loss) of the β electrons in the radiation shields. The actual operating temperature of the detectors was about 10 K. In order to minimize effects of scattering in the Fe foil they were mounted to view the foil surface (which was parallel to the magnetic field) under an angle of about 15° , corresponding to detection angles of 15° (Right detector) and 165° (Left

detector) with respect to the polarizing magnetic field. Thin isolated copper wires (about 13 cm long) connected the detectors to the preamplifiers outside the refrigerator, resulting in an energy resolution of about 3 keV for 1 MeV electrons. Thin wires were used in order to minimize the heat load from room temperature to the detectors.

Apart from these particle detectors, large-volume HPGe detectors for detection of the γ radiation were installed outside the refrigerator at 0° and 180° with respect to the orientation axis (magnetic field axis). The energy resolution of these was about 3 keV for the 1332 keV γ line of ^{60}Co .

All data were corrected for the dead time of the data acquisition system using a precision pulse generator. The energy calibration of all detectors was performed with the 136.5 and 692.4 keV γ lines of ^{57}Co and the 184.6 keV γ line of ^{67}Cu . During the on-line measurement of ^{68}Cu additional calibration was performed with the 1077.7 keV γ line of ^{68}Cu and the 511 keV positron annihilation line from the β^+ decay of ^{68}Ga .

D. Angular distributions

The angular distribution of radiation emitted by oriented nuclei can be described by the function [29]

$$W(\theta) = 1 + f \sum_{\lambda} B_{\lambda} U_{\lambda} A_{\lambda} Q_{\lambda} P_{\lambda}(\cos \theta). \quad (4)$$

Here f represents the fraction of nuclei that experience the full orienting hyperfine interaction μB (with μ the nuclear magnetic moment and B the total magnetic field), while the rest $(1 - f)$ is supposed to experience no interaction at all. B_{λ} are the nuclear orientation parameters which depend on the magnetic moment μ of the decaying nuclei, the total magnetic field B_{tot} these nuclei experience (see Sec. II E), the temperature of the sample T , and the initial spin I , the half-life and the relaxation constant C_K of the oriented state. The U_{λ} are the deorientation coefficients, which account for the effect of unobserved intermediate radiations, while A_{λ} are the directional distribution coefficients which depend on the properties of the observed radiation itself. Finally, Q_{λ} are solid angle correction factors and $P_{\lambda}(\cos \theta)$ are the Legendre polynomials. The angle θ is measured with respect to the orientation axis.

For γ rays only λ even terms occur. For allowed β decays only the $\lambda = 1$ term is present

and Eq.(4) transforms to

$$W(\theta) = 1 + f \frac{v}{c} \tilde{A} P Q_1 \cos \theta, \quad (5)$$

where v/c is the β particle velocity relative to the speed of light, \tilde{A} is as defined in Eq. 3 and P is the degree of nuclear polarization. Note that the product $\frac{v}{c} \tilde{A} P$ is equal to $B_1 A_1$ in the notation used in [29].

Experimentally the angular distribution is obtained as

$$W(\theta) = \frac{N_{\text{cold}}(\theta)}{N_{\text{warm}}(\theta)}, \quad (6)$$

with $N_{\text{cold,warm}}(\theta)$ the count rates when the sample is ‘‘cold’’ (about 10 mK; oriented nuclei) or ‘‘warm’’ (about 1K; unoriented nuclei). Such a ratio is then constructed for each detector.

In on-line experiments, where the count rates vary with beam intensity, it is customary to construct a double ratio, combining count rates in two different detectors in order to eliminate effects of beam intensity fluctuations and avoid the need to correct for the half-life of the isotope. In the present work the double ratio

$$R = \frac{W(15^\circ)}{W(165^\circ)} = \frac{\left[\frac{N(15^\circ)}{N(165^\circ)} \right]_{\text{cold}}}{\left[\frac{N(15^\circ)}{N(165^\circ)} \right]_{\text{warm}}} \quad (7)$$

was used for the β electrons of ^{68}Cu .

For the β -asymmetry measurement of ^{67}Cu , and for the gamma detectors used for temperature determination by observing the anisotropy of the 136 keV γ rays of the isotope ^{57}Co , no double ratios were necessary as these isotopes were not produced on-line and the half-lives are known with sufficient precision so that these could be taken into account in the data analysis.

E. Total magnetic field

In LTNO experiments the total magnetic field the nuclei feel when implanted into a ferromagnetic host foil has three components:

$$B_{\text{tot}} = B_{\text{hf}} + B_{\text{app}}(1 + K) - B_{\text{dem}}. \quad (8)$$

with B_{hf} the hyperfine magnetic field, B_{app} the externally applied magnetic field, B_{dem} the demagnetization field, and K the Knight shift. The external field was in all measurements

set to 0.100(2) T. The hyperfine field of dilute Cu impurities in Fe was recently determined to be -21.794(10) T [30]. The demagnetization field for the foil is 0.018(4) T [31], with a 20% error to account for the approximations made when arriving to the analytical formulas of the demagnetization field. The Knight shift for copper in iron has never been determined at low temperatures, but a conservative upper limit of 5% corresponds to a 0.005 T systematic uncertainty on the total magnetic field [30]. The total field the nuclei experience then amounts to $B_{\text{tot}} = -21.712(12)$ T.

F. Thermometry

The temperature of the sample was maintained in the region between 8 mK and about 60 mK and measured by monitoring the intensity of the 136 keV γ line of a $^{57}\text{CoFe}$ nuclear orientation thermometer [32], attached to the back side of the sample holder, using two HPGe detectors. The ^{57}Co activity had been diffused into an iron foil similar to the sample foil and prepared in the same way. Calibration of the thermometer against a ^{60}Co single crystal thermometer resulted in a fraction of 94.3(4)% of the ^{57}Co nuclei feeling the full orienting hyperfine field in the foil.

G. Nuclear spin-lattice relaxation

Due to their short half-life the ^{68}Cu nuclei had to be implanted continuously and their anisotropies be observed in on-line conditions. As a consequence the value for the nuclear polarization $P = \sqrt{3I/(I+1)}B_1$ results from an equilibrium between implantation of un-oriented (warm) nuclei and the decay of (partially) relaxed nuclei that may or may not yet have reached thermal equilibrium (i.e. the full orientation corresponding to the sample temperature). This nuclear spin-lattice relaxation effect needs to be taken into account when the half-life and the relaxation time are of the same order of magnitude. For the case of a dominant magnetic-dipole relaxation mechanism, as applies to 3d element impurities in an Fe host [33], the so-called Korringa constant, C_K , describes the relaxation process. When C_K is known for one isotope of a given element in a specific host material it can be calculated for the other isotopes using the relation [34]:

$$\frac{\mu^2 C_K}{I^2} = \text{const} . \quad (9)$$

Table I. Calculated values of C_K for all Cu isotopes studied here, using Eq. 9 and the C_K value measured previously for ^{62}Cu . The uncertainties are dominated by the uncertainty of the measured C_K value for ^{62}Cu . All magnetic moment values are from Ref. [18].

	^{62}Cu	^{67}Cu	^{68}Cu	$^{68\text{m}}\text{Cu}$
μ [μN]	0.3809(12)	2.5142(6)	2.3933(6)	1.1548(6)
I (\hbar)	1	3/2	1	6
T_{int} [mK] ^a	3.0	13	19	1.5
C_K [sK]	4.34(25) ^b	0.225(13)	0.110(6)	17.0(10)

^a using the hyperfine field for Cu in Fe host from [30]

^b from Ref. [35]

The C_K has been measured in the past for two other Cu isotopes, ^{62}Cu [35] and ^{63}Cu [36], in iron and at $B_{\text{ext}} = 0.1$ T. The former measurement used the technique of LTNO at milliKelvin temperatures while the latter was a spin-echo experiment at 4.2 K. To estimate the C_K of the isotopes of interest in this work we will use here the result of the ^{62}Cu measurement since the experimental conditions were very similar to ours. Spins, magnetic moments and measured or calculated C_K values for the different Cu isotopes studied here are listed in Tab. I.

In conventional nuclear magnetic resonance (NMR) at lattice temperatures $T \geq 1$ K, spin-lattice relaxation leads to an exponential time dependence of the signal and a relaxation time T_1 can be defined unambiguously. Such experiments are always performed in the high-temperature limit, i.e. $T \gg IT_{\text{int}}$ with the interaction temperature T_{int} given by the nuclear level splitting:

$$T_{\text{int}} = |\mu B_{\text{tot}}/k_{\text{B}}I| \quad (10)$$

(with k_{B} the Boltzmann constant), such that for metallic samples the Korringa law, i.e. $C_K = T_1 T$, is valid.

The relaxation behavior we probe via the B_1 orientation parameter in the β decay of the copper isotopes studied here is the same as in conventional NMR. However, since $T_{\text{int}}(^{68}\text{CuFe}) = 19$ mK and our data were taken at temperatures between about 18 mK and 8 mK, the low temperature limit, $T \leq IT_{\text{int}}$, applies. Experimentally it was observed [37] that the angular distribution in this case, to first order, still has a single exponential behavior that

can be characterized by a constant “relaxation” time, T_μ . This T_μ provides a good estimate of the time required to reach thermal equilibrium and is given by $T_\mu = C_K/IT_{int}$. The parameter C_K is then called “relaxation constant” to not give erroneously the impression that the Korringa law has been assumed in data analysis.

In the low temperature limit one calculates $T_\mu \simeq 6$ s for $^{68}\text{CuFe}$ which is of the same order of magnitude as the half-life of 31 s, so that relaxation effects (modifying the B_1 parameter) have to be taken into account in fitting the β anisotropy for ^{68}Cu (see Sec. V A).

For $^{67}\text{CuFe}$, the factor $IT_{int} = 20$ mK corresponds to $T_\mu \simeq 11$ s. However, as ^{67}Cu was collected off-line and measured only later, relaxation phenomena were only an issue when the sample temperature was changed during the measurement. As data were collected throughout the experiment in blocs of 300 s each, neglecting the first 300 s bloc after a change in sample temperature assured that relaxation effects did not play a role in the analysis of the data for ^{67}Cu .

III. DATA TAKING

A. β spectrum of ^{67}Cu and beam purity

The observed β spectrum of ^{67}Cu is shown in Fig. 3. The peak at the end of the spectrum is from the pulser that was used to monitor the dead time of the data acquisition system. Because of the rather long half-life of ^{67}Cu the measurement of this isotope was performed in semi-online mode, meaning that a ^{67}Cu sample was collected for several hours after which the beam line was closed and the measurement started. To extract the asymmetry parameter for the highest-energetic pure Gamow-Teller $3/2^- \rightarrow 5/2^-$ β transition of ^{67}Cu only the upper part of the spectrum between 469 keV and 562 keV was considered. This region does not contain events from other β branches with lower endpoint energy. The region between 410 and 469 keV, containing also counts from the next β branch, was analyzed as well, providing a cross-check on the value of \tilde{A} , although with a lesser precision (see Sec. VI B 8).

The very weak γ peak at 692.4 keV is from the decay of the ^{57}Co nuclear thermometer and does not disturb the β -asymmetry measurement. A possible contamination from ^{67}Ga in the beam was not important since ^{67}Ga decays purely by electron-capture and has no intense γ rays in its decay that could contaminate the β spectrum in the region of interest

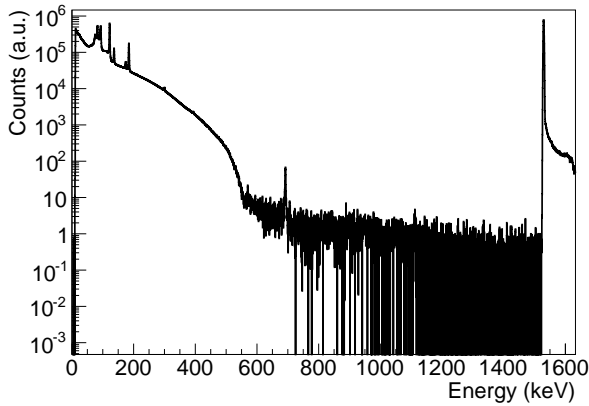


Figure 3. The β spectrum of ^{67}Cu as observed by the Right particle detector. The very weak γ line at 692.4 keV is from the ^{57}Co thermometer, while the large peak at around 1500 keV is the pulser peak.

(see Figure 1).

B. β spectrum of ^{68}Cu and beam purity

The β spectrum of ^{68}Cu is shown in figure 4. Due to the short half-life a full on-line measurement was necessary for this isotope. In this case ions are continuously implanted into the sample foil while performing the measurement. The anisotropy of the highest-energetic β branch of ^{68}Cu was used to obtain the fraction f of Cu nuclei experiencing the full orienting magnetic field via Eq. 5. As both ^{67}Cu and ^{68}Cu were implanted at low dose (i.e. well below 5×10^{13} at/cm²) and at low temperature in the same iron foil, and their anisotropies were also observed in this same foil, the fraction obtained for ^{68}Cu can be used for the measurement with ^{67}Cu as well. As the second most energetic β branch of ^{68}Cu has an endpoint energy as much as 1078 keV lower than the highest energetic one the region of interest for analysis could be restricted to the upper β branch (i.e. from 3.39 to 4.44 MeV) without problems with respect to collecting enough statistics. Further, due to the high endpoint energy of 4.44 MeV the region of interest is completely free from events coming

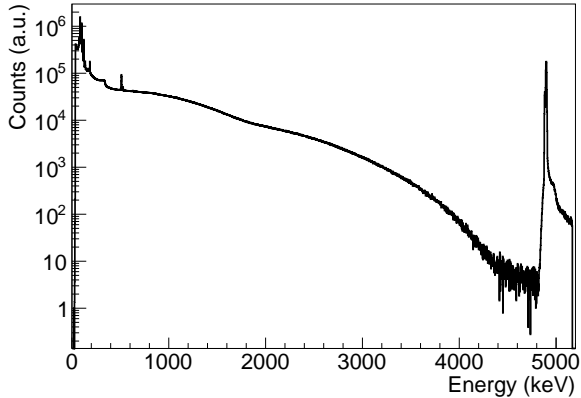


Figure 4. The β spectrum of ^{68}Cu as observed by the Right particle detector. The 511 keV annihilation peak is from the β^+ decay of ^{68}Ga . Near the high-energy end of the spectrum the pulser peak is visible.

from the other isotopes. Finally, due to the much higher β endpoint energy of ^{68}Cu with respect to ^{67}Cu , the sensitivity of the β asymmetry measurement with ^{68}Cu to tensor type contributions was about five times less (see Eq. 3) so that the fraction f could be obtained and then be used later for the analysis of the β asymmetry of ^{67}Cu , without disturbance by possible tensor currents (see also Sec. V A).

The amount of ^{68}Ga contamination was roughly estimated from β spectra when no ^{68}Cu was present in the system, i.e. after the beam was stopped. The amount of ^{68}Ga in the beam was found to be similar to that of ^{68}Cu . However, due to its low β -endpoint energy of 1.9 MeV it did not disturb the measurement on the highest energy β branch of ^{68}Cu .

The amount of the metastable $^{68\text{m}}\text{Cu}$ in the beam was estimated from the intensity of the 526 keV gamma line and found to be around 10%. As this isotope has a half-life of 3.75 min and a magnetic moment of $1.1548(6) \mu_N$ [18] it also becomes oriented. However, $^{68\text{m}}\text{Cu}$ decays mainly (branching ratio of 84%) via an internal transition to the ground state, the effect of which is discussed in Section V B. The remaining 16% decay via β^- emission but these are feeding the higher lying states in ^{68}Zn so that the β -endpoint energy is only 2.8 MeV. These β particles therefore do not disturb the region of interest (i.e. from 3.39 to

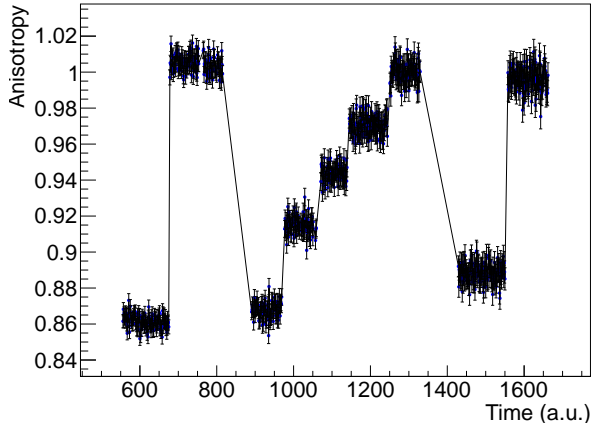


Figure 5. Count rate of the 136 keV γ line of the ^{57}Co thermometer normalized to isotropic (“warm”) data during the ^{67}Cu measurement, showing the 6 “cold” and 3 “warm” data blocs. Every data point represents a measurement time of 300 s.

4.44 MeV) that is used for the determination of the fraction f of ^{68}Cu at good lattice sites.

C. Data taking sequence

The experimental campaign started with a temperature test followed by the online measurement of ^{68}Cu , which consisted of one cooling cycle with four different temperature points. After that the ^{67}Cu sample was collected. The off-line measurement of this isotope included two cooling cycles with a total of six temperature points and three measurement periods with isotropic emission (unoriented nuclei). Figure 5 shows the count rate of the 136 keV γ line of the ^{57}Co thermometer normalized to isotropic (“warm”) data during these measurements with ^{67}Cu .

D. Further steps

The temperature for each 300 s measurement was determined from the anisotropy of the 136 keV γ ray of the ^{57}Co nuclear thermometer. After identifying time intervals of constant

temperature the experimental spectra were summed. The dead time was deduced from the intensity of the pulser peak and its tail, while the pile-up probability (see Sec. VIB 4) was obtained from the pulser tail-to-peak ratio. The integrals of the summed experimental spectra in the different energy ranges (providing N_{cold} for different temperatures and N_{warm}) were corrected for dead time and measurement time, as well as for the decay of ^{67}Cu during the measurement.

IV. SIMULATIONS

In the analysis extensive use was made of the Geant4-based Monte Carlo code [38] that was developed for this type of experiments [39] and which was modified for the geometry of the NICOLE low temperature nuclear orientation setup. A detailed description of the setup as well as of the magnetic field generated by the split-coil superconducting magnet around the sample, was implemented in the code. The field map was provided by the magnet manufacturer, Oxford Instruments.

As in previous works [11, 12] the main role of the code was to account for the effects of electron (back)scattering in the sample foil, on the detectors and the environment, as well as to deal with the influence of the external magnetic field on the electron trajectories. It thus provides a value for $\tilde{Q} = \frac{v}{c}Q_1 \cos \theta$ for each temperature point.

Geant4 has built-in modules to handle the decay of radioactive isotopes which include the full decay scheme. However, our code for simulating β anisotropies has to be used outside this framework; for both isotopes only the three most intense β branches together with their accompanying γ rays (see Tab. II) were included in the simulations. The other β branches did not affect the respective regions of interest and were therefore omitted. The asymmetries of the γ rays were not simulated because they also do not affect the region of interest in the spectrum. The lowest energetic of the three β branches included for ^{67}Cu has an unknown \tilde{A} coefficient (the Fermi/Gamow-Teller mixing ratio is not known) and was therefore simulated isotropically.

Detailed models of the HPGe particle detectors were implemented and verified by test measurements [28, 40]. The reliability of the simulations was further verified by simulating the isotropic data of both ^{67}Cu and ^{68}Cu . For the former, we find agreement between experiment and simulations to better than 3-4% over the energy region between 300 keV

Table II. The simulated β branches for ^{67}Cu [19] and ^{68}Cu [20]. Endpoint energies (E_0), relative intensities (Int.) and the \tilde{A} parameters are shown. The uncertainties on the β branch intensities of ^{67}Cu are based on the corresponding γ intensities.

^{68}Cu			^{67}Cu		
E_0 (MeV)	Int (%)	\tilde{A}	E_0 (keV)	Int (%)	\tilde{A}
4.44	33(4)	-1	561.7	20.0(3)	0.6
3.36	38(4)	0.5	468.4	21.8(3)	-1
2.10	16.0(1.2)	0.5	377.1	57.1(3)	0.0 ^a

^a unknown F/GT mixing ratio, no anisotropy simulated

and the endpoint (Fig. 6), and a $\chi_{red}^2 = 1.24$ for 91 degrees of freedom for the region of interest, i.e. between 470 and 560 keV. For ^{68}Cu the agreement between experiment and simulations is somewhat worse but still better than about 5% everywhere from 2.00 MeV up to about 200 keV from the endpoint where pile-up events start to dominate

Simulations for the anisotropic (“cold”) data were performed for each temperature point, with the corresponding degree of nuclear polarization and the standard model value for the β -asymmetry parameter as input values. For ^{68}Cu the relaxation was also taken into account. From the raw data histograms were constructed which took into account the experimentally determined dead time and detector pulse pile-up. The effect of the fraction of nuclei at good lattice sites was also incorporated at this stage. Spectra of ^{57}Co were also simulated and added to the histograms of ^{67}Cu .

V. ^{68}Cu ANALYSIS

A. Fraction determination

Analysis revealed a significant amount of events close to and beyond the β endpoint as a result of detector event pile-up due to the high count rate during the ^{68}Cu measurement. The fact that this reduced significantly the signal-to-noise ratio near the β endpoint lead us to reduce the region of interest (ROI) for analysis to 3400-4000 keV. For this energy region comparison of experimental and simulated isotropic (“warm”) spectra revealed a $\chi_{red}^2 = 0.97$

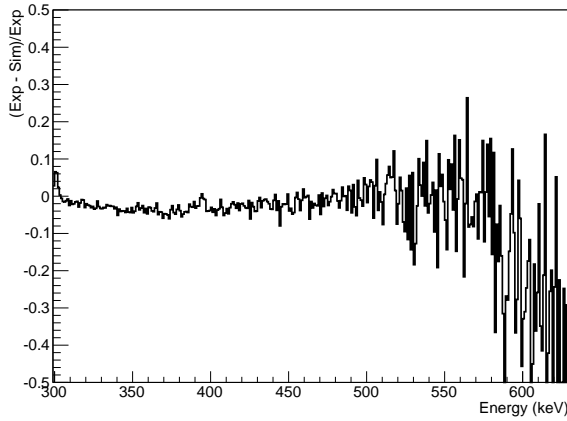


Figure 6. Difference between the experimental and simulated spectrum of isotropic ^{67}Cu (Left detector), normalized to the experimental spectrum. The region of interest is between 470 and 560 keV, where $\chi_{red}^2 = 1.24$ for 91 degrees of freedom.

for 251 degrees of freedom.

The ROI was divided into 6 energy bins, each 100 keV wide. Experimental double ratios R (see Eq. 7) were determined for these energy bins for each temperature point:

$$R = \frac{W(15^\circ)}{W(165^\circ)} = \frac{1 + f\tilde{A}B_1(T, C_K)\tilde{Q}(15^\circ)}{1 + f\tilde{A}B_1(T, C_K)\tilde{Q}(165^\circ)}, \quad (11)$$

(see Fig. 7).

It was demonstrated earlier (with ^{62}Cu) [35] that the simultaneous fit of the fraction f and the relaxation constant C_K to the anisotropy curve is possible. The parameter f , being independent of temperature, determines only the size of the anisotropy effect $|R - 1|$, while B_1 is temperature dependent and therefore determines the shape of the anisotropy R versus temperature. The calculation of B_1 takes into account the fact that upon implantation the nuclei are not oriented. In the time following they relax to thermal equilibrium with the cold lattice where the size of B_1 is determined by a competition between nuclear decay and relaxation. In order to take into account the effect of spin-lattice relaxation (i.e. C_K) in Eq. 11 the nuclear orientation parameter B_1 was expressed as $B_1(\text{sec}) = \rho_1 B_1(\text{th})$, with ρ_1 the ratio of the observed orientation parameter for the nuclear ensemble when in secular

equilibrium (i.e. still relaxing) and $B_1(\text{th})$ the thermal equilibrium orientation parameter. The ρ_1 attenuation coefficients were determined according to the procedure outlined in Ref. [41] (see also Ref. [34]) and taking into account the observed temperature for each individual data point.

In fitting the experimental data we used $\mu(^{68}\text{Cu}) = 2.3933(6) \mu_{\text{N}}$ (Tab. I) and $B_{\text{hf}}(\text{CuFe}) = -21.712(12) \text{ T}$ (see Sec. II E). The \tilde{Q} factor was obtained for each bin and for each temperature point using Geant4 simulations, its value ranging from 0.86 to 0.95. The Standard Model value of the β -asymmetry parameter of ^{68}Cu , based on the spin sequence only, is $A_{SM} = 1$. However, higher order corrections (see Sec. VII for details) modify this value to 0.9902(22), determined at 3700 keV. The energy dependence of these corrections (a 0.15% change over the entire energy range) was also incorporated in the fit procedure.

Two parameter fits for f and C_K to the double ratio R were performed for all 6 energy bins in the region between 3400 and 4000 keV. The weighted average of the results obtained for the Korringa relaxation constant yielded $C_K = 0.124(29) \text{ sK}$. However, as the two fit parameters are correlated, their respective uncertainties are significantly larger than expected based on statistics. As this value obtained for C_K is in perfect agreement with the value of 0.110(6) sK calculated for ^{68}Cu on the basis of the value previously measured for ^{62}Cu in Fe host (see Tab. I), C_K was subsequently fixed to 0.110(6) sK and only the fraction f fitted.

The values of the fraction f thus obtained for each of the 100 keV wide energy bins are shown on Fig. 8, with their statistical error bars increased by a factor of $\sqrt{\chi_{\text{red}}^2}$, obtained from the fit. The final value for the fraction was determined as the weighted average in the energy region from 3400 to 4000 keV, yielding $f = 1.0003(26)$, where the error is purely statistical. The systematic errors are summarized in Tab. III and discussed further in the next section. Combining then the systematic and statistical uncertainties one arrives at $f = 1.0003(26)_{\text{stat}}(80)_{\text{syst}}$.

B. Error analysis

1. Relaxation

The approximately 5% relative uncertainty related to the calculated value $C_K = 0.110(6)$ used in the fitting the ^{68}Cu data induces a 0.0072 systematic error on the fraction.

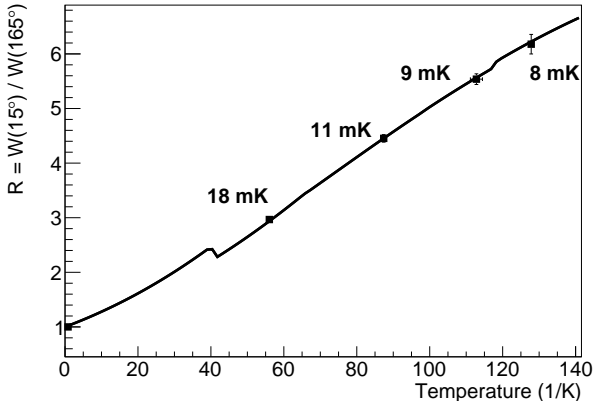


Figure 7. Fit of the fraction f to the double ratio R (Eq. 7) determined at different temperatures, for the energy range of 3600-3700 keV. The fit resulted in $f = 1.002(4)$ with $\chi_{red}^2 = 1.1$ for 4 degrees of freedom. The fit function is not continuous because of the different values of \tilde{Q} at different temperature points.

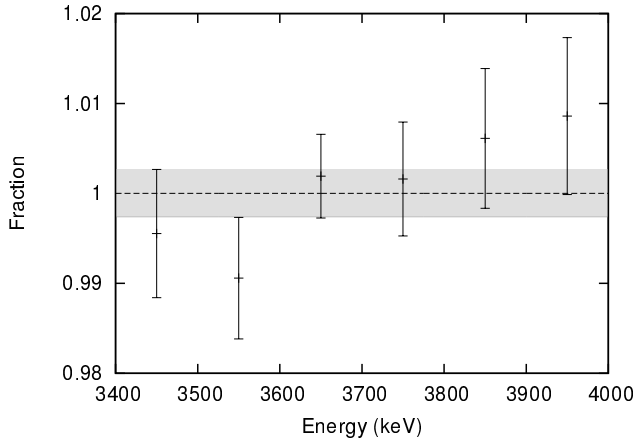


Figure 8. Results of the fit of the fraction f to the experimental double ratio R in the different energy regions. The weighted average for the total region from 3400 to 4000 keV is $1.0003(26)$, which is indicated by the dashed line and the gray band.

Table III. Contributions to the systematic uncertainty of the fraction determination from the decay of ^{68}Cu . The recoil corrections are discussed in Sec. VII

Effect	Value
relaxation constant C_K	0.0072
effective detector thickness	–
$^{68\text{m}}\text{Cu}$ isomeric state	–
thermometry	0.0028
μB of ^{68}Cu	0.0003
tensor couplings	0.0018
Geant4	–
recoil corrections	0.0012
Total:	0.0080

2. *Effective detector thickness*

The thickness of the sensitive area of the planar HPGe β detectors is determined by the thickness of the rear dead layer which was measured to be between 0.7 and 0.9 mm [26]. Simulations were performed to check whether this influences the value of the fraction. No effect outside the statistical error bar (0.003) of these simulations was found. Note that this effect is only relevant when dealing with high energy electrons. Consequently the ^{67}Cu results, where the β particles were stopped in the upper part of the sensitive area of the detector, are not affected.

3. *Orientation of the $^{68\text{m}}\text{Cu}$ isomeric state*

As mentioned before the 721 keV isomer of ^{68}Cu was also present in the beam with an estimated 10% relative intensity. Its relatively long half-life of 3.75 min and magnetic moment of $1.1548(6) \mu_N$ [18] ensures that these nuclei also become oriented. Since $^{68\text{m}}\text{Cu}$ decays with a 74% branching ratio via a γ cascade to the ground state, this alters the isotropic orientation of ^{68}Cu expected from implantation. However, due to the small interaction temperature

$T_{\text{int}} = 1.5$ mK of $^{68\text{m}}\text{Cu}$, the associated B_1 parameters remain below 0.1 even for the base temperature of 8 mK, because of the high relaxation constant for $^{68\text{m}}\text{Cu}$ ($C_K = 17.0(10)$ sK, see Tab. I). The induced orientation of the ground state of ^{68}Cu is further reduced by the deorientation coefficient, which takes into account the γ cascade connecting the two states. Since the M1/E2 mixing ratios of these γ transitions are not known we use a worst case scenario, i.e. take the mixing such as to produce the largest possible values. In that case the deorientation coefficient is $U_1 = 0.0053$, which, in combination with the calculated B_1 value yields an induced β anisotropy for ^{68}Cu below 0.04%, which is negligible at the present level of precision.

4. Thermometry

The statistical errors related to the temperature determination were included in the fit (horizontal error bars on Fig. 7). The systematic effects are discussed in Sec. VIB2, and these induce a 0.0028 systematic error on the fraction.

5. Hyperfine interaction μB

The error on the hyperfine interaction experienced by the ^{68}Cu nuclei has two components. One is from the nuclear magnetic moment μ , the other from the hyperfine field of Cu impurities in iron host. The relative error on the latter is larger and therefore dominates the total of the 0.0003 systematic error from μB on the fraction.

6. Tensor couplings

The β -asymmetry parameter \tilde{A} of ^{68}Cu is also sensitive to the tensor coupling constants C_T and C'_T . However, the sensitivity factor $\gamma m/E_e = 0.1157$ is almost a factor 5 smaller than for ^{67}Cu . Considering the current 2σ limits on tensor couplings, i.e. $-0.008 < (C_T + C'_T)/C_A < 0.024$ [2], translates into an 0.0018 uncertainty on the β -asymmetry parameter of ^{68}Cu and, consequently, on the fraction f .

7. *Geant4*

The statistical uncertainties of the *Geant4* simulations were added in quadrature to the uncertainties of the measured asymmetry data.

8. *Other effects*

The double ratio R contains the factor $[N(15^\circ)/N(165^\circ)]_{\text{warm}}$ in the denominator, which ensures that the majority of all temperature independent systematic effects are greatly reduced, or even canceled. Among these are geometrical uncertainties, such as the detector positions, together with the uncertainty related to the position of the implanted ^{68}Cu nuclei in the Fe foil (see Sec. VI B 1). Other remaining undetected systematic effects were accounted for by increasing the error bars on the fit results for the fraction by the factor of $\sqrt{\chi_{\text{red}}^2}$.

VI. ^{67}Cu ANALYSIS

A. Extraction of the beta-asymmetry parameter

In order to check for possible energy-dependent systematic effects in the β spectrum of ^{67}Cu the region of interest (ROI) was divided into several energy bins. Analysis showed that, similar to the case of ^{68}Cu , the ROI had to be reduced to 470-510 keV because of detector event pile-up. The lower edge of the ROI is limited by the presence of another β branch with endpoint energy of $E_0 = 469$ keV (see Fig. 1 and Tab. II). As a cross-check on the value of \tilde{A} obtained, also the region from 410 to 470 keV was included in the analysis. However, the precision obtained in this case is less good due to the presence of counts from two β branches.

Having obtained both experimental and simulated integrals ($N_{\text{cold,warm}}$) for all energy bins, the ratio

$$\frac{W^{\text{exp}} - 1}{W^{\text{sim}} - 1} = \frac{f B_1 \tilde{A} \tilde{Q}}{f B_1 A_{SM} \tilde{Q}} = \frac{\tilde{A}}{A_{SM}} \quad (12)$$

can be calculated, assuming that the *Geant4* simulations duly account for the geometrical factors \tilde{Q} . Further, the simulations relied on the value of the fraction f (obtained from the asymmetry of ^{68}Cu ; see Sec. V A) and of the orientation coefficients B_1 (corresponding to the sample temperature determined with the ^{57}Co nuclear thermometer; see Sec. II F). This

ratio is constructed for the different energy bins. When changing over from measuring ^{68}Cu to ^{67}Cu we unfortunately lost electrical contact to the Right β detector. The ^{67}Cu analysis therefore includes only data from the Left β detector.

An overview of the values obtained for \tilde{A}/A_{SM} as a function of energy in the region from 410 to 510 keV and for the different temperatures (viz. degrees of nuclear orientation), together with the weighted averages for the energy regions 470-510 keV (only the highest energetic β branch) and 410-470 keV (two highest energetic β branches) is given in Fig. 9. In the lower energy region events from the β branch of ^{67}Cu with endpoint energy of 468.4 keV are present as well, which renders the analysis of these data more complex. As can be seen, the weighted averages in both energy regions are always in good agreement, indicating the good quality of the Geant4 simulations of the β spectra over the entire energy region considered here. Indeed, many of the effects Geant4 has to take into account are energy dependent so that their improper treatment in the simulations would cause an energy dependence of \tilde{A}/A_{SM} . Also, no temperature or time dependence of \tilde{A}/A_{SM} was observed.

The weighted average of all points in the ROI is 0.9730(27) where the error is purely statistical. This still needs to be increased by a factor of $\sqrt{\chi_{\text{red}}^2} = 3.6$ (see Sec. VIB 3 for details), finally arriving to a value of 0.973(10). In the lower energy range (i.e. from 410 to 470 keV) the same procedure yields a value of 0.986(9). However, the systematic uncertainty related to the intensity of the second β branch relative to the highest energetic one (see Sec. VIB 8) amounts to 0.022, arriving at a value of 0.986(24).

B. Error analysis

The systematic errors associated with the ratio \tilde{A}/A_{SM} for ^{67}Cu are summarized in Tab. IV and discussed in the rest of this section.

1. Beam spot position

In this experiment the radioactive ions from ISOLDE were implanted into a cold sample foil which was soldered to the sample holder. However, it was noticed already in previous experiments that the resulting radioactive beam spot is not perfectly centered with respect

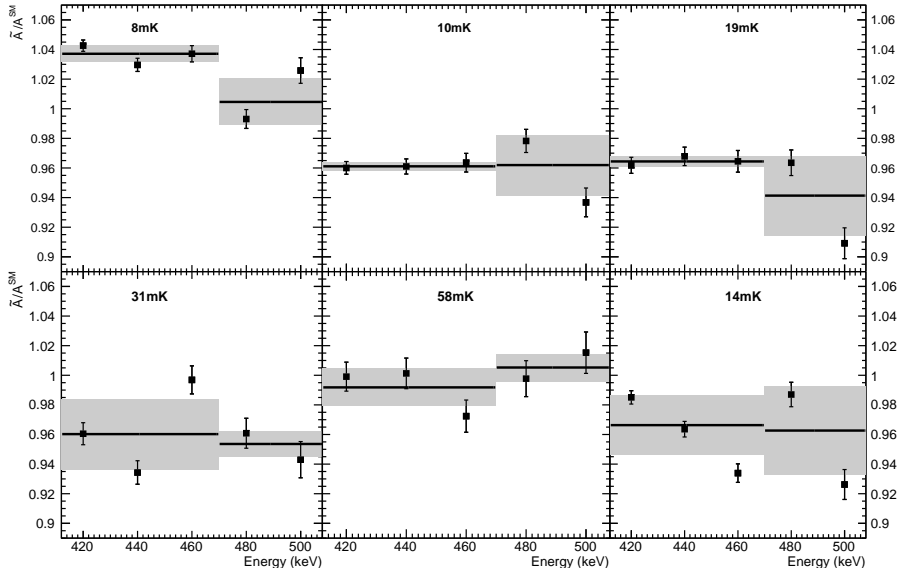


Figure 9. Ratio \tilde{A}/A_{SM} as a function of energy and for the different sample temperatures. Weighted averages are shown as horizontal lines (with the gray bands indicating the 1σ error bar) in the regions from 410 to 470 keV and from 470 to 510 keV. The energy region between 410 and 470 keV also contains events from the second most energetic β branch in the decay of ^{67}Cu (see Fig. 1 and Tab. II). No temperature or time dependent effects are observed (the data points are ordered chronologically).

to the sample holder. Consequently the Right and Left detectors have different count rates even when the nuclei are not oriented. To take this into account in the analysis the position of the implantation spot was measured with an adhesive tape mounted on the sample holder. The NICOLE setup was cooled to 77 K to achieve experimental conditions and a stable beam of ^{85}Rb was implanted for 5 hours with a beam current of approximately 8 nA. After the implantation a discolored spot was visible on the tape clearly indicating the position of the beam spot with respect to the sample holder. Two different methods of analysis yielded 0.85 mm and 1.1 mm offset toward the Right detector. To assess the effect of the beam spot position on the final result, all simulations were performed for both offset values and their average was then used. However, no systematic change outside of the statistical error bar

Table IV. Systematic error budget of the ratio \tilde{A}/A_{SM} measured in the decay of ^{67}Cu .

Effect	Value
beam spot position	–
thermometry ^a	0.0087
Geant4	–
pile-up	0.0028
half-life of ^{67}Cu	0.0068
geometry	0.0032
hyperfine interaction μB^b	0.0006
recoil corrections (Sec. VII)	0.0002
fraction from $^{68}\text{Cu}^c$	0.0080
Total:	0.0143

^a linear sum of the thermometry related uncertainties of both isotopes

^b linear sum of the uncertainties related to the hyperfine interaction of both isotopes

^c this contains the statistical error, but not the error related to thermometry

of 0.0027 was observed for this effect.

For the fraction f obtained from the ^{68}Cu data, the beam spot position does not cause a significant change. This is expected, since the usage of the double ratios R (Eq. 7) reduces any effect of this to a second order effect, which is in this case negligible. However, the analysis was still performed with simulated values of the \tilde{Q} factors for both beam offset values, with the average then being used as final result.

2. Thermometry

The distance between the nuclear thermometer and the HPGe γ detectors measuring the temperature was determined with 1 mm precision, which also includes the uncertainty of the position of the nuclear thermometer within the setup. This induces a 0.04 mK systematic error on all temperature points. Considering the thermometer, the fraction of the ^{57}Co nuclei feeling the orienting interaction, which was determined to be 0.943(4), induces a 0.07 mK error in the temperature determination. These errors are identical in the analysis of both

^{68}Cu and ^{67}Cu , and the final uncertainties were propagated accordingly.

In the analysis of the ^{67}Cu data the statistical error on the temperature was added in quadrature to the statistical error of the simulated asymmetry.

3. Quality of Geant4 simulations

Previous studies [28] concerning the HPGe β detectors used in this experiment indicate that the difference between simulated and experimental spectra should not exceed the level of a few percent. The relatively low endpoint energy of 562 keV is comparable to the case of ^{85}Kr from Ref. [28]. The findings of Ref. [28] indicate that at this level of precision the effect of the different Geant4 models and simulation parameter values will be negligible. The simulated spectra of warm (isotropic) data measured at 1.2 K agree with the experimental ones up to 2-3% (see Figure 6), with the absence of systematic trends. Furthermore, results obtained in the lower energy region (i.e. 410-470 keV) indicate the absence of an energy dependence of the ratio \tilde{A}/A_{SM} . Finally, during the analysis of this experiment, ratios of count rates obtained for identical geometries (i.e. $N_{\text{cold}}/N_{\text{warm}}$) were constructed, so that many temperature independent systematic effects cancel, while others are reduced in size.

However, the observed large scattering of the ratio \tilde{A}/A_{SM} in the different temperature groups (Fig. 9) might indicate the presence of a small difference between simulated and experimental spectra. Therefore the statistical uncertainty of the weighted average was increased by a factor of $\sqrt{\chi_{red}^2}$, which we consider as a systematic error related to the Geant4 simulations. Therefore, full separation of “statistical” and “systematic” uncertainties becomes impossible at this stage.

4. Pile-up and dead time

The relatively high count rate during the experiment caused considerable pile-up and dead time in the electronics chain. The dead time of the system was monitored with a precision pulser signal fed to the preamplifier. The variation in the pile-up probability was determined by determining the ratio of the pulser peak and the tail at its right hand side (Fig. 3).

For the case of ^{67}Cu this ratio is then proportional to the probability of summing of two

events in the simulated spectra, with the proportionality factor determined from a fit to the warm spectrum. Generating simulated spectra for different values of this proportionality factor allows to estimate the effect of pile-up, yielding a 0.0028 uncertainty on the \tilde{A}/A_{SM} ratio.

For the case of ^{68}Cu the effect of pile-up (PU) can be described as

$$W(\theta) = \frac{N_C + N_C^{PU}}{N_W + N_W^{PU}} = \frac{N_C(1 + p_C)}{N_W(1 + p_W)} \quad (13)$$

with p_C (p_W) the pile-up probability for anisotropic (“cold”) respectively isotropic (“warm”) data. Based on the pulser tail/peak ratio the pile-up was the highest in the warm data, indicating that this effect reduces the observed anisotropy. As the fraction is measured to be 1.0003(26) we observe no reduction of anisotropy which means that the effect of pile-up is negligible at this level of precision for ^{68}Cu .

5. Half-life of ^{67}Cu

The experimental spectra of ^{67}Cu had to be corrected for the half-life of this isotope ($T_{1/2} = 61.83(12)$ h). Varying this value within the error bar induces a 0.0011 systematic uncertainty on the ratio \tilde{A}/A_{SM} .

The half-life of this isotope can also be obtained from an exponential fit to the three groups of isotropic data taken throughout the measuring campaign (see Fig. 5), resulting in $T_{1/2} = 61.07(12)$ h. The difference between this value and the above mentioned literature value induces a systematic shift of 0.0067 in the ratio \tilde{A}/A_{SM} which is used as a systematic error related to the half-life value.

The final value for the uncertainty related to the half-life of ^{67}Cu is obtained as the square sum of the two uncertainties mentioned above, which amounts to 0.0068

6. Geometry

The geometrical uncertainties related to the experimental setup (e.g. detector position) also induce systematic errors on the simulated spectra of ^{67}Cu . Varying the detector’s position within their uncertainties a systematic error of 0.0032 can be assigned to the ratio \tilde{A}/A_{SM} .

7. Hyperfine interaction μB

The uncertainties related to the magnetic moment μ and the total magnetic field B yield a total of 0.0003 systematic error on the ratio \tilde{A}/A_{SM} . Similar to the case of ^{68}Cu , the error on the hyperfine interaction experienced by the ^{67}Cu nuclei is dominated by the uncertainty related to the total magnetic field (see Sec. II E), therefore the corresponding errors were propagated by considering them fully correlated, yielding a total systematic error of 0.0006.

8. The β asymmetry parameter of two β branches

Considering an energy region where two β branches are present with $A^{1,2}$ asymmetry parameters and $\eta_{1,2}$ as weights (branching intensities), the observed effect W by a detector can then be written in the following form (see Eq. 5):

$$W(\theta) = 1 + \eta_1 f \tilde{A}^1 P \tilde{Q} + \eta_2 f \tilde{A}^2 P \tilde{Q}. \quad (14)$$

Therefore an effective asymmetry parameter A^{eff} can be introduced:

$$A^{\text{eff}} = \eta_1 \tilde{A}^1 + \eta_2 \tilde{A}^2. \quad (15)$$

One can then construct the ratio

$$\begin{aligned} \frac{\tilde{A}^{\text{eff}}}{A_{SM}^{\text{eff}}} &= \frac{\tilde{A}_1 + \frac{\eta_2}{\eta_1} \tilde{A}_2}{A_{SM}^1 + \frac{\eta_2}{\eta_1} A_{SM}^2} \\ &= \frac{A_{SM}^1 + \frac{\eta_2}{\eta_1} A_{SM}^2}{A_{SM}^1 + \frac{\eta_2}{\eta_1} A_{SM}^2} [1 + T] \end{aligned} \quad (16)$$

(see Eq. 12), where $T = \frac{\gamma m}{E} \Re \frac{C_T + C_T'}{C_A}$. Naturally the fraction in front of the factor $1 + T$ is equal to unity. However, the ratio of the branching intensities η_1/η_2 (see Tab. II) induces a systematic error of 0.022 on the ratio $\tilde{A}^{\text{eff}}/A_{SM}^{\text{eff}}$.

C. Total systematic error and final results

Adding, finally, all systematic errors for \tilde{A}/A_{SM} for ^{67}Cu in quadrature yields a value of 0.014, which is about 50% larger than the statistical error bar. The final result for the asymmetry parameter for the highest energetic β branch in the decay of ^{67}Cu then reads $\tilde{A}/A_{SM} = 0.973 \pm 0.010_{\text{stat}} \pm 0.014_{\text{syst}} = 0.973(17)$.

VII. STANDARD MODEL VALUE FOR \bar{A}

The Standard Model value of the correlation coefficients is modified at the percent level by the higher order corrections [42, 43]. Including the recoil, Coulomb and radiative corrections the β -asymmetry parameter can be written as [44]:

$$A_{SM} = \frac{F_4 + F_7/3 + \Delta F_4 + \Delta F_7/3 + \Delta R_3}{F_1 + \Delta F_1 + \Delta R_2} \quad (17)$$

where $F_{1,4,7}$ and $\Delta F_{1,4,7}$ are defined by Holstein [42], while the radiative corrections $\Delta R_{2,3}$ are from Yokoo and Morita [45]. By using the impulse approximation all recoil corrections can be expressed in terms of the nuclear matrix elements involved in the decay. For a pure Gamow-Teller decay these are mainly the M_{GT} , M_L , $M_{\sigma L}$ and M_{1y} matrix elements. The Gamow-Teller matrix element M_{GT} can be experimentally obtained from the relation [44, 46]:

$$M_{GT}^2 \simeq c^2 \simeq \frac{2\mathcal{F}t^{0^+ \rightarrow 0^+}}{(1 + \delta'_R)ft} \quad (18)$$

where $\mathcal{F}t^{0^+ \rightarrow 0^+} = 3071.8(8)$ s stands for the corrected ft value of the superallowed $0^+ \rightarrow 0^+$ transitions [7, 47] and δ'_R is a part of the “outer” radiative corrections which depends only on the electron energy and the atomic number Z of the daughter nucleus. For the case of a retarded Gamow-Teller transition, where M_{GT} is small, this relation is not accurate enough, and a shape correction factor $S(Z, W)$ needs to be included in the statistical rate function f . The expression for f then becomes

$$f_{exact} = \int_1^{W_0} pW(W_0 - W)^2 F(Z, W) S(Z, W) dW \quad (19)$$

where W (W_0) is the total electron (endpoint) energy in units of the electron rest mass $m_e c^2$, p is the electron momentum, $F(Z, W)$ is the Fermi function and $S(Z, W) = F_1(W)/c^2$ where $F_1(W)$ is the spectral function defined by Holstein [42].

All matrix elements mentioned above can also be computed using shell model calculations from the expression:

$$M = \sum_{j_1, j_2} \langle f | \left[a_{j_1}^\dagger a_{j_2} \right]^K | i \rangle \langle j_1 | \mathcal{O}^K | j_2 \rangle \quad (20)$$

where the first factor is the one-body density matrix element (OBDME) which is the expectation value of the creation and annihilation operators for j_1 and j_2 orbitals evaluated in the many-body initial and final states, $|i\rangle$ and $|f\rangle$. The OBDME depends only on the

rank K of the operator being evaluated, and the ones of interest here all have $K = 1$. The second factor is a single-particle matrix element and depends on the operator but not on the many-body physics included in the initial and final wave functions.

Shell model calculations were performed using the KB3 [48, 49], FPMI3 [50], GXPF1 [51], GXPF1A [52] and MSDI3 interactions with a ^{56}Ni core (closed $\pi f_{7/2}$ shell). As the computed M_{GT} matrix elements were in disagreement with the experimentally determined value, an iterative re-weighing method (using Eqs. 18 and 19) was applied to the OBDMEs. Because the corrections from this method were still very large, one hole was included in the $\pi f_{7/2}$ shell, thereby breaking the ^{56}Ni core. Repeating the procedure only for the supposedly best interaction GXPF1A now yielded significantly smaller corrections induced by the iterative re-weighing method. The results for the matrix elements thus obtained for both ^{67}Cu and ^{68}Cu are summarized in Tab. V, where the uncertainties are based on the scatter in the values observed during the re-weighing process.

Table V. Relevant nuclear matrix elements for the decay of ^{67}Cu and ^{68}Cu . The value of M_{GT} was obtained experimentally using Eq. 18. The other matrix elements were calculated within the shell model employing the GXPF1A interaction, with one hole in the $\pi f_{7/2}$ shell. The uncertainty connected to the values of the matrix elements is based on the scatter observed during the re-weighing process.

Matrix element	^{67}Cu	^{68}Cu
M_{GT}	0.0600(3)	0.102(6)
M_L	0.213(37)	0.349(15)
$M_{\sigma L}$	-0.257(22)	-0.814(8)
M_{1y}	7.91(41)	1.28(16)

The form factors occurring in the spectral functions $F_{1,4,7}(W)$ which determine both the shape factor $S(Z, W)$ and the recoil corrected value of A_{SM} (Eq. 17) are related to the nuclear matrix elements via the impulse approximation [42, 44]. Their values for ^{67}Cu are summarized in Tab. VI for the different interactions considered.

In the decay of ^{68}Cu the spin sequence ($1^+ \rightarrow 0^+$) ensures that the a, e, f, g, j_2, j_3 form factors are equal to zero [42]. For this isotope the same procedure was applied, i.e. the

Table VI. Overview of the form factors relevant for the decay of ^{67}Cu , calculated within the shell model using different interactions. The row marked “Final” lists the values obtained employing the re-weighting process (see text) and is used further in the analysis. Note that, except for d/Ac , these values are always situated between the outermost values obtained for the different interactions. The c form factor was experimentally determined to be 0.060 from Eq. 18. Note that A here stands for the atomic mass number, while A_{SM} is the Standard Model value of the β -asymmetry parameter including recoil, radiative and Coulomb corrections at 490 keV. The associated uncertainty of the final value is the square sum of the propagated uncertainties of the different matrix elements (see Tab. V).

Interaction	b/Ac	d/Ac	f/Ac	g/Ac	h/Ac	j_2/Ac	j_3/Ac	A_{SM}
KB3	2.6	-1.3	-0.87	8.4×10^4	2.4×10^5	-1.6×10^5	2.3×10^4	0.6010
FPMI3	2.7	-1.4	-0.86	8.2×10^4	2.5×10^5	-1.6×10^5	2.5×10^4	0.6012
GXPFI1	0.87	1.6	-0.75	7.2×10^4	1.2×10^5	-1.4×10^5	8.6×10^4	0.6002
GXPFI1A	-0.17	2.6	-0.79	7.6×10^4	1.1×10^5	-1.4×10^5	1.1×10^5	0.5995
MSDI3	-0.20	1.7	-0.60	5.7×10^4	7.5×10^4	-1.2×10^5	5.0×10^4	0.6002
Final	1.2	4.3	-0.73	6.9×10^4	1.4×10^5	-1.3×10^5	9.9×10^4	0.5998(2)

results of shell model calculations employing the GXPFI1A interaction were re-weighted until agreement with the experimentally determined value of M_{GT} was reached. Using the thus obtained form factors (see Tab. VII) one arrives at $A_{SM} = 0.9902(12)$, determined at 3700 keV. The error is based on the uncertainties of the matrix elements, see Tab. V. The relatively large correction of about 1% is due to the high energy region that is used for analysis. At lower energies this correction becomes significantly smaller (i.e. 0.0012 at 500 keV).

VIII. DISCUSSION

Our experimental result for the β asymmetry parameter of ^{67}Cu $\tilde{A}/A_{SM} = 0.973(17)$ indicates agreement with the Standard Model within 1.4σ . Combining this with the Standard Model prediction of 0.5998(2) yields $\tilde{A} = 0.584(10)$, one of the most accurate values for this parameter to date.

Table VII. The form factors relevant for the decay of ^{68}Cu , calculated within the shell model (GXPF1A interaction) using the re-weighing process (see text). The c form factor was experimentally determined to be 0.102 from Eq. 18. Note that the spin sequence ($1^+ \rightarrow 0^+$) ensures that the a, e, f, g, j_2, j_3 form factors are equal to zero.

Form factor	Value
b	-8.9
c	-0.102
d	-55
h	-1.9×10^5

To deduce limits on possible charged current weak tensor couplings Eq. 3 was used retaining terms linear as well as quadratic in C_T and C'_T but neglecting the imaginary couplings. The sensitivity factor $\gamma m/E_e$ is equal to 0.500 in the ROI (between 470 and 510 keV). The limits obtained from this measurement are $-0.002 < (C_T + C'_T)/C_A < 0.100$ (90% C.L.). A comparison of these limits with limits obtained from other recent precision measurements of correlation coefficients in nuclear β decay is shown on Fig. 10. As can be seen all measurements are consistent with the tensor coupling constants C_T and C'_T being equal to zero.

IX. CONCLUSIONS

The measurement of the β -asymmetry parameter in the decay of ^{67}Cu was presented. The technique of low temperature nuclear orientation was used in combination with Geant4 simulations to account for systematic effects such as electron scattering. An on-line measurement of the β -asymmetry parameter for ^{68}Cu was also performed for normalization purposes.

The experiment yielded a value of $\tilde{A} = 0.584(10)$, one of the most precise determination of this parameter to date and in agreement with the Standard Model prediction which was found to be $A_{SM} = 0.5998(2)$, including recoil, radiative and Coulomb corrections.

The results were interpreted in terms of possible time reversal invariant tensor currents in the weak interaction Hamiltonian. The limits obtained are competitive with limits from other measurements of correlations in neutron and nuclear β decay.

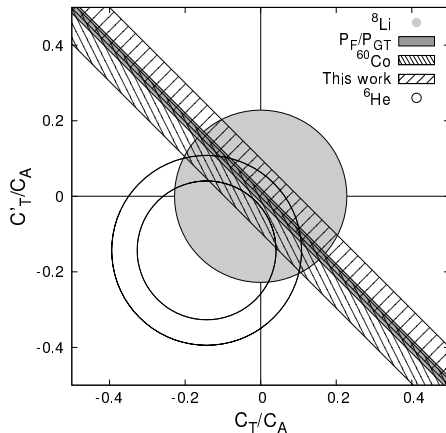


Figure 10. Limits (90% C.L.) on time reversal invariant tensor type coupling constants C_T and C_T' normalized to the axial-vector coupling constant C_A . The result of this work is shown together with results from other experiments in nuclear β decay: the $\alpha_{\beta\nu}$ measurement of ^6He [53, 54], the α - β - ν correlation of ^8Li [14], the \bar{A} measurement of ^{60}Co [12], the positron polarization in the decays of ^{14}O and ^{10}C [55]. Note that for drawing the bands, tensor couplings up to second order were retained.

Comparing the error budgets of this and previous β asymmetry parameter measurements using the low temperature nuclear orientation technique, [11, 12] it is clear that, besides some specific effects which can be reduced under favorable conditions, the main sources of error are the fraction determination, Geant4 related uncertainties and thermometry. As these effects are inherent to the present LTNO technology they will be limiting the accuracy of any future experiment of this type to a level of around 1%.

Recent reviews [56, 57] showed that low energy weak interaction experiments in neutron decay and nuclear β decay remain competitive with ongoing searches for new bosons at the TeV mass scale at the LHC with focusing on the Fierz term and if precisions at the 10^{-3} level are envisaged. This requires major modifications to the LTNO method as presently used, or application of a different type of method. In this respect we are setting up a new β spectrometer based on a combination of energy sensitive detectors and a multi-wire drift chamber for β particles as described in Refs. [58, 59].

ACKNOWLEDGMENTS

This work was supported by the Fund for Scientific Research Flanders (FWO), Projects GOA/2004/03 and GOA/2010/10 of the K. U. Leuven, the Interuniversity Attraction Poles Programme, Belgian State Belgian Science Policy (BriX network P6/23), and Grant LA08015 of the Ministry of Education of the Czech Republic.

- [1] T. Lee, C. Yang. *Physical Review* 104 (1956) 254–258
- [2] N. Severijns, M. Beck, O. Naviliat-Cuncic. *Reviews of Modern Physics* 78 (2006) 991–1040
- [3] H. Abele. *Progress in Particle and Nuclear Physics* 60 (2008) 1–81
- [4] G. Konrad, *et al.* In R. V. H. V. Klapdor-Kleingrothaus, I. V. Krivosheina, ed., *Physics Beyond the Standard Models of Particles, Cosmology and Astrophysics (Proc. 5th Int. Conf., Beyond 2010)* (2010) arXiv:1007.3027v2
- [5] H. P. Mumm, *et al.* *Physical Review Letters* 107 (2011) 102301
- [6] A. Kozela, *et al.* *Physical Review C* 85 (2012) 045501
- [7] N. Severijns, O. Naviliat-Cuncic. *Annual Review of Nuclear and Particle Science* 61 (2011) 23–46
- [8] J. R. A. Pitcairn, *et al.* *Physical Review C* 79 (2009) 015501
- [9] X. Fléchar, *et al.* *Journal of Physics G: Nuclear and Particle Physics* 38 (2011) 055101
- [10] P. A. Vetter, *et al.* *Physical Review C* 77 (2008) 035502
- [11] F. Wauters, *et al.* *Physical Review C* 80 (2009) 062501
- [12] F. Wauters, *et al.* *Physical Review C* 82 (2010) 055502
- [13] M. Beck, *et al.* *The European Physical Journal A* 47 (2011) 45
- [14] G. Li, *et al.* *Physical Review Letters* 110 (2013) 092502
- [15] J. Jackson, S. Treiman, J. H. Wyld. *Physical Review* 106 (1957) 517–521
- [16] R. Huber, *et al.* *Physical Review Letters* 90 (2003) 202301
- [17] N. Stone, H. Postma. *Low-Temperature Nuclear Orientation*. North-Holland, Amsterdam (1986)
- [18] P. Vingerhoets, *et al.* *Physical Review C* 82 (2010) 064311
- [19] H. Junde, H. Xiaolong, J. Tuli. *Nuclear Data Sheets* 106 (2005) 159–250

- [20] E. McCutchan. Nuclear Data Sheets 113 (2012) 1735–1870
- [21] U. Köster, *et al.* Nuclear Instruments and Methods in Physics Research Section B: Beam Interactions with Materials and Atoms 204 (2003) 303–313
- [22] U. Köster, *et al.* Nuclear Instruments and Methods in Physics Research Section B: Beam Interactions with Materials and Atoms 160 (2000) 528–535
- [23] L. Weissman, *et al.* Physical Review C 65 (2002) 044321
- [24] K. Schlösser, *et al.* Hyperfine Interactions 43 (1988) 139–149. 10.1007/BF02398294
- [25] J. Wouters, *et al.* Hyperfine Interactions 59 (1990) 59–75. 10.1007/BF02401194
- [26] D. Vénos, *et al.* Nuclear Instruments and Methods in Physics Research, Section A: Accelerators, Spectrometers, Detectors, and Associated Equipment 454 (2000) 403–408
- [27] D. Zákoucký, *et al.* Nuclear Instruments and Methods in Physics Research, Section A: Accelerators, Spectrometers, Detectors, and Associated Equipment 520 (2004) 80 – 83. Proceedings of the 10th International Workshop on Low Temperature Detectors
- [28] G. Soti. *submitted*
- [29] K. Krane. Low-Temperature Nuclear Orientation, chapter Nuclear Orientation Formalism, 31. North-Holland, Amsterdam (1986)
- [30] V. V. Golovko, *et al.* Physical Review C 84 (2011) 014323
- [31] S. Chikazumi. Physics of magnetism. J. Wiley and Sons, New York (1964)
- [32] H. Marshak. Low-Temperature Nuclear Orientation, chapter Nuclear Orientation Thermometry, 769 – 820. North-Holland, Amsterdam (1986)
- [33] T. Funk, *et al.* Journal of Magnetism and Magnetic Materials 195 (1999) 406–419
- [34] T. L. Shaw, N. J. Stone. Atomic Data and Nuclear Data Tables 42 (1989) 339 – 363
- [35] V. V. Golovko, *et al.* Physical Review C 74 (2006) 044313
- [36] M. Kontani, T. Hioki, Y. Masuda. Journal of the Physical Society of Japan 32 (1972) 416–428
- [37] E. Klein. Low-Temperature Nuclear Orientation, chapter Relaxation phenomena, 579. North-Holland, Amsterdam (1986)
- [38] S. Agostinelli, *et al.* Nuclear Instruments and Methods in Physics Research, Section A: Accelerators, Spectrometers, Detectors, and Associated Equipment 506 (2003) 250 – 303
- [39] F. Wauters, *et al.* Nuclear Instruments and Methods in Physics Research, Section A: Accelerators, Spectrometers, Detectors, and Associated Equipment 609 (2009) 156 – 164
- [40] F. Wauters. Search for tensor type weak currents by measuring the β -asymmetry parameter

- in nuclear decays. Ph.D. thesis, K.U. Leuven (2009)
- [41] D. Vénos, D. Zákoucký, N. Severijns. *Atomic Data and Nuclear Data Tables* 83 (2003) 1–44
- [42] B. R. Holstein. *Reviews of Modern Physics* 46 (1974) 789–814
- [43] B. R. Holstein. *Reviews of Modern Physics* 48 (1976) 673–673
- [44] V. de Leebeek. *in preparation*
- [45] Y. Yokoo, S. Suzuki, M. Morita. *Progress of Theoretical Physics* 50 (1973) 1894–1907
- [46] F. Calaprice, B. Holstein. *Nuclear Physics A* 273 (1976) 301 – 325
- [47] J. C. Hardy, I. S. Towner. *Physical Review C* 79 (2009) 055502
- [48] A. Poves, E. Pasquini, A. Zuker. *Physics Letters B* 82 (1979) 319–324
- [49] A. Poves, A. Zuker. *Physics Reports* 70 (1981) 235–314
- [50] W. Richter. *Nuclear Physics A* 523 (1991) 325–353
- [51] M. Honma, *et al.* *Physical Review C* 69 (2004) 1–34
- [52] M. Honma, *et al.* *The European Physical Journal A* 25 (2005) 499–502. 4th International Conference on Exotic Nuclei and Atomic Masses, Pine Mt, GA, SEP 12-16, 2004
- [53] C. Johnson, F. Pleasonton, T. Carlson. *Physical Review* 132 (1963) 1149
- [54] F. Glück. *Nuclear Physics A* 628 (1998) 493–502
- [55] A. Carnoy, *et al.* *Physical Review C* 43 (1991) 2825–2834
- [56] T. Bhattacharya, *et al.* *Physical Review D* 85 (2012) 1–29
- [57] O. Naviliat-Cuncic, M. González-Alonso. Prospects for precision measurements in nuclear β decay at the LHC era (2013). *Annalen der Physik*, to be published
- [58] K. Lojek, K. Bodek, M. Kuzniak. *Nuclear Instruments and Methods in Physics Research, Section A: Accelerators, Spectrometers, Detectors, and Associated Equipment* 611 (2009) 284 – 288
- [59] G. Ban, *et al.* *Nuclear Instruments and Methods in Physics Research Section A: Accelerators, Spectrometers, Detectors and Associated Equipment* 611 (2009) 198–202

Chapter 6

Measurement of the β spectrum shape

The search for physics beyond the standard model via precision correlation measurements has yielded results with relative uncertainties on the percent level. In the coming several years the sub-percent precision will be reached with experiments employing atom or ion traps. The great advantage of this approach is the essentially scatter-free environment, which enables very accurate determination of the angle between the decay products, leading to ever more accurate results.

In order to follow this trend, i.e. to further increase the accuracy of our β asymmetry measurements, the major sources of uncertainties have to be addressed. The effect of electron scattering in the host foil and from the detector, together with the fraction determination constitute the major part of the error budget of previous measurements. However, these effects are irreducible and inherent to the LTNO method. Reducing the error from the fraction determination to the permille level requires the asymmetry measurement of a γ transition accompanying the β decay, which will distort the β spectrum. Scattering can not be reduced therefore it has to be accounted for with Geant4 simulations. The uncertainties due to these simulations are related to the inner mechanics of the implemented physics models, the improvement of which is a task requiring many dedicated high precision measurements.

Trying to improve the precision of our β asymmetry measurements would require a significant amount of research and development, and subsequent modifications of the inner part of the dilution refrigerator. Rather than doing

this we decided to switch to another method, i.e. precision β spectrum shape measurements with a new type of β spectrometer which combines a scintillator detector for energy determination with a multi-wire drift chamber for tracking of scattered β particles. From the β spectrum shape the Fierz interference term can be extracted which provides information on tensor or scalar weak currents, depending on the type of β transition. With this setup, in addition, scattering can be investigated in detail, which will hopefully allow to reduce the uncertainties in the Geant4 simulation results.

It is to be noted also that the sub-percent precision values of the correlation coefficients can only impose limits on new physics if the higher order standard model corrections have been taken into account. The recoil corrections in the formalism developed by Holstein (see ref. [17] and section 2.1.2) influence the correlation coefficients up to about 1%. Although the theoretical framework has been developed several decades ago, not many dedicated experiments have been performed up till now. The few measurements were focusing on mirror transitions and isospin triplet systems of low masses ($A < 40$), while some current correlation results were obtained in a higher mass region [24, 81].

Performing β spectrum shape measurements for well-selected transitions with the new β spectrometer will also allow to address these recoil corrections.

6.1 Introduction

Besides correlation measurements with atom or ion traps the accurate measurement of the β spectrum shape can also give limits on the scalar and tensor coupling constants via the Fierz interference term. Furthermore, it is sensitive to the most important recoil term which induces an important systematic uncertainty on the standard model value of the β -asymmetry parameter A , i.e. weak magnetism. This novel approach is unique in terms of the experimental observable therefore its results do not share any systematic effects with other approaches.

A now outdated overview of the experimental status of spectrum shape measurements was given by Daniel [82]. Some of these measurements were used for CVC tests and determination of weak magnetism (the b form factor in the Holstein formalism) in the past. These works were focusing on the $A = 12$ (^{12}C , ^{12}N , ^{12}O) [83, 84, 85] and $A = 20$ (^{20}F , ^{20}Ne , ^{20}Na) [86, 87, 88] isospin triplet systems. The disagreement of the final results of these experiments indicates that the systematic effects, such as scattering or bremsstrahlung, might be significant. Geant4 simulations can aid in estimating these effects, increasing the reliability of any new experimental results.

The Fierz interference term was only once determined with good accuracy by a spectrum shape measurement using ^{114}In [89]. At low β energies, as will be shown later, extra care has to be taken with Geant4 simulations, especially regarding electron scattering. On the positive side, bremsstrahlung effects decrease with energy. Note that also high resolution semiconductor detectors can be used for these measurements, provided low Z detectors (i.e. Si) are used to limit the amount of backscattering.

6.1.1 Shape of the β spectrum

If one wants to extract accurate limits on new physics the existing physics has to be understood with high precision. Applying Fermi's Golden rule for β decay gives immediately the spectrum shape in the first approximation [90]:

$$d\lambda = \frac{2\pi}{\hbar} \langle \Psi_i | V | \Psi_f \rangle \rho(E) \rightarrow K p^2 (W_0 - W_e)^2 dp \quad (6.1)$$

where $K = \frac{|M_{fi}|^2 (m_e c^2)^2}{2\pi^3 \hbar^7 c^3}$ is a constant factor, $W = E_{kin}/m_e c^2 + 1$ and $p = \sqrt{W^2 - 1}$ is the electron/positron momentum. The largest correction to this is the Fermi function $F(Z, W)$ [91] which accounts for the Coulomb interaction between the (point-like and infinitely heavy) nucleus and the outgoing electron/positron.

$$F(Z, W) = 2(\gamma + 1)(2pR)^{2(\gamma-1)} e^{\pi\alpha ZW/p} \frac{|\Gamma(\gamma + i\alpha ZW/p)|^2}{\Gamma(2\gamma + 1)^2} \quad (6.2)$$

where R is the nuclear radius, α the fine structure constant and $\gamma = \sqrt{1 - \alpha^2 Z^2}$. Higher order corrections were studied in a series of articles by Wilkinson [91, 92, 93, 94] and are summarized in table 6.1. The relevant corrections have been incorporated in our β spectrum generator routine which is also used in the Geant4 LTNO code [95]. Including all corrections the expression for the β spectrum becomes:

$$d\lambda = K F R_N L_0 C R (W_0 - W_e)^2 p^2 dp \quad (6.3)$$

Factors that have not yet been mentioned are explained in table 6.1. The effects of some of these corrections are shown on figure 6.1. In the rest of this section some of these corrections will be discussed in more detail.

Radiative corrections

Unlike for other corrections, information on radiative corrections is spread out over a series of papers in literature. Therefore a detailed summary of the radiative corrections is given here, for clarity and future use.

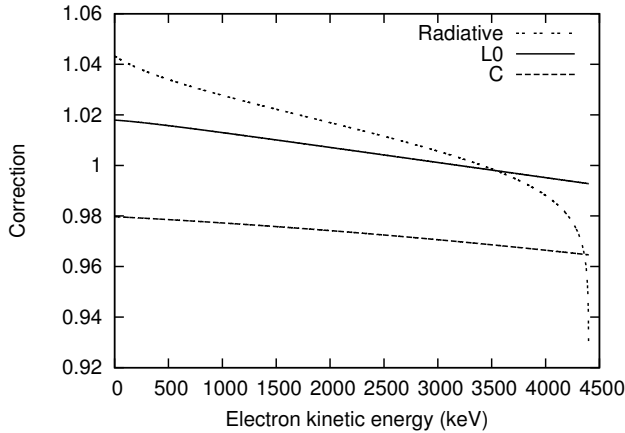


Figure 6.1: The effect of several corrections (14, 13 and 15 from table 6.1) to the β spectrum of ^{68}Cu .

During β decay photons may be exchanged between the charged participant particles or emitted into a free state. Furthermore Z^0 bosons can be also exchanged. These effects, called radiative corrections, can influence the β spectrum on the percent level. They are discussed in detail in papers by Wilkinson [93, 94]. Here just a short overview will be given. There are two classes of radiative corrections: *inner* and *outer*. The inner corrections are connected to the mechanics of the W boson, and for a pure Fermi transition they can be calculated, while for a Gamow-Teller transition they are included into the axial coupling constant. The outer corrections are independent on the strong and the weak interaction, and they include effects such as bremsstrahlung or hadronic photon exchange. These corrections can be expanded into a power series by $\alpha^n Z^{n-1}$. The order where these corrections converge is heavily Z dependent, see Table 6.2. Wilkinson's articles cover the radiative corrections up to third order in α :

$$R = 1 + \delta_1(W) + \delta_2(W, Z) + \delta_3(W, Z) \quad (6.4)$$

	Effect	Comment	Formula
1	Phase space factor	incorporated	$p^2(W_0 - W)^2 dp$ [91]
2	Neutrino mass	negligible	
3	Recoiling nucleus	incorporated	R_N [92]
4	Forbidden decays	not applicable	
5	Fierz term	our topic	$1 + b'$
6	Right handed currents	our topic	
7	“Traditional” Fermi function	incorporated	F [91]
8	Magnetic interaction between the electron and nucleus	to be investigated	
9	Coulomb screening	to be investigated	
10	Rearrangement of the electron shells	to be investigated	
11	Decay into a bound state	not applicable	
12	Effect of EC (for β^+)	not applicable	
13	Finite size of the nucleus	incorporated	L_0 [92]
14	Radiative corrections	incorporated	R [93, 94]
15	Nucleonic orbitals	incorporated	C [92]
16	Many body nuclear structure effects	our topic	$S(E)$

Table 6.1: Overview of the corrections on the β spectrum shape, according to Wilkinson [91]. The recoil corrections are denoted by “16. Many body nuclear structure effects”.

Order	Z			
	10	30	50	80
α	$7.3 \cdot 10^{-3}$	$7.3 \cdot 10^{-3}$	$7.3 \cdot 10^{-3}$	$7.3 \cdot 10^{-3}$
$\alpha^2 Z$	$5.3 \cdot 10^{-4}$	$1.6 \cdot 10^{-3}$	$2.7 \cdot 10^{-3}$	$4.3 \cdot 10^{-3}$
$\alpha^3 Z^2$	$3.9 \cdot 10^{-5}$	$3.5 \cdot 10^{-4}$	$9.7 \cdot 10^{-4}$	$2.5 \cdot 10^{-3}$

Table 6.2: The Z dependence of the $\alpha^n Z^{n-1}$ factor for different orders of radiative corrections.

The first order correction is $\delta_1 = \frac{\alpha}{2\pi} g(W_0, W)$, where g is defined by Sirlin [96]:

$$\begin{aligned}
g(W_0, W) = & 3 \ln \frac{m_p}{m_e} - \frac{3}{4} + \frac{4}{\beta} L_s \frac{2\beta}{1+\beta} + 4 \left(\frac{\tanh^{-1} \beta}{\beta} - 1 \right) \\
& \times \left[\frac{W_0 - W}{3W} - \frac{3}{2} + \ln 2(W_0 - W) \right] \\
& + \frac{\tanh^{-1} \beta}{\beta} \left[2(1 + \beta^2) + \frac{(W_0 - W)^2}{6W^2} - 4 \tanh^{-1} \beta \right]
\end{aligned} \tag{6.5}$$

where \tanh^{-1} is the inverse hyperbolic tangent function, $\beta = \sqrt{W^2 - 1}$ and

$$L_s = \int_0^x \frac{\ln(1-t)}{t} dt \equiv - \sum_{k=1}^{k=\infty} \frac{x^k}{k^2} \equiv -\text{Li}_2(x) \quad (6.6)$$

is the Spence function (also known as dilogarithm). The higher order corrections were derived for the pure Fermi (superallowed) transitions so their validity for mixed and Gamow-Teller transitions is questionable, but, as Wilkinson noted [94], they should not be very wrong. Furthermore, recently Severijns and Naviliat-Cuncic successfully used these to arrive to the V_{ud} matrix element from the mirror transitions [14]. Therefore it is useful to go forward and investigate these corrections as well. The second order term, which is proportional to $\alpha^2 Z$ has the following form [94]:

$$\delta_2(W, Z) = \alpha^2 Z \sum_{i=1}^4 \Delta_i(E) \quad (6.7)$$

where $\Delta_1 = \Delta_1^0 + \Delta_1^F$ (see below). The Δ_i are given by Jaus and Rasche [97] and final formulas by Sirlin [98]. In the extreme-relativistic approximation [94]

$$\Delta_1^0 + \Delta_4 = \ln \frac{m_p}{m_e} - \frac{5}{3} \ln 2W + \frac{43}{18} \quad (6.8)$$

which agrees reasonably well with numerical calculations without invoking this approximation. The others can be evaluated by using the uniformly charged sphere (of radius $R = r_0 A^{\frac{1}{3}} = \sqrt{\frac{5}{3}} \langle r^2 \rangle = \sqrt{10}/\Lambda$) model for the nucleus:

$$\begin{aligned} \Delta_1^F &= \ln \frac{\Lambda}{M} - \gamma_E + \frac{4}{3} - \ln \sqrt{10} - \frac{3}{2\pi\sqrt{10}} \left[\frac{1}{2} + \gamma_E + \ln \sqrt{10} \frac{\Lambda}{M} \right] \\ \Delta_2 &= \frac{3}{2\pi\sqrt{10}} \frac{\Lambda}{M} \left(1 - \frac{\pi}{2\sqrt{10}} \frac{\Lambda}{M} \right) \\ \Delta_3 &= \frac{3}{\pi\sqrt{10}} g_A g_M \frac{\Lambda}{M} \left[\gamma_E - 1 + \ln \sqrt{10} \frac{\Lambda}{M} + \frac{\pi}{4\sqrt{10}} \frac{\Lambda}{M} \right] \end{aligned} \quad (6.9)$$

Here $g_A = 1.265$, $g_M = 4.706$, the Euler-Mascheroni constant $\gamma_E \simeq 0.5772$, $\Lambda = \sqrt{6/\langle r^2 \rangle}$ with $\langle r^2 \rangle$ the rms charge radius, and M is the nucleon mass. Thus

$$\frac{\Lambda}{M} = \frac{\hbar c \sqrt{10}}{M r_0 A^{\frac{1}{3}}} \simeq \frac{0.665}{r_0 A^{\frac{1}{3}}} \quad (6.10)$$

where usually $r_0 = 1.2$ fm is used while Wilkinson [94] suggests the parameterization:

$$r_0(\text{fm}) = 1.614 - 0.1067 \ln A + 0.005456 \ln^2 A + \frac{6.112}{(A - 1.76)^2} \quad (6.11)$$

The third order corrections can be found in a paper by Sirlin and Zucchini [99] with typos and errors corrected by Wilkinson [94]. However, the derivation of this formula is labeled as “heuristic”, and its purpose is the evaluation of the error caused by stopping the expansion at second order in α . Here the radius R is in natural units.

$$\delta_3 = \alpha^3 Z^2 \left[a \ln \frac{\sqrt{10}}{RW} + bf(W) + \frac{4}{3\pi}g(W) - 0.649 \ln 2W_0 \right] \quad (6.12)$$

where

$$\begin{aligned} a &= \frac{\pi}{3} - \frac{3}{2\pi} \simeq 0.5697 \\ b &= \frac{4}{3\pi} \left(\frac{11}{4} - \gamma_E - \frac{\pi^2}{6} \right) \simeq 0.2240 \\ f(W) &= \ln 2W - \frac{5}{6} \\ g(W) &= \frac{1}{2} (\ln^2 R - \ln^2 2W) + \frac{5}{3} \ln 2RW \end{aligned} \quad (6.13)$$

Other effects

The majority of the other effects (e.g. effects 8 to 10 in Table 6.1) are of atomic nature thus influencing the spectrum shape only at low energies, i.e. below 50 keV. As the β particle leaves the nucleus the effect of the Coulomb interaction is described by the Fermi function. However, the nuclear charge is screened by the atomic electrons so the Fermi function is modified. This effect is called Coulomb screening. Also, the sudden change of the nuclear charge during decay can induce atomic excitation and internal ionization. Further, atomic exchange happens when the β particle decays directly into a bound state of the daughter nucleus, while a bound electron makes a transition into the continuum [100]. More detailed investigation is required in order to fully understand the significance of these effects at play below about 50 keV.

6.1.2 Fierz interference term

The Fierz term, as introduced in section 2.1.2, also influences the β spectrum as is the case for other correlation coefficients. From equation 2.3 for the case of unpolarized nuclei ($\langle \mathbf{J} \rangle = 0$) one can see that it essentially is a multiplicative

factor of the form $1 + b \frac{m}{E_e} = 1 + b'$. It depends on the real parts of the scalar and tensor coupling constants with the following limits (95.5% C.L.) [13]:

$$\begin{aligned} |C_S/C_V| < 0.070, & \quad |C_T/C_A| < 0.090, \\ |C'_S/C_V| < 0.067, & \quad |C'_T/C_A| < 0.089. \end{aligned} \quad (6.14)$$

Meanwhile newer measurements (see chapter 2.2.4) further reduced these limits to the several percent level so in the coming feasibility study we will “search” for a 2% effect.

Note that due to the factor $1/E_e$ spectrum shape measurements are most sensitive to scalar and tensor contributions to the weak interactions if β transitions with low β endpoint energy are used.

6.1.3 Recoil corrections

The recoil corrections, introduced in chapter 2.1.2, apply not only to the correlation coefficients but also to the β spectrum shape. It is given by the H_0 spectral function [17, 18] which depends on the b , d , e and h form factors. The experimental observable in this case is the spectrum shape $S(E)$ which is usually normalized at E_m , the energy with the most counts in the beta spectrum:

$$S(E) = \frac{H_0(E, J, J', 0)}{H_0(E_m, J, J', 0)} \quad (6.15)$$

However, for the purposes of this feasibility study we will normalize $S(E)$ at 0 kinetic energy.

$$\begin{aligned} H_0 = & |a_1|^2 + \frac{2a_1a_2}{3M^2} \left[m_e^2 + 4EE_0 + 2\frac{m_e^2}{E}E_0 - 4E^2 \right] \\ & + |c_1|^2 + \frac{2c_1c_2}{9M^2} \left[11m_e^2 + 20EE_0 - 2\frac{m_e^2}{E}E_0 - 20E^2 \right] \\ & - \frac{2E_0}{3M} (c_1^2 + dc_1 \pm bc_1) + \frac{2E}{3M} (3a_1^2 + 5c_1^2 \pm 2bc_1) \\ & - \frac{m_e^2}{3ME} \{ -3a_1e + c_1 [2c_1 + d \pm 2b - h(E_0 - E)/2M] \} \end{aligned} \quad (6.16)$$

where the upper (lower) sign stands for negative (positive) β decay. M stands for the nuclear mass, m_e is the electron mass, E is the total electron energy ($E = m_e c^2 + E_{kin}$) while E_0 is the total endpoint energy. Choosing a pure Gamow-Teller transition the a_1 , a_2 and e form factors drop out so only c , b ,

d , and h remain. Furthermore we can neglect c_2 , meaning that $c = c_1$. By measuring the spectrum shape one is only sensitive to the energy-dependent terms since an overall multiplicative factor only influences the half-life. Therefore it is useful to rewrite the above equation:

$$H_0 = f_1(c, b, d) + E f_2(c, b) + E^2 f_3(c_1, c_2) + \frac{1}{E} f_4(c, b, d, h) \quad (6.17)$$

To first order in M only f_1 and f_2 are non-zero and for a pure GT transition they have the following form:

$$\begin{aligned} f_1 &= c^2 - \frac{2E_0}{3M}(c^2 + dc \pm bc) \\ f_2 &= \frac{2}{3M}(5c^2 \pm 2bc) \end{aligned} \quad (6.18)$$

In this approximation $S(E) = f_1 + f_2 E$ (see figure 6.2), and if one normalizes it at 0 kinetic energy it will have the form of $1 + \frac{f_2 E}{f_1}$. Its relative effect over the whole spectrum (so that $E = E_0$, see figure 6.2) can be quantified as:

$$\frac{f_2 E_0}{f_1} \simeq \frac{5c \pm 2b}{\frac{3M}{2E_0} c - c - d \mp b} \simeq \frac{2E_0}{3M} \left(5 \pm 2 \frac{b}{c} \right) \quad (6.19)$$

which yields for some typical values of the form factors [19] an effect up to a percent. This sets the first requirement for an experiment: the precision reached should be such that a percent effect in the spectrum shape would be clearly visible. The linear dependence of the effect on the endpoint energy means that isotopes with high endpoint energies are most suitable for studying the weak magnetism recoil term. At higher energies the Fierz term (see chapter 2.1.2) diminishes making the extraction of the spectrum shape easier.

If one requires higher accuracy the $1/E$ term f_4 can also be included. In the same approximation as the linear term it has the following form:

$$f_4 = -\frac{m_e^2}{3M} c \left(2c + d \pm 2b - h \frac{E_0 - E}{2M} \right) \quad (6.20)$$

where the h recoil term has been retained because it is usually of the order of 10^5 .

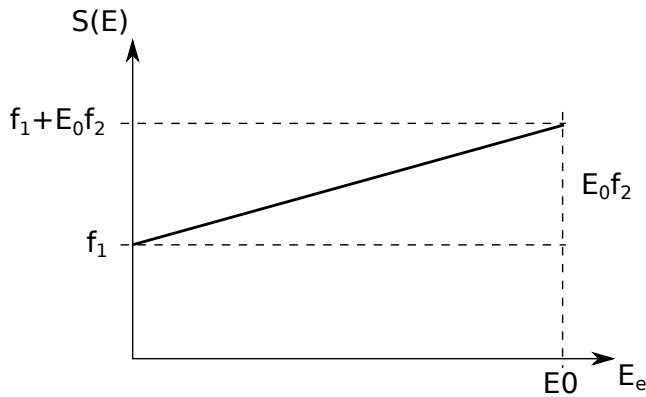


Figure 6.2: The effect of the recoil corrections $S(E)$ in function of the electron energy.

6.2 Experimental requirements

Statistics

Already at the design stage of the experiment one can estimate the required number of counts in a β spectrum for a precise determination of $S(E)$ or the Fierz term. Both effects are significant at the percent level, meaning that the spectrum shape should be determined with higher precision.

The effect of the recoil terms $S(E)$ is, to first order, linear in energy and can be of the order of several percent. In order to investigate the accuracy with which such a linear effect can be obtained from experimental data, numerical calculations were performed in ROOT [101]. First, random numbers were generated according to the distribution $1 + fx$ ($f = 0.02$, to mimic a 2% effect) in a hypothetical energy range of 0-1710 keV which was fitted with a first order polynomial. It turns out that already 10^6 events ensure an uncertainty below a percent on f . Changing bin size or endpoint energy did not influence the accuracy of the fit, which allows us to conclude that it is fully determined by the amount of events. However, a realistic β spectrum is not uniform, but contains less counts near the edges. In order to incorporate this effect into the analysis, random numbers were generated according to the theoretically calculated spectrum shape of ^{32}P (endpoint energy of 1710 keV), arriving to a calculated spectrum. This procedure was repeated to include the recoil corrections in the form of $1 + \frac{f}{E_0} E$ ($f = 0.02$, to mimic a 2% linear effect over the whole energy range). The ratio R of the distorted and the “regular”

calculated spectrum should leave only the 2% effect with the appropriate statistical artifacts, and can be then fitted with a straight line (i.e. $R = a + bE$, where $f = E_0 b/a$; see figure 6.3) However, as the determination of f involves

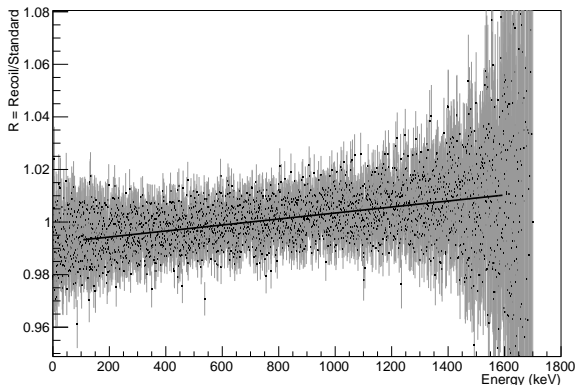


Figure 6.3: Ratio R of calculated spectra (10^8 events), with and without recoil corrections, fitted with $R = a + bE$. The added effect was $f = 0.02$, and the fit resulted in $f = 0.0197(11)$ in the region from 100 to 1600 keV.

both fitted parameters a and b the parameter uncertainties reported by ROOT need to be increased [102]. This was verified by performing the fit a thousand times on ratios of different calculated spectra. The spread of the f values (the σ resulting from the Gaussian fit of the f values) was the same as the increased ROOT errors. A simple transformation of the fit function, $R = a(1 + bE)$, would require only one parameter to determine f (i.e. $f = b/E_0$) implying that the ROOT errors should not be increased. However, repeating the procedure of performing the fit a thousand times, yielded a larger spread for the f values than what was initially reported by ROOT. This indicates that the ROOT errors should be increased regardless on the number of parameters to be used later on, in contradiction with the guidelines of F. James [102]. This topic certainly requires a much deeper investigation.

For the purposes of this feasibility study we will use $R = a + bE$ as the fit function, duly taking into account the increased errors from ROOT and also the correlations between a and b . The results of fits for different amounts of events are summarized in table 6.3.

The effect of the Fierz term ($1 + \gamma \frac{m}{E_e} b$, see chapter 2.1.2) is only significant at low energies, so for the feasibility study we used the β spectrum of ^{45}Ca with

Events	Fit result f
10^7	0.018(3)
10^8	0.0197(11)
10^9	0.0198(3)

Table 6.3: The fitted linear effect f to the ratio R of calculated spectra, with and without recoil corrections, for different amount of events. The fit was performed in the region between 100 and 1600 keV. The initial β spectrum was distorted with a 2% effect over the whole energy region.

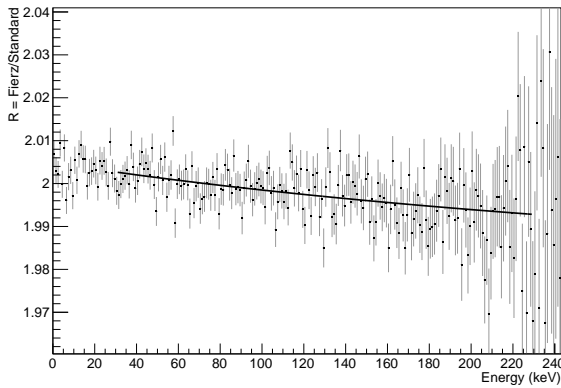


Figure 6.4: Ratio of calculated spectra (10^8 events), with and without the Fierz term (fixed at 0.02). It was fitted with $a(1 + b\gamma\frac{m}{E_e})$, and the fit resulted in $b = 0.0206(11)$ in the region from 30 to 230 keV.

an endpoint energy of 255.8 keV. A procedure similar to the one used for the recoil correction studies was followed in this case. Ratios of calculated spectra with and without a Fierz term ($b = 0.02$) were fitted using $a(1 + b\gamma\frac{m}{E_e})$ with a being a normalization factor (see figure 6.4). The results are summarized in table 6.4.

Detector resolution

The next topic to be investigated is the required detector resolution which flattens the features of the experimental spectrum. In a β spectrum there are no sharp peaks but the effect is nonetheless there, possibly masking the small

Events	Fit result b
10^7	0.019(3)
10^8	0.0206(11)
10^9	0.0199(3)

Table 6.4: Results of the fit of b_{Fierz} (fixed at 0.02) for different amounts of counts in the spectrum of ^{45}Ca .

effect of recoil terms in $S(E)$. Two types of detectors are considered for this experiment, a semiconductor detector and a scintillation detector, both having significantly different energy resolution. A typical semiconductor detector has around 5 keV resolution for β particles, while a scintillator has at least 50 keV, depending on the type. Intuitively the 5 keV resolution will not matter much when measuring a 4000 keV endpoint energy spectrum, however the question remains: for a given endpoint energy which is the maximum resolution that still gives acceptable results?

The procedure from the previous section was repeated, i.e. calculated spectra of ^{32}P with and without the recoil corrections, and including the effect of detector resolution, were constructed. The reported uncertainties did not change significantly as compared to the case without detector resolution (see table 6.3). This, however, is only valid if one can measure the detector resolution over the whole energy range of interest.

6.3 Detector response

Besides the energy resolution another requirement for the detector employed in β spectrum measurements is its thickness, i.e. it should be able to fully stop high energy electrons. The drawback of the semiconductor detectors in this case is that their thickness is limited by the purity of the material. The HPGe detectors already discussed in chapter 5 have a thickness of 4 mm, however the rear dead layer reduces the depleted region down to around 3 mm. Pure silicon detectors (PIPS) have a maximum thickness of 1.5 mm while the Si(Li) detectors can be made thicker (i.e. up to 5 mm) because the Li compensates the other impurities. Scintillation detectors can be made much thicker, but their worse resolution might offset this advantage, however. In order to investigate the detector thickness required to stop electrons of different kinetic energies one can employ the continuous slowing down approximation (CSDA) with the results summarized in table 6.5. Based solely on this table one can conclude that the current HPGe and Si(Li) detectors can be used to measure electrons

Energy [MeV]	Ge [mm]	Si [mm]
0.6	0.7	1.2
0.8	0.9	1.8
1	1.2	2.3
2	2.7	5.1
3	4.0	7.8
4	5.3	10.4
5	6.5	12.8

Table 6.5: CSDA range for Si and Ge from NIST ESTAR database [103].

with energies up to 2 MeV. However, the CSDA integrates the total stopping power in function of energy, and therefore is not taking into account energy fluctuations. These fluctuations induce a “smearing” of the electron range. To get a feeling for this Geant4 simulations were performed. Monoenergetic electrons were shot at a very basic model of the available detectors (Si, HPGe, and scintillator) and all outgoing particles were recorded. The outcome of each event was sorted into one of the categories:

- *full energy deposition*, when the electron stops in the detector, depositing all of its energy;
- *backscatter*, when the electron deposits some energy in the detector and exits into the half-sphere defined by the direction it came from;
- *transmission*, when the electron deposits some energy in the detector and exits into the half-sphere complementary to the backscatter half-sphere;
- *bremstrahlung*, when a bremstrahlung photon escapes the detector, thus reducing the deposited energy;
- *mixed events*, when a bremstrahlung photon together with an electron escapes from the detector. This typically happens at higher energies, when the initial electron traverses the detector and also creates bremstrahlung photons.

These simulations therefore allow getting a good idea of the response of the different detector type and therefore on their suitability for β spectrum shape measurements.

An important issue in this respect is the fact that the backscattering decreases with the incident electron energy while the bremstrahlung increases, so that there is a point (E_C , table 6.6) where the two effects have the same probability.

Since the wire chamber can only signal the presence of backscattered events, the bremsstrahlung has to be accounted for by simulations. In a precision measurement one would like to keep these simulation corrections as small as possible, so it is important to determine E_C for every type of detector.

Planar HPGe detectors

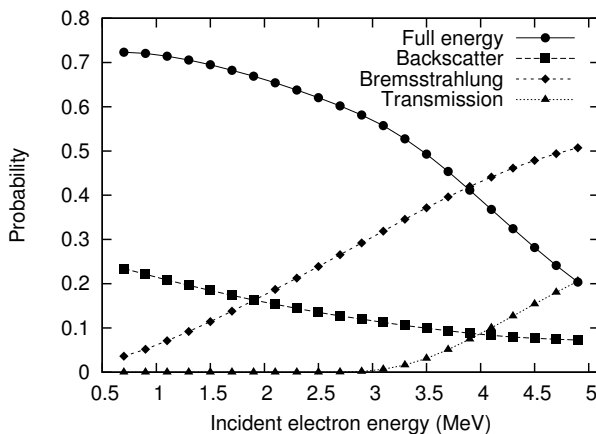


Figure 6.5: Probabilities for the different possible outcomes when an electron hits a 3 mm thick slab of Ge.

The HPGe detectors have an average thickness of 4 mm, which, according to table 6.5, should be enough to stop around 3 MeV electrons. Detailed Geant4 simulations show that they are usable up to around 3.7 MeV, above which the transmission probability rises above 5% (see figure 6.5). At those energies the backscattering coefficients is around 10%. However, a much bigger effect is the escape of bremsstrahlung γ rays. One can easily determine the value of E_C to be approximately 2 MeV. Figure 6.6 shows spectra of monoenergetic electrons of different initial energies.

Si detectors

Currently there are two types of Si detectors: PIPS and Si(Li). The former are made of pure silicon and are quite small: $1.5 \times 10 \times 10 \text{ mm}^3$. The Si(Li) detectors are doped with Li to compensate for the impurities, and thus can be made significantly thicker, up to 5 mm, with diameters up to 37 mm. They

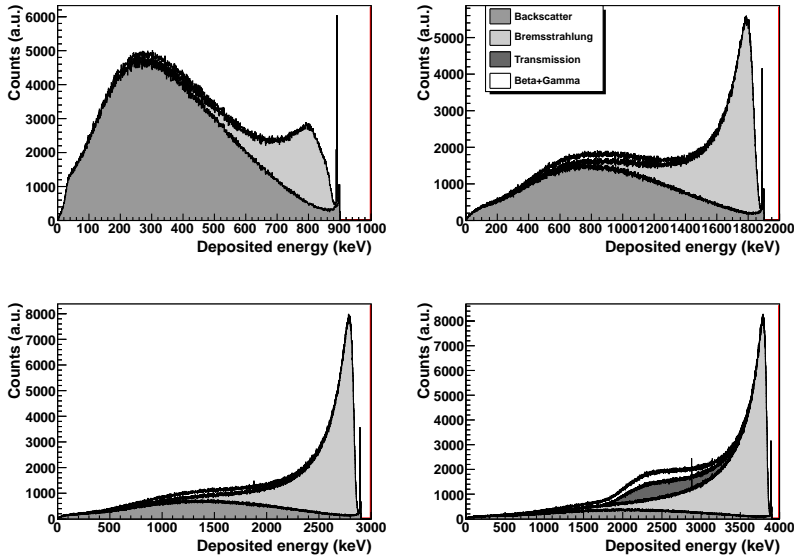


Figure 6.6: Response of the 4 mm thick HPGe detector to monoenergetic electrons of 0.9, 1.9, 2.9 and 3.9 MeV. The peak showing near the full energy is the X-ray escape, while the full energy peak is removed for clarity. The incoming electron can also create an electron-positron pair, giving rise to the double escape peak appearing on the two lower graphs at 1878 and 2878 keV, respectively.

also have an approximately 30 nm thick gold entrance window, while the PIPS detector has a very thin grid of Al covering only 3% of its surface. Figures 6.7 and 6.8 show that the gold layer on the Si(Li) detector does not influence the backscattering coefficient significantly. The PIPS detector is not limited by the bremsstrahlung effects, the E_C for this detector is 1.7 MeV which is much higher than the energy of about 0.7 MeV where transmission becomes significant. The Si(Li) detector would be useful for up to 2.2 MeV (which is still fully stopped), however, it is limited down to $E_C = 1.7$ MeV by bremsstrahlung escape.

Scintillators

Scintillators have the advantage that their size can be much bigger than the typical size of the semiconductor detectors discussed before. This has two advantages: it can stop electrons with higher energies and also can reduce the

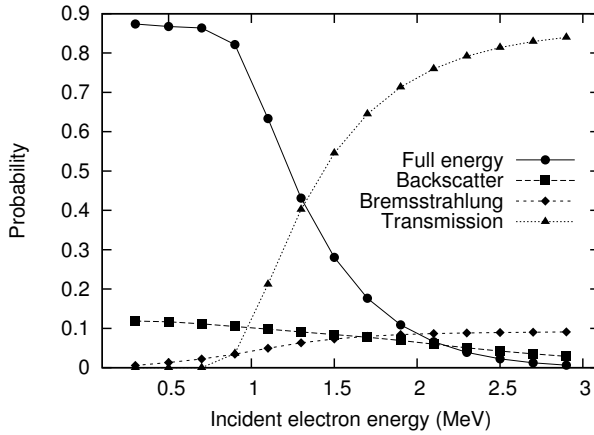


Figure 6.7: Probabilities of different outcomes for an event when an electron hits a 1.5 mm thick slab of Si PIPS detector.

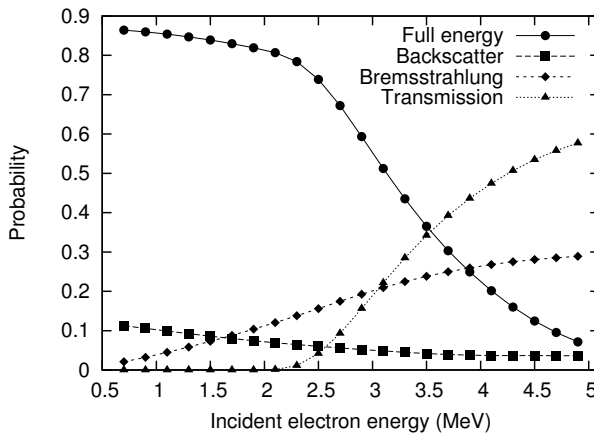


Figure 6.8: Probabilities for the different possible outcomes when an electron hits a 5 mm thick Si(Li) detector.

bremsstrahlung escape. Furthermore, by choosing an organic scintillator, the average Z of the material is reduced with respect to Si, leading to a decreased bremsstrahlung escape (which is proportional to Z^2). A well known fact, which is also demonstrated by the investigation of the two semiconductor detectors (Si and Ge), is the increase of the backscattering coefficient with Z , so a low- Z

material should be advantageous from this perspective as well. For testing purposes a plastic scintillator (BC-400 by Saint-Gobain, $10 \times 10 \times 1 \text{ cm}^3$) is already used in combination with the wire chamber. Figure 6.9 shows that a 10 mm thick plastic scintillator can stop electrons with kinetic energies up to 2 MeV and further simulations show that a 20 mm thick one would stop up to 3.7 MeV electrons. Further, backscattering is at a very low level, while bremsstrahlung escape is limited as well. Figure 6.10 shows spectra of monoenergetic electrons of different initial kinetic energies.

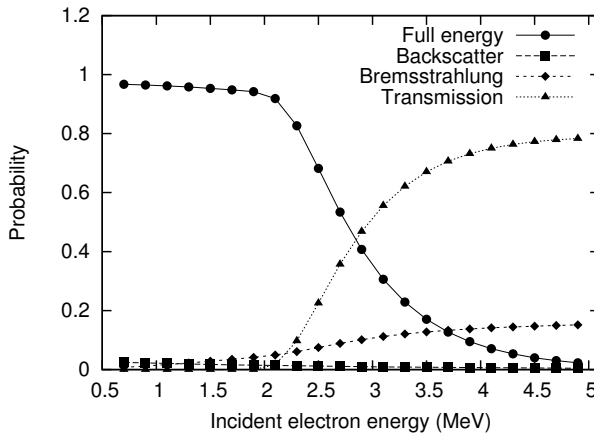


Figure 6.9: Probabilities for the different possible outcomes when an electron hits a 1 cm thick plastic scintillator (BC-400 by Saint-Gobain).

Conclusions

The final choice of the energy sensitive detector will depend on several factors. A disadvantage of the HPGe detectors is its required operating temperature of 77 K. The Si detectors represent a good choice, however, some types of these must be operated in vacuum. The plastic scintillators have the advantage of low bremsstrahlung escape which means that despite their relatively low E_C (see table 6.6) they are useful up to much higher energies. Since the prototype and the test setup both use a plastic scintillator the first measurements will be performed with this detector type.

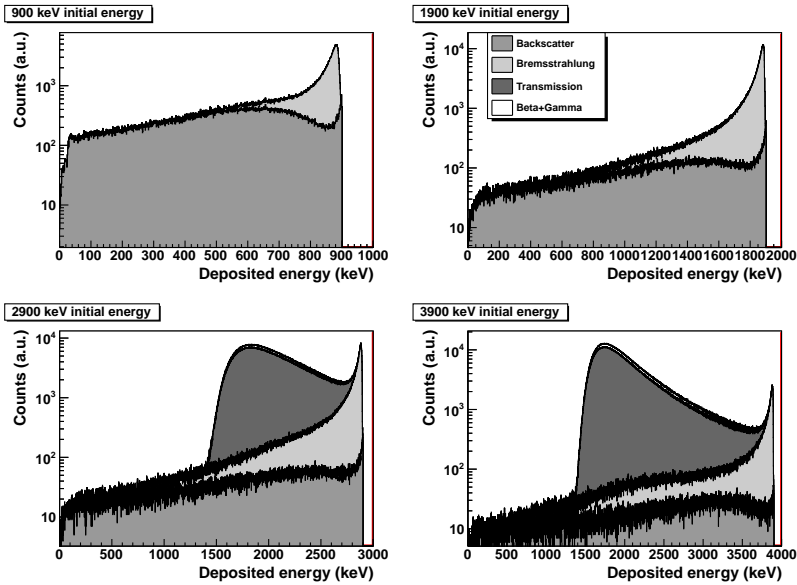


Figure 6.10: Simulated spectra of monoenergetic electrons with different initial energies (900, 1900, 2900 and 3900 keV). The detector is a 10 mm thick plastic scintillator. The constant dE/dx transmission peak is clearly visible around 2000 keV for the cases when the initial electron energy is 2900 and 3900 keV.

Detector	Thickness (mm)	E_C (MeV)	E_{tot} (MeV)	Resolution (keV)
HPGe	4	1.9	3.7	5
PIPS	1.5	1.7	0.7	5
Si(Li)	5	1.7	2.1	50
Scintillator	10	1.2	2.0	100

Table 6.6: Overview of the relevant detector properties. The quoted energy resolutions are at E_{tot} and come from the manufacturer’s data sheets, while the scintillator’s resolution stems from a dedicated measurement [104]

6.4 Setup

It is clear from the previous sections that a regular spectrum measurement with a radioactive source in front of a semiconductor detector will not result

in a clean energy spectrum. As was shown in section 6.3, at energies below 2 MeV the dominant distorting effect is the backscattering of electrons from the detector. To filter out such events one would have to detect all backscattered electrons. One of the possibilities is to use a wire chamber which has high efficiency for electrons and can easily cover the whole hemisphere. The active gas in the detector should be a low mass and low Z material to minimize energy losses and angular straggling. A prototype of such a wire chamber was already investigated by a group based in Krakow [105]. High detection efficiency (up to 95%) was achieved even at low pressures (around 300 mbar) using helium gas with 10 – 30% isobutane. In order to increase the sensitivity for tracking this wire chamber functions as a drift-chamber, meaning that within one cell the drift velocity (v_d) of the secondary electrons is constant. The energy detector provides a common start signal so the drift time (t_d) can be measured for the cells which registered a hit. The original trajectory is reconstructed by requiring that it touches the circles of radii $v_d t_d$ around the signal wires. Further

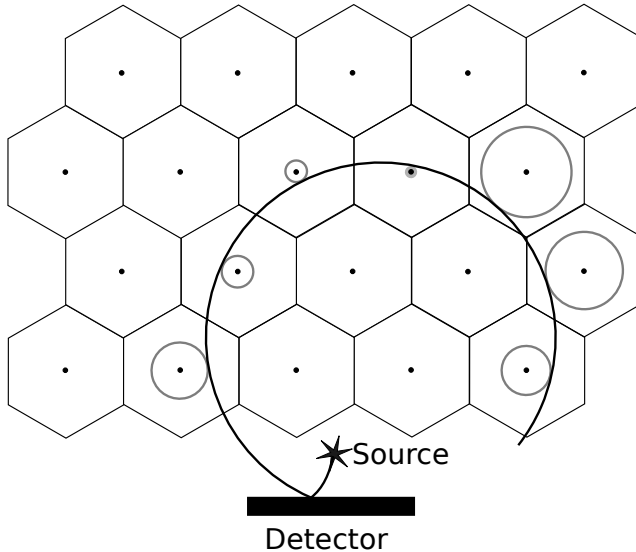


Figure 6.11: A particle detector with the wire chamber in front of it. The black dots represent the signal wires, while the vertices of the hexagons are the field wires. An electron, coming from the source, hits the detector and backscatters into the wire chamber. The gray circles represent hits, with radii $v_d t_d$.

investigation, as mentioned in the paper by Lojek et. al. [105], showed that a hexagonal cell structure would be more advantageous (see figure 6.11). In such a structure the wire density is lower resulting in a lower probability for

the electrons to scatter off the wires. Furthermore all field wires are at the same potential so the power supply, as well as the wire frame boards are much simpler. The third spatial component (z) will be obtained by employing the charge division technique. This requires that the signal wires have non-negligible resistance. One then measures the amount of charge on both ends of the wire, knowing that their ratio is proportional to the position along the wire where the charge was collected. This provides further information about the electron track and can help disentangle complex events with multiple tracks.

Finally, an external magnetic field can be applied so the tracks become curved, which then provides an additional measurement of energy. Calculations show that a field of roughly 0.1 T is needed to have a trajectory curvature of around 5-30 cm in the typical energy range of 500-5000 keV. If the hexagonal cell retains the same resolution as the rectangular one (around 0.5 mm [105]) in the plane perpendicular to the signal wires and if the fitting of the track retains this accuracy, the energy resolution from the track radius measurement can be below 10 keV.

6.4.1 Operating principle

Figure 6.11 shows the arrangement of the energy sensitive detector, source and wire chamber. The source holder should be very thin and possibly made from a low Z material in order to minimize the energy losses and scattering of the β particles. Radioactivity in the form of a liquid solution can e.g. be dried onto a typical, 10 μm thick mylar foil in which the energy loss for an electron is around 3 keV. A drift chamber needs a common start or stop signal in order to determine the drift times, which is provided by the energy detector. The wire chamber is read out (i.e. the drift time for each cell is determined) when the detector registers an event. A fitting routine determines the presence of tracks. If none is registered after a hit in the scintillation detector it means it was an event with full energy deposition (but with possible bremsstrahlung escape though). If a track is observed this means that the electron has backscattered so the event gets a tag. This way a “clean”, backscatter-free spectrum can be recorded. However, since the backscattering coefficient is energy dependent one can not simply discard the backscattered events. This energy dependence can be determined in two ways. A direct, dedicated experiment is described in section 6.6. Another way is to record both the deposited energy in the solid state detector and the energy obtained by the curvature radius of the backscattered track. Depending on the energy resolution of the wire chamber this can be good enough for an accurate measurement of the β particle’s energy.

The entire setup is designed and built in collaboration with the Jagiellonian

University in Krakow, Poland. The construction of the wirechamber is finished and it is now ready for commissioning (scheduled for July 2013), while the data acquisition system still requires some additional improvements. The entire system is expected to be shipped to Leuven in September 2013.

6.5 Which isotope to measure?

In order to measure the small effects of the Fierz term or of the recoil terms one needs a good understanding of the “classical” spectrum shape. The best understood β transitions are the allowed ones ($\Delta J = 0, \pm 1$ and $\Delta \pi = 1$). Also, a relatively low $\log ft$ value is required, since a high value implies that the leading order matrix elements (Fermi and Gamow-Teller) are reduced and the allowed shape is not guaranteed.

6.5.1 Recoil terms

The ideal candidate for a measurement of the weak magnetism recoil term must fulfill several additional criteria to the ones mentioned above. A high endpoint energy means that the effect of $S(E)$ is bigger (given the recoil terms are the same), while a low $\log ft$ ensures an unhindered transition meaning the c , b and d are not reduced [19]. The combination of these two conditions, however, almost automatically means a very short halflife which is not practical for a measurement in the wire chamber. Even in an on-line laboratory (e.g. ISOLDE) the time required for collecting a source in a foil and mounting it into the wire chamber would put a lower limit on the halflife of the order of minutes. Furthermore, a β^- and ground state to ground state transition is preferred so one does not have pile-up events with the γ rays coming from positron annihilation and/or from the decay itself. In this case the full β spectrum can be used for analysis.

De Leebeek et al. [19] compiled several tables of nuclei for which the weak magnetism term b has already been determined. Out of the “triplet nuclei” only ^{18}F and ^{30}P have a half life longer than a minute. Both are β^+ emitters with endpoint energies of 633 and 3210 keV, respectively. The halflife of the so called “mirror nuclei” is longer than a minute only for the low masses. The properties of these isotopes are summarized in table 6.7. Out of these only ^{30}P is not produced at ISOLDE. Table 6.8 lists several isotopes with long half lives for off line measurements and testing purposes.

Transition	$T_{1/2}$	E_0 [keV]	g.s. \rightarrow g.s.
$^{18}\text{F} \rightarrow ^{18}\text{O}$	109.8 min	633	yes
$^{30}\text{P} \rightarrow ^{30}\text{Si}$	150 s	3210	no
$^{11}\text{C} \rightarrow ^{11}\text{B}$	20.4 min	960	yes
$^{13}\text{N} \rightarrow ^{13}\text{C}$	9.96 min	1198	yes
$^{15}\text{O} \rightarrow ^{15}\text{N}$	122 s	1732	yes
$^{17}\text{F} \rightarrow ^{17}\text{O}$	64.5 s	1738	no

Table 6.7: List of mirror and triplet nuclei with halfives longer than a minute. All are β^+ emitters. ^{17}F only has a very weak (0.017%, $E_0 = 870$ keV) branch to an excited state while ^{30}P decays with 0.05% probability via a branch with almost 1 MeV endpoint energy to an excited state in ^{30}S .

Transition	Spin sequence	$T_{1/2}$	E_0 [keV]	$\log ft$	g.s. \rightarrow g.s.
$^{32}\text{P} \rightarrow ^{32}\text{S}^a$	$1^+ \rightarrow 0^+$	14.27 d	1711	7.9	yes
$^{56}\text{Mn} \rightarrow ^{56}\text{Fe}$	$3^+ \rightarrow 2^+$	2.58 h	2850	7.1	no
$^{61}\text{Co} \rightarrow ^{61}\text{Ni}$	$7/2^- \rightarrow 5/2^-$	1.65 h	1254	5.24	no
$^{114}\text{In} \rightarrow ^{114}\text{Sn}^b$	$1^+ \rightarrow 0^+$	71.9 s	1989	4.47	yes

^a One can also prepare a sample of ^{32}Si ($T_{1/2} = 153$ y) which decays to ^{32}P with a g.s. to g.s. β transition of $E_0 = 227$ keV.

^b One actually prepares a sample of $^{114\text{m}}\text{In}$ ($T_{1/2} = 49.5$ d) which decays to the ground state emitting a 79% converted γ ray of 190 keV.

Table 6.8: List of interesting isotopes for a recoil measurement.

The recoil corrections can also be calculated within the nuclear shell model, however the complexity of the calculations rises with the atomic mass of the nucleus considered. Already the corrections to the β -asymmetry parameter A for ^{60}Co were calculated in a truncated and not a full model space [24]. Therefore it is advisable to restrict the candidate isotope to low masses.

6.5.2 Fierz term

For a Fierz term measurement low endpoint energy is preferred. Some interesting isotopes are summarized in table 6.9. With the exception of ^{14}C they are all mixed transitions.

Second forbidden unique transitions ($\Delta J = 2$, $\Delta\pi = -1$) are also good candidates for a Fierz term measurement since their spectrum shape is known

Transition	Spin sequence	$T_{1/2}$		E_0 [keV]	$\log ft$
$^{14}\text{C} \rightarrow ^{14}\text{N}$	$0^+ \rightarrow 1^+$	5700	y	156.5	9.04
$^{33}\text{P} \rightarrow ^{33}\text{S}$	$1/2^+ \rightarrow 3/2^+$	25.35	d	248.5	5.02
$^{35}\text{S} \rightarrow ^{35}\text{Cl}$	$3/2^+ \rightarrow 3/2^+$	87.4	d	167.3	5.01
$^{45}\text{Ca} \rightarrow ^{45}\text{Sc}^a$	$7/2^- \rightarrow 7/2^-$	163	d	255.8	6.0
$^{63}\text{Ni} \rightarrow ^{63}\text{Cu}$	$1/2^- \rightarrow 3/2^-$	101.1	y	66.9	6.7

^a There is another, 0.002% intense β branch with $E_0 = 243.4$ keV.

Table 6.9: Some candidates for a Fierz term measurement. All the isotopes are β^- emitters.

in a closed form. However, the radiative corrections, as discussed in section 6.1.1 are applicable only to allowed decay.

^{14}C is interesting for one more reason: its anomalously long half-life of 5700(30) y (or equivalently a very high $\log ft$) is in contradiction with the fact that it decays via a Gamow-Teller transition. The Gamow-Teller matrix element M_{GT} has been determined to be $2 \cdot 10^{-3}$ contrary to its typical value of 1. This fact has triggered a lot of experiments in the past [106, 107, 108, 109]. An accurate measurement of its spectrum shape could, besides the search for the Fierz term, provide valuable input to the theoretical understanding of this nucleus [110, 111].

6.6 Geant4 improvements

The modular nature of the wire chamber described in section 6.4 allows performing also other measurements than the spectrum shape. Indeed, one can also perform electron scattering and transmission experiments, thereby providing valuable input data to the Geant4 collaboration. In this section several possible modifications to the wire chamber are proposed aiming at different goals.

Electron backscattering measurements

A detailed investigation of the backscattering of electrons would provide data to validate the Geant4 electromagnetic physics models. A high precision measurement of the backscattering probabilities, together with the angular distribution can rather easily be accomplished with the wire chamber described in this chapter. The detector in the wire chamber (see figure 6.11) can be replaced

with any piece of material that one wants to investigate. By fitting all the tracks (backscattered and regular) one can extract the energy dependent backscattering coefficients, together with angular distribution information. The drawback of this method is that the electron energy has to be determined from the track curvature, which can become complicated for a backscattered event. The use of a conversion electron source, providing monoenergetic electrons, would be a good solution since γ rays don't interfere with this kind of measurements. Table 6.10 lists some potential isotopes for such a measurement.

^{133}Ba	^{113}Sn	^{207}Bi
45.0	363.8	481.7
75.3	387.5	553.8
79.8	390.9	565.8
240.4		975.7
266.9		1047.8
320.0		1059.8
347.9		
350.3		

Table 6.10: List of the main conversion electron energies for ^{133}Ba , ^{113}Sn and ^{207}Bi to be used in electron backscattering measurements.

Electron bremsstrahlung measurements

By using a HPGe detector in combination with a high endpoint energy β emitter the bremsstrahlung losses start to dominate the spectrum, as per figure 6.5. One can validate the Geant4 models against such data.

Electron transmission measurements

Also transmission measurements, especially the angular distribution of the electrons after scattering would provide benchmark data for the Geant4 multiple scattering models. These models are of the condensed type, meaning that they provide a distribution of the scattering angle and of the lateral displacement. A direct measurement of the scattering angle for different thicknesses of scatterers would provide valuable data to calibrate these models. One possible arrangement is that one end of the wire chamber is connected to an electron accelerator with the entrance window being the scatterer, as shown on figure 6.12. Instead of an accelerator, monoenergetic conversion electron sources can be used as well.

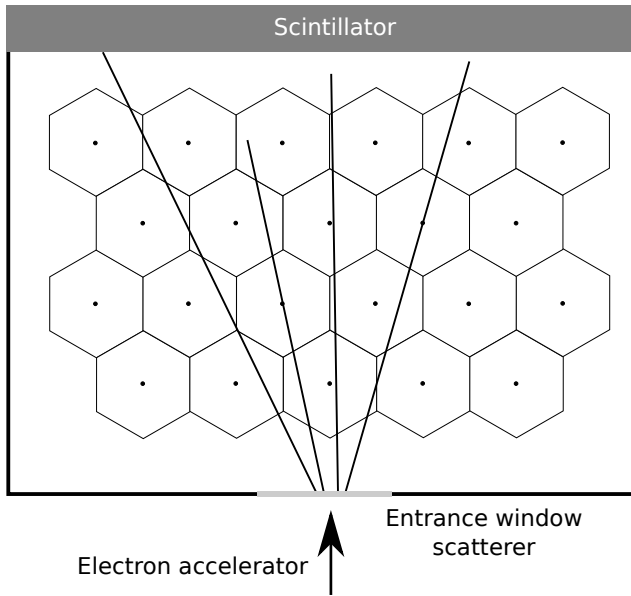


Figure 6.12: Scheme of the wire chamber configured for electron transmission measurements. The electrons from the accelerator traverse the entrance window which acts as the scatterer. The angular distribution can be recorded with the wire chamber behind.

Chapter 7

Conclusions

The precision measurement of the β asymmetry parameter \tilde{A} in a pure Gamow-Teller type decay with low β endpoint energy can provide stringent limits on possible charged tensor currents in the weak interaction Hamiltonian.

In this thesis the measurement of \tilde{A} in the decay of ^{67}Cu is presented. The experiment was performed using the NICOLE setup at ISOLDE (CERN), employing the technique of low temperature nuclear orientation. A ^3He - ^4He dilution refrigerator cooled to milliKelvin temperatures an iron foil, into which the radioactive nuclei were implanted. The orienting magnetic field was provided by a split-coil superconducting magnet. The asymmetric emission of the β particles was observed with custom made planar high purity germanium (HPGe) detectors, mounted inside the 4 K radiation shield. The detectors were directly facing the sample foil, minimizing the scattering of the β particles. Large volume HPGe detectors were positioned outside the cryostat in order to monitor the sample temperature. An on-line measurement of the β asymmetry parameter in the decay of ^{68}Cu was also performed for normalisation purposes.

In order to reach higher levels of accuracy the entire experimental setup was modeled within Geant4. The simulations performed are used in the data analysis to account for systematic effects, such as electron scattering on the detectors and the surrounding material or the influence of the magnetic field on the electron's trajectories. Since the simulations play such a crucial role, a significant amount of time and effort was spent on assessing their quality. Optimal values for different simulation parameters and the choice of electron multiple scattering model were based on the comparison of experimental and simulated spectra using different particle detectors and radioactive isotopes.

Before interpreting the obtained results in terms of new physics, higher order recoil and radiative corrections to the Standard Model value of the A parameter need to be taken into account. Using shell-model calculations these corrections were determined to be relatively small (10^{-4} level), yielding $A = 0.5998(2)$. The experimental value of the \tilde{A} parameter is $0.584(10)$, in agreement with the Standard Model prediction. This provides competitive limits on the time reversal invariant tensor coupling constants C_T and C'_T .

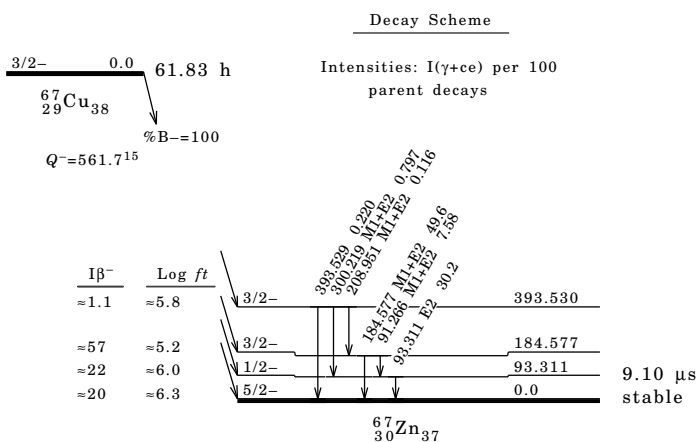
As to possible future measurements of the \tilde{A} parameter with the low temperature nuclear orientation technique, one has to analyse the error budget of not only this, but past experiments as well. Besides some specific effects, the uncertainty of the fraction determination is one of the dominant components. Reducing the main source(s) of error might be possible. However, at the sub-percent level several effects (e.g. thermometry, geometry of the setup) inherent to this technique appear which will be limiting the precision of future experiments to a level of around 1%. Therefore it is better to look into new methods in order to lower the errors of future measurements below this level.

Precision β spectrum shape measurements can provide competitive limits on scalar or tensor couplings in the weak interaction Hamiltonian via the Fierz interference term. A feasibility study was performed as part of this work and such measurements are in preparation. They will use a new type of β spectrometer, combining a scintillation detector for energy determination with a multi-wire drift chamber for tracking of backscattered particles. With the same setup the recoil terms can also be measured by choosing a suitable isotope.

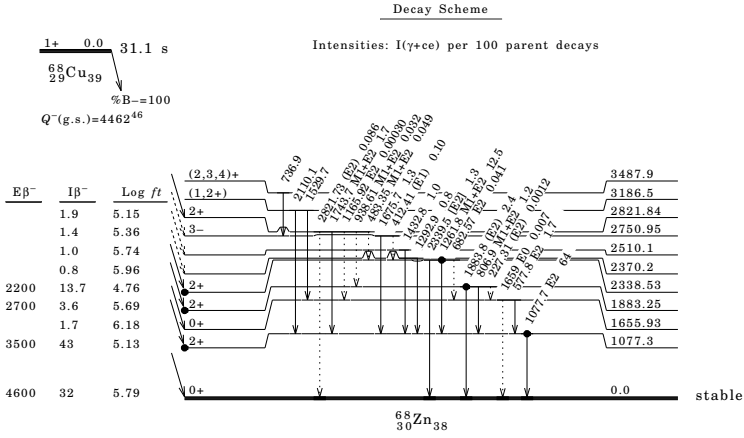
Appendix A

Decay schemes

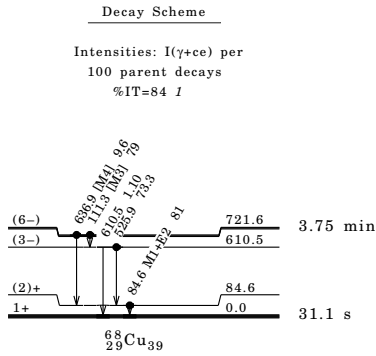
^{67}Cu β^- Decay 1978Me10,1969Ra15,1953Ea11



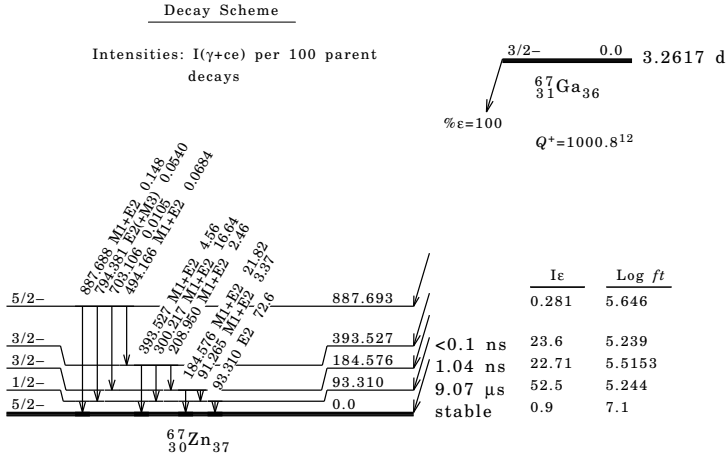
⁶⁸Cu β- Decay (31.1 s) 1972Sw01,1975Ti01



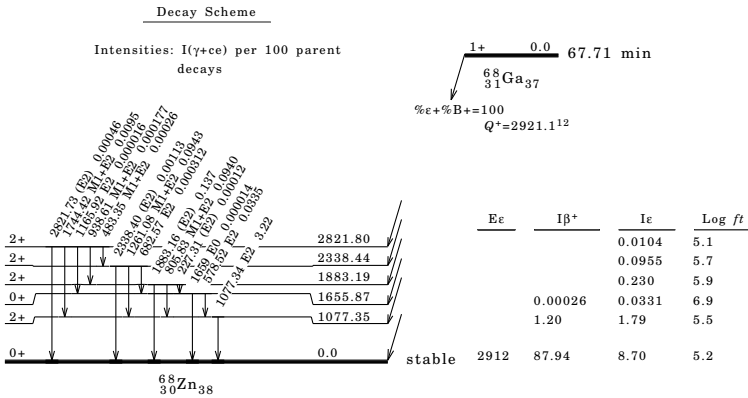
⁶⁸Cu IT Decay (3.75 min)



⁶⁷Ga ε Decay 2005Ya01,1978Me10



⁶⁸Ga ε Decay 1999BeZQ,1999BeZS



Bibliography

- [1] S. L. Glashow, “Partial-symmetries of weak interactions,” *Nuclear Physics*, vol. 22, pp. 579–588, Feb. 1961. pages 4
- [2] S. Weinberg, “A Model of Leptons,” *Physical Review Letters*, vol. 19, pp. 1264–1266, Nov. 1967. pages 4
- [3] E. Fermi, “Theorie der beta-strahlen,” *Zeitschrift fur Physik A Hadrons and Nuclei*, vol. 88, pp. 161–177, 1934. pages 5
- [4] F. L. Wilson, “Fermi’s Theory of Beta Decay,” *American Journal of Physics*, vol. 36, no. 12, p. 1150, 1968. pages 5
- [5] E. C. G. Sudershan and R. E. Marshak, “Chiralilty invariance and the universal fermi interaction,” *Physical Review*, vol. 109, no. 5, pp. 1860 – 1862, 1958. pages 5
- [6] T. Lee and C. Yang, “Question of parity conservation in weak interactions,” *Physical Review*, vol. 104, no. 1, pp. 254–258, 1956. pages 5, 6
- [7] C. Wu, E. Ambler, R. Hayward, D. Hopper, and R. Hudson, “Experimental test of parity conservation in beta decay,” *Physical Review*, vol. 105, p. 1413, 1957. pages 5
- [8] M. Goldhaber, L. Grodzins, and A. W. Sunyar, “Helicity of neutrinos,” *Physical Review*, vol. 109, p. 1015, 1957. pages 5
- [9] R. Garwin, L. Lederman, and M. Weinrich, “Observations of the Failure of Conservation of Parity and Charge Conjugation in Meson Decays: the Magnetic Moment of the Free Muon,” *Physical Review*, vol. 105, pp. 1415–1417, Feb. 1957. pages 5
- [10] J. Jackson, S. Treiman, and J. H. Wyld, “Possible tests of time reversal invariance in beta decay,” *Physical Review*, vol. 106, no. 3, pp. 517 –521, 1957. pages 6, 7, 8, 10, 20

- [11] M. Gell-Mann, "Test of the Nature of the Vector Interaction in β Decay," *Physical Review*, vol. 111, no. 1, pp. 362–365, 1958. pages 6
- [12] M. Rho, "Quenching of axial-vector coupling constant in β -decay and pion-nucleus optical potential," *Nuclear Physics A*, vol. 231, no. 3, pp. 493–503, 1974. pages 6
- [13] N. Severijns, M. Beck, and O. Naviliat-Cuncic, "Tests of the standard electroweak model in beta decay," *Reviews of Modern Physics*, vol. 78, pp. 991–1040, 2006. pages 7, 12, 14, 15, 18, 106
- [14] N. Severijns and O. Naviliat-Cuncic, "Symmetry Tests in Nuclear Beta Decay," *Annual Review of Nuclear and Particle Science*, vol. 61, pp. 23–46, Nov. 2011. pages 7, 16, 104
- [15] J. C. Hardy and I. S. Towner, "Superaligned $0^+ \rightarrow 0^+$ nuclear beta decays: A new survey with precision tests of the conserved vector current hypothesis and the standard model," *Physical Review C*, vol. 79, no. 5, p. 055502, 2009. pages 8, 14, 16
- [16] R. Huber, J. Lang, S. Navert, J. Stromicki, K. Bodek, S. Kistryn, J. Zejma, O. Naviliat-Cuncic, E. Stephan, and W. Haeberli, "Search for time-reversal violation in the β -decay of polarized ^8Li nuclei," *Physical Review Letters*, vol. 90, no. 20, p. 202301, 2003. pages 9
- [17] B. R. Holstein, "Recoil effects in allowed beta decay: The elementary particle approach," *Reviews of Modern Physics*, vol. 46, pp. 789–814, Oct 1974. pages 11, 100, 106
- [18] B. R. Holstein, "Erratum: Recoil effects in allowed beta decay: The elementary particle approach," *Reviews of Modern Physics*, vol. 48, pp. 673–673, Oct 1976. pages 11, 106
- [19] V. de Leebeek, "*in preparation*.". pages 12, 107, 120
- [20] P. Herczeg, "Beta decay beyond the standard model," *Progress in Particle and Nuclear Physics*, vol. 46, pp. 413 – 457, 2001. pages 12, 14
- [21] V. Cirigliano, M. González-Alonso, and M. L. Graesser, "Non-standard Charged Current Interactions: beta decays versus the LHC." arXiv 1210.4553, 2012. pages 12, 14
- [22] T. Bhattacharya, V. Cirigliano, S. Cohen, A. Filipuzzi, M. González-Alonso, M. Graesser, R. Gupta, and H.-W. Lin, "Probing novel scalar and tensor interactions from (ultra)cold neutrons to the LHC," *Physical Review D*, vol. 85, pp. 1–29, Mar. 2012. pages 12

- [23] V. Cirigliano, J. P. Jenkins, and M. González-alonso, “Semileptonic decays of light quarks beyond the Standard Model,” *Nuclear Physics B*, vol. 830, no. 1-2, pp. 95–115, 2010. pages 13
- [24] F. Wauters, I. Kraev, D. Zákoucký, M. Beck, M. Breitenfeldt, V. De Leebeeck, V. V. Golovko, V. Y. Kozlov, T. Phalet, S. Rocchia, G. Soti, M. Tandecki, I. S. Towner, E. Traykov, S. Van Gorp, and N. Severijns, “Precision measurements of the ^{60}Co β -asymmetry parameter in search for tensor currents in weak interactions,” *Physical Review C*, vol. 82, no. 5, p. 055502, 2010. pages 15, 16, 34, 100, 121
- [25] S.-C. Hung, K. Krane, and D. Shirley, “Beta-decay asymmetry from the decays of oriented ^{52}Mn and ^{60}Co ,” *Physical Review C*, vol. 14, no. 3, pp. 1162 – 1173, 1976. pages 16
- [26] L. M. Chirovsky, W.-P. Lee, A. M. Sabbas, A. J. Becker, J. L. Groves, and C. Wu, “Nuclear orientation facility for the study of the angular distribution of γ radiation and β particles emitted by polarized nuclei,” *Nuclear Instruments and Methods in Physics Research*, vol. 219, pp. 103–110, Jan. 1984. pages 16
- [27] F. Wauters, V. D. Leebeeck, I. Kraev, M. Tandecki, E. Traykov, S. V. Gorp, N. Severijns, and D. Zákoucký, “ β asymmetry parameter in the decay of ^{114}In ,” *Physical Review C*, vol. 80, no. 6, p. 062501, 2009. pages 16, 34
- [28] F. P. Calaprice, S. Freedman, W. Mead, and V. H.C., “Experimental study of weak magnetism and second-class interaction effects in the β decay of polarized ^{19}Ne ,” *Physical Review Letters*, vol. 35, no. 23, pp. 1566 – 1570, 1975. pages 16
- [29] H. Abele, “The neutron. Its properties and basic interactions,” *Progress in Particle and Nuclear Physics*, vol. 60, pp. 1–81, Jan. 2008. pages 16
- [30] J. S. Nico, “Neutron beta decay,” *Journal of Physics G: Nuclear and Particle Physics*, vol. 36, p. 104001, Oct. 2009. pages 16
- [31] G. Konrad, W. Heil, S. Baeßler, D. Pocanic, and F. Glück, “Impact of neutron decay experiments on non-standard model physics,” in *Physics Beyond the Standard Models of Particles, Cosmology and Astrophysics (Proc. 5th Int. Conf., Beyond 2010)* (R. V. H. V. Klapdor-Kleingrothaus, I. V. Krivosheina, ed.), 2010. pages 16
- [32] J. Beringer, J. F. Arguin, R. M. Barnett, K. Copic, O. Dahl, D. E. Groom, C. J. Lin, J. Lys, H. Murayama, C. G. Wohl, W. M. Yao, P. A. Zyla, C. Amsler, M. Antonelli, D. M. Asner, H. Baer, H. R. Band,

- T. Basaglia, C. W. Bauer, J. J. Beatty, V. I. Belousov, E. Bergren, G. Bernardi, W. Bertl, S. Bethke, H. Bichsel, O. Biebel, E. Blucher, S. Blusk, G. Brooijmans, O. Buchmueller, R. N. Cahn, M. Carena, A. Ceccucci, D. Chakraborty, M. C. Chen, R. S. Chivukula, G. Cowan, G. D'Ambrosio, T. Damour, D. de Florian, A. de Gouvêa, T. DeGrand, P. de Jong, G. Dissertori, B. Dobrescu, M. Doser, M. Drees, D. A. Edwards, S. Eidelman, J. Erler, V. V. Ezhela, W. Fetscher, B. D. Fields, B. Foster, T. K. Gaiser, L. Garren, H. J. Gerber, G. Gerbier, T. Gherghetta, S. Golwala, M. Goodman, C. Grab, A. V. Gritsan, J. F. Grivaz, M. Grünewald, A. Gurtu, T. Gutsche, H. E. Haber, K. Hagiwara, C. Hagmann, C. Hanhart, S. Hashimoto, K. G. Hayes, M. Heffner, B. Heltsley, J. J. Hernández-Rey, K. Hikasa, A. Höcker, J. Holder, A. Holtkamp, J. Huston, J. D. Jackson, K. F. Johnson, T. Junk, D. Karlen, D. Kirkby, S. R. Klein, E. Klempt, R. V. Kowalewski, F. Krauss, M. Kreps, B. Krusche, Y. V. Kuyanov, Y. Kwon, O. Lahav, J. Laiho, P. Langacker, A. Liddle, Z. Ligeti, T. M. Liss, L. Littenberg, K. S. Lugovsky, S. B. Lugovsky, T. Mannel, A. V. Manohar, W. J. Marciano, A. D. Martin, A. Masoni, J. Matthews, D. Milstead, R. Miquel, K. Mönig, F. Moortgat, K. Nakamura, M. Narain, P. Nason, S. Navas, M. Neubert, P. Nevski, Y. Nir, K. A. Olive, L. Pape, J. Parsons, C. Patrignani, J. A. Peacock, S. T. Petcov, A. Piepke, A. Pomarol, G. Punzi, A. Quadt, S. Raby, G. Raffelt, B. N. Ratcliff, P. Richardson, S. Roesler, S. Rolli, A. Romaniouk, L. J. Rosenberg, J. L. Rosner, C. T. Sachrajda, Y. Sakai, G. P. Salam, S. Sarkar, F. Sauli, O. Schneider, K. Scholberg, D. Scott, W. G. Seligman, M. H. Shaevitz, S. R. Sharpe, M. Silari, T. Sjöstrand, P. Skands, J. G. Smith, G. F. Smoot, S. Spanier, H. Spieler, A. Stahl, T. Stanev, S. L. Stone, T. Sumiyoshi, M. J. Syphers, F. Takahashi, M. Tanabashi, J. Terning, M. Titov, N. P. Tkachenko, N. A. Törnqvist, D. Tovey, G. Valencia, K. van Bibber, G. Venanzoni, M. G. Vincter, P. Vogel, A. Vogt, W. Walkowiak, C. W. Walter, D. R. Ward, T. Watari, G. Weiglein, E. J. Weinberg, L. R. Wiencke, L. Wolfenstein, J. Womersley, C. L. Woody, R. L. Workman, A. Yamamoto, G. P. Zeller, O. V. Zenin, J. Zhang, R. Y. Zhu, G. Harper, V. S. Lugovsky, and P. Schaffner, "Review of particle physics," *Physical Review D*, vol. 86, p. 010001, Jul 2012. pages 16
- [33] I. S. Towner and J. C. Hardy, "The evaluation of V_{ud} and its impact on the unitarity of the Cabibbo-Kobayashi-Maskawa quark-mixing matrix," *Reports on Progress in Physics*, vol. 73, p. 046301, Apr. 2010. pages 16
- [34] N. Severijns and O. Naviliat-Cuncic, "Structure and symmetries of the weak interaction in nuclear beta decay," *Physica Scripta*, vol. T152, p. 014018, Jan. 2013. pages 16

- [35] Y. Mostovoi, I. Kuznetsov, V. Solovei, A. Serebrov, I. Stepanenko, T. Baranova, A. Vasiliev, Y. Rudnev, B. Yerozolimsky, M. Dewey, F. Wietfeldt, O. Zimmer, and V. Nesvizhevsky, “Experimental value of G_A/G_V from a measurement of both P-odd correlations in free-neutron decay,” *Physics of Atomic Nuclei*, vol. 64, pp. 1955–1960, 2001. 10.1134/1.1423745. pages 17
- [36] H. Abele, M. Astruc Hoffmann, S. Baeßler, D. Dubbers, F. Glück, U. Müller, V. Nesvizhevsky, J. Reich, and O. Zimmer, “Is the unitarity of the quark-mixing ckm matrix violated in neutron β -decay?,” *Physical Review Letters*, vol. 88, no. 21, p. 211801, 2002. pages 17
- [37] D. Mund, B. Märkisch, M. Deissenroth, J. Krempel, M. Schumann, H. Abele, A. Petoukhov, and T. Soldner, “Determination of the Weak Axial Vector Coupling $\lambda=g_A/g_V$ from a Measurement of the β -Asymmetry Parameter A in Neutron Beta Decay,” *Physical Review Letters*, vol. 110, p. 172502, Apr. 2013. pages 17
- [38] M. P. Mendenhall, R. W. Pattie, Y. Bagdasarova, D. B. Berguno, L. J. Broussard, R. Carr, S. Currie, X. Ding, B. W. Filippone, a. García, P. Geltenbort, K. P. Hickerson, J. Hoagland, a. T. Holley, R. Hong, T. M. Ito, a. Knecht, C.-Y. Liu, J. L. Liu, M. Makela, R. R. Mammei, J. W. Martin, D. Melconian, S. D. Moore, C. L. Morris, a. Pérez Galván, R. Picker, M. L. Pitt, B. Plaster, J. C. Ramsey, R. Rios, a. Saunders, S. J. Seestrom, E. I. Sharapov, W. E. Sondheim, E. Tatar, R. B. Vogelaar, B. VornDick, C. Wrede, a. R. Young, and B. a. Zeck, “Precision measurement of the neutron β -decay asymmetry,” *Physical Review C*, vol. 87, p. 032501, Mar. 2013. pages 17
- [39] C. Johnson, F. Pleasonton, and T. Carlson, “Precision measurement of the recoil nergy spectrum from the decay of ${}^6\text{He}$,” *Physical Review*, vol. 132, p. 1149, 1963. pages 17
- [40] X. Fléchar, P. Velten, E. Liénard, A. Méry, D. Rodríguez, G. Ban, D. Durand, F. Mauger, O. Naviliat-Cuncic, and J. C. Thomas, “Measurement of the β - ν correlation coefficient $a_{\beta\nu}$ in the β decay of trapped ${}^6\text{He}^+$ ions,” *Journal of Physics G: Nuclear and Particle Physics*, vol. 38, p. 055101, May 2011. pages 17
- [41] O. Naviliat-Cuncic, “Vud from nuclear mirror transitions.” arXiv 1301.4153, 2013. pages 17
- [42] G. Li, R. Segel, N. D. Scielzo, P. F. Bertone, F. Buchinger, S. Caldwell, a. Chaudhuri, J. a. Clark, J. E. Crawford, C. M. Deibel, J. Fallis, S. Gulick, G. Gwinner, D. Lascar, a. F. Levand, M. Pedretti, G. Savard, K. S. Sharma,

- M. G. Sternberg, T. Sun, J. Van Schelt, R. M. Yee, and B. J. Zabransky, "Tensor Interaction Limit Derived From the α - β - $\bar{\nu}$ Correlation in Trapped ^8Li Ions," *Physical Review Letters*, vol. 110, p. 092502, Mar. 2013. pages 17
- [43] F. Wauters, *Search for tensor type weak currents by measuring the β -asymmetry parameter in nuclear decays*. PhD thesis, K.U. Leuven, 2009. pages 18, 31, 37
- [44] A. Kozela, G. Ban, A. Białek, K. Bodek, P. Gorel, K. Kirch, S. Kistryn, M. Kuźniak, O. Naviliat-Cuncic, J. Pulut, N. Severijns, E. Stephan, and J. Zejma, "Measurement of the Transverse Polarization of Electrons Emitted in Free-Neutron Decay," *Physical Review Letters*, vol. 102, p. 172301, May 2009. pages 18
- [45] A. Kozela, G. Ban, A. Białek, K. Bodek, P. Gorel, K. Kirch, S. Kistryn, O. Naviliat-Cuncic, N. Severijns, E. Stephan, and J. Zejma, "Measurement of the transverse polarization of electrons emitted in free neutron decay," *Physical Review C*, vol. 85, p. 045501, Apr. 2012. pages 18
- [46] T. Chupp, R. Cooper, K. Coulter, S. Freedman, B. Fujikawa, A. García, G. Jones, H. Mumm, J. Nico, A. Thompson, C. Trull, F. Wietfeldt, and J. Wilkerson, "Search for a T-odd, P-even triple correlation in neutron decay," *Physical Review C*, vol. 86, p. 035505, Sept. 2012. pages 18
- [47] M. Simson, F. A. Guardia, S. Baeßler, M. Borg, F. Glück, W. Heil, I. Konorov, G. Konrad, R. M. Horta, K. Leung, Y. Sobolev, T. Soldner, H.-F. Wirth, and O. Zimmer, "Measuring the proton spectrum in neutron decay—latest results with aspect," *Nuclear Instruments and Methods in Physics Research, Section A: Accelerators, Spectrometers, Detectors, and Associated Equipment*, vol. 611, pp. 203 – 206, 2009. pages 18
- [48] G. Konrad, F. Ayala Guardia, S. Baeßler, M. Borg, F. Glück, W. Heil, I. Konorov, K. Leung, R. Muñoz Horta, M. Simson, *et al.*, "The Proton Spectrum in Neutron Beta Decay: Latest Results with the aSPECT Spectrometer," *Nuclear Physics A*, vol. 827, no. 1-4, pp. 529c–531c, 2009. pages 18
- [49] K. Krane, "Dilute impurity hyperfine fields in Fe, Co, Ni, Gd," *Hyperfine Interactions*, vol. 16, pp. 1069–1079, 1983. 10.1007/BF02147421. pages 19
- [50] G. Rao, "Table of hyperfine fields for impurities in Fe, Co, Ni, Gd and Cr," *Hyperfine Interactions*, vol. 24, p. 1119, 1985. pages 19
- [51] W. Brewer, *Low-Temperature Nuclear Orientation*, ch. Nuclear orientation in non-magnetic metals, p. 407. North-Holland, Amsterdam, 1986. pages 19

- [52] K. Krane, *Low-Temperature Nuclear Orientation*, ch. Nuclear Orientation Formalism, p. 31. North-Holland, Amsterdam, 1986. pages 20, 25, 27
- [53] K. Krane, *Low-Temperature Nuclear Orientation*, ch. Coefficients for angular and polarization distribution functions, p. 982. North-Holland, Amsterdam, 1986. pages 21, 25
- [54] E. Klein, *Low-Temperature Nuclear Orientation*, ch. Relaxation phenomena, p. 579. North-Holland, Amsterdam, 1986. pages 22, 24
- [55] T. L. Shaw and N. J. Stone, "Nuclear spin-lattice relaxation attenuation coefficients for use in on-line nuclear orientation experiments," *Atomic Data and Nuclear Data Tables*, vol. 42, no. 2, pp. 339 – 363, 1989. pages 22, 25
- [56] D. Vénos, D. Zákoucký, and N. Severijns, "Spin-lattice relaxation attenuation coefficients for on-line nuclear orientation experiments," *Atomic Data and Nuclear Data Tables*, vol. 83, pp. 1–44, 2003. pages 25
- [57] V. V. Golovko, F. Wauters, S. Cottenier, M. Breitenfeldt, V. De Leebeek, S. Roccia, G. Soti, M. Tandecki, E. Traykov, S. Van Gorp, D. Zákoucký, and N. Severijns, "Hyperfine field and hyperfine anomalies of copper impurities in iron," *Physical Review C*, vol. 84, p. 014323, Jul 2011. pages 30
- [58] P. R. Locher, "Ratio of the magnetic dipole moments of ^{63}Cu and ^{65}Cu and the hyperfine-structure anomalies $^{63}\Delta^{65}$," *Phys. Rev. B*, vol. 10, pp. 801–804, Aug 1974. pages 30
- [59] P. Vingerhoets, K. T. Flanagan, M. Avgoulea, J. Billowes, M. L. Bissell, K. Blaum, B. A. Brown, B. Cheal, M. De Rydt, D. H. Forest, C. Geppert, M. Honma, M. Kowalska, J. Krämer, A. Krieger, E. Mané, R. Neugart, G. Neyens, W. Nörtershäuser, T. Otsuka, M. Schug, H. H. Stroke, G. Tungate, and D. T. Yordanov, "Nuclear spins, magnetic moments, and quadrupole moments of Cu isotopes from $n = 28$ to $n = 46$: Probes for core polarization effects," *Physical Review C*, vol. 82, p. 064311, Dec 2010. pages 30
- [60] S. Chikazumi, *Physics of magnetism*. J. Wiley and Sons, New York, 1964. pages 30
- [61] J. Wouters, *Onderzoek van de nucleaire structuur met behulp van anisotrope α emissie*. PhD thesis, Katholieke Universiteit Leuven, 1989. pages 30

- [62] D. Vénos, G. Van Assche, N. Severijns, D. Srnka, and D. Zákoucký, “The behaviour of HPGe detectors operating at temperatures below 77 K,” *Nuclear Instruments and Methods in Physics Research, Section A: Accelerators, Spectrometers, Detectors, and Associated Equipment*, vol. 454, pp. 403–408, 2000. pages 30
- [63] D. Zákoucký, D. Srnka, D. Vénos, V. Golovko, I. Kraev, T. Phalet, P. Schuurmans, N. Severijns, B. Vereecke, and S. Versyck, “HPGe detectors for low-temperature nuclear orientation,” *Nuclear Instruments and Methods in Physics Research, Section A: Accelerators, Spectrometers, Detectors, and Associated Equipment*, vol. 520, pp. 80 – 83, 2004. Proceedings of the 10th International Workshop on Low Temperature Detectors. pages 30
- [64] H. Marshak, *Low-Temperature Nuclear Orientation*, ch. Nuclear Orientation Thermometry, pp. 769 – 820. North-Holland, Amsterdam, 1986. pages 31
- [65] S. Agostinelli, J. Allison, K. Amako, J. Apostolakis, H. Araujo, P. Arce, M. Asai, D. Axen, S. Banerjee, G. Barrand, F. Behner, L. Bellagamba, J. Boudreau, L. Broglia, A. Brunengo, H. Burkhardt, S. Chauvie, J. Chuma, R. Chytracsek, G. Cooperman, G. Cosmo, P. Degtyarenko, A. Dell’Acqua, G. Depaola, D. Dietrich, R. Enami, A. Feliciello, C. Ferguson, H. Fesefeldt, G. Folger, F. Foppiano, A. Forti, S. Garelli, S. Giani, R. Giannitrapani, D. Gibin, J. J. G. Cadenas, I. González, G. G. Abril, G. Greeniaus, W. Greiner, V. Grichine, A. Grossheim, S. Guatelli, P. Gumplinger, R. Hamatsu, K. Hashimoto, H. Hasui, A. Heikkinen, A. Howard, V. Ivanchenko, A. Johnson, F. W. Jones, J. Kallenbach, N. Kanaya, M. Kawabata, Y. Kawabata, M. Kawaguti, S. Kelner, P. Kent, A. Kimura, T. Kodama, R. Kokoulin, M. Kossov, H. Kurashige, E. Lamanna, T. Lampén, V. Lara, V. Lefebure, F. Lei, M. Liendl, W. Lockman, F. Longo, S. Magni, M. Maire, E. Medernach, K. Minamimoto, P. M. de Freitas, Y. Morita, K. Murakami, M. Nagamatu, R. Nartallo, P. Nieminen, T. Nishimura, K. Ohtsubo, M. Okamura, S. O’Neale, Y. Oohata, K. Paech, J. Perl, A. Pfeiffer, M. G. Pia, F. Ranjard, A. Rybin, S. Sadilov, E. D. Salvo, G. Santin, T. Sasaki, N. Savvas, Y. Sawada, S. Scherer, S. Sei, V. Sirotenko, D. Smith, N. Starkov, H. Stoecker, J. Sulikimo, M. Takahata, S. Tanaka, E. Tcherniaev, E. S. Tehrani, M. Tropeano, P. Truscott, H. Uno, L. Urban, P. Urban, M. Verderi, A. Walkden, W. Wander, H. Weber, J. P. Wellisch, T. Wenaus, D. C. Williams, D. Wright, T. Yamada, H. Yoshida, and D. Zschesche, “Geant4 - a simulation toolkit,” *Nuclear Instruments and Methods in Physics Research, Section A: Accelerators, Spectrometers, Detectors, and Associated Equipment*, vol. 506, no. 3, pp. 250 – 303, 2003. pages 33

- [66] Geant4 website <http://geant4.cern.ch>. pages 33, 34
- [67] “Geant4 physics reference manual.” <http://geant4.cern.ch/support/userdocuments.shtml>. pages 34, 35
- [68] H. Burkhardt, V. Grichine, P. Gumplinger, V. Ivanchenko, R. Kokoulin, M. Maire, and L. Urban, “Geant4 standard electromagnetic package for hep applications,” *IEEE Symposium Conference Record Nuclear Science 2004.*, vol. 3, no. C, pp. 1907–1910, 2004. pages 34
- [69] J. Apostolakis, V. M. Grichine, V. N. Ivanchenko, M. Maire, and L. Urban, “The recent upgrades in the "standard" electromagnetic physics package,” in *CHEP'06*, 2006. pages 34
- [70] S. Chauvie, S. Guatelli, V. Ivanchenko, F. Longo, A. Mantero, B. Mascialino, P. Nieminen, L. Pandola, S. Parlati, L. Peralta, M. Pia, M. Piergentili, P. Rodrigues, S. Saliceti, and A. Tndade, “Geant4 low energy electromagnetic physics,” in *Nuclear Science Symposium Conference Record, 2004 IEEE*, vol. 3, pp. 1881 –1885 Vol. 3, oct. 2004. pages 34
- [71] J. Sempau, E. Acosta, J. Baro, J. Fernández-Varea, and F. Salvat, “An algorithm for monte carlo simulation of coupled electron-photon transport,” *Nuclear Instruments and Methods in Physics Research, Section B: Beam Interactions with Materials and Atoms*, vol. 132, no. 3, pp. 377 – 390, 1997. pages 35
- [72] <https://twiki.cern.ch/twiki/bin/view/Geant4/LoweMigratedProcesses>. pages 35
- [73] S. Goudsmit and J. Saunderson, “Multiple Scattering of Electrons,” *Physical Review*, vol. 57, pp. 24–29, Jan. 1940. pages 35
- [74] H. W. Lewis, “Multiple scattering in an infinite medium,” *Physical Review*, vol. 78, pp. 526–529, Jun 1950. pages 35
- [75] J. Apostolakis, A. Bagulya, S. Elles, V. N. Ivanchenko, O. Kadri, M. Maire, and L. Urban, “The performance of the geant4 standard em package for lhc and other applications,” *Journal of Physics: Conference Series*, vol. 119, no. 3, p. 032004, 2008. pages 35
- [76] V. N. Ivanchenko, O. Kadri, M. Maire, and L. Urban, “Geant4 models for simulation of multiple scattering,” *Journal of Physics: Conference Series*, vol. 219, no. 3, p. 032045, 2010. pages 35

- [77] O. Kadri, V. Ivanchenko, F. Gharbi, and A. Trabelsi, "Incorporation of the goudsmit-saunderson electron transport theory in the geant4 monte carlo code," *Nuclear Instruments and Methods in Physics Research, Section B: Beam Interactions with Materials and Atoms*, vol. 267, no. 23-24, pp. 3624 – 3632, 2009. pages 35
- [78] J. Fernández-Varea, R. Mayol, J. Baró, and F. Salvat, "On the theory and simulation of multiple elastic scattering of electrons," *Nuclear Instruments and Methods in Physics Research Section B: Beam Interactions with Materials and Atoms*, vol. 73, pp. 447–473, Apr. 1993. pages 35
- [79] L. Urbán, "A model for multiple scattering in geant4," Tech. Rep. CERN-OPEN-2006-077, CERN, Dec 2006. pages 35
- [80] F. Salvat, A. Jablonski, and C. J. Powell, "ELSEPA - Dirac partial-wave calculation of elastic scattering of electrons and positrons by atoms, positive ions and molecules," *Computer Physics Communications*, vol. 165, pp. 157–190, Jan. 2005. pages 35
- [81] J. R. A. Pitcairn, D. Roberge, A. Gorelov, D. Ashery, O. Aviv, J. A. Behr, P. G. Bricault, M. Dombisky, J. D. Holt, K. P. Jackson, B. Lee, M. R. Pearson, A. Gaudin, B. Dej, C. Höhr, G. Gwinner, and D. Melconian, "Tensor interaction constraints from beta-decay recoil spin asymmetry of trapped atoms," *Physical Review C*, vol. 79, no. 1, p. 015501, 2009. pages 100
- [82] H. Daniel, "Shapes of Beta-Ray Spectra," *Reviews of Modern Physics*, vol. 40, pp. 659–672, July 1968. pages 100
- [83] F. Calaprice and B. Holstein, "Weak magnetism and the beta spectra of ^{12}B and ^{12}N ," *Nuclear Physics A*, vol. 273, pp. 301 – 325, 1976. pages 100
- [84] W. Kaina, V. Soergel, H. Thies, and W. Trost, "A new measurement of the weak magnetism term in the betaspectra of ^{12}B and ^{12}N ," *Physics Letters B*, vol. 70, pp. 411–414, Oct. 1977. pages 100
- [85] J. Camp, "Measurement of the beta spectral shapes of B^{12} and N^{12} ," *Physical Review C*, vol. 41, pp. 1719–1726, Apr. 1990. pages 100
- [86] F. P. Calaprice, W. Chung, and B. H. Wildenthal, "Calculation of recoil-order matrix elements for the beta decays of F^{20} and Na^{20} ," *Physical Review C*, vol. 15, pp. 2178–2186, Jun 1977. pages 100
- [87] L. Van Elmbt, J. Deutsch, and R. Prieels, "Measurement of the ^{20}F beta-spectrum: A low-energy test of the standard electro-weak gauge-model," *Nuclear Physics A*, vol. 469, pp. 531–556, Aug. 1987. pages 100

- [88] D. Hetherington, A. Alousi, and R. Moore, "The shape factor of the 20F beta spectrum," *Nuclear Physics A*, vol. 494, pp. 1–35, Mar. 1989. pages 100
- [89] H. Daniel, G. Kaschl, H. Schmitt, and K. Springer, "Shapes of Allowed and Unique First-Forbidden β -Ray Spectra: In114, K42, Rb86, Sr90, and Y90," *Physical Review*, vol. 136, pp. B1240–B1242, Dec. 1964. pages 101
- [90] K. Heyde, *Basic ideas and concepts in nuclear physics*. Institute of Physics Publishing, 1999. pages 101
- [91] D. Wilkinson, "Evaluation of beta-decay, Part I. The traditional phase space factors.," *Nuclear Instruments and Methods in Physics Research, Section A: Accelerators, Spectrometers, Detectors, and Associated Equipment*, vol. 275, pp. 378 – 386, 1989. pages 101, 103
- [92] D. Wilkinson, "Evaluation of beta-decay, Part II. Finite mass and size effects.," *Nuclear Instruments and Methods in Physics Research, Section A: Accelerators, Spectrometers, Detectors, and Associated Equipment*, vol. 290, pp. 509 – 515, 1990. pages 101, 103
- [93] D. Wilkinson, "Evaluation of beta-decay, Part V. The Z-independent outer radiative corrections for allowed decay.," *Nuclear Instruments and Methods in Physics Research, Section A: Accelerators, Spectrometers, Detectors, and Associated Equipment*, vol. 365, pp. 497 – 507, 1995. pages 101, 102, 103
- [94] D. Wilkinson, "Evaluation of beta-decay, Part VI. The Z-dependent outer radiative corrections for allowed decay.," *Nuclear Instruments and Methods in Physics Research, Section A: Accelerators, Spectrometers, Detectors, and Associated Equipment*, vol. 401, pp. 275 – 280, 1997. pages 101, 102, 103, 104, 105
- [95] F. Wauters, I. Kraev, D. Zákoucký, M. Beck, V. Golovko, V. Kozlov, T. Phalet, M. Tandecki, E. Traykov, S. V. Gorp, and N. Severijns, "A geant4 monte-carlo simulation code for precision β spectroscopy," *Nuclear Instruments and Methods in Physics Research, Section A: Accelerators, Spectrometers, Detectors, and Associated Equipment*, vol. 609, no. 2-3, pp. 156 – 164, 2009. pages 101
- [96] A. Sirlin, "General Properties of the Electromagnetic Corrections to the Beta Decay of a Physical Nucleon," *Physical Review*, vol. 164, pp. 1767–1775, Dec. 1967. pages 103
- [97] W. Jaus and G. Rasche, "Radiative corrections to $0^+ \rightarrow 0^+$ β transitions," *Physical Review D*, vol. 35, pp. 3420–3422, June 1987. pages 104

- [98] A. Sirlin, “Remarks concerning the $O(Z\alpha^2)$ corrections to Fermi decays, conserved-vector-current predictions, and universality,” *Physical Review D*, vol. 35, pp. 3423–3427, June 1987. pages 104
- [99] A. Sirlin and R. Zucchini, “Accurate Verification of the Conserved-Vector-Current and Standard-Model Predictions,” *Physical Review Letters*, vol. 57, pp. 1994–1997, Oct. 1986. pages 105
- [100] X. Mougeot, M.-M. Bé, C. Bisch, and M. Loidl, “Evidence for the exchange effect in the β decay of ^{241}Pu ,” *Physical Review A*, vol. 86, p. 042506, Oct. 2012. pages 105
- [101] R. Brun and F. Rademakers, “ROOT - An object oriented data analysis framework,” *Nuclear Instruments and Methods in Physics Research Section A: Accelerators, Spectrometers, Detectors and Associated Equipment*, vol. 389, pp. 81–86, Apr. 1997. <http://root.cern.ch/drupal>. pages 108
- [102] F. James, “The interpretation of errors.” <http://seal.cern.ch/documents/minuit/mnerror.ps>, 2004. pages 109
- [103] M. Z. M.J. Berger, J.S. Coursey and J. Chang, “Stopping-power and range tables for electrons, protons, and helium ions.” 2005. pages 112
- [104] N. Kudomi, “Energy calibration of plastic scintillators for low energy electrons by using Compton scatterings of γ rays,” *Nuclear Instruments and Methods in Physics Research, Section A: Accelerators, Spectrometers, Detectors, and Associated Equipment*, vol. 430, pp. 96–99, June 1999. pages 117
- [105] K. Lojek, K. Bodek, and M. Kuzniak, “Ultra-thin gas detector for tracking of low energy electrons,” *Nuclear Instruments and Methods in Physics Research, Section A: Accelerators, Spectrometers, Detectors, and Associated Equipment*, vol. 611, pp. 284 – 288, 2009. pages 118, 119
- [106] C. Cook, L. Langer, and H. Price, “Study of the Beta-Spectra of C14 and S35,” *Physical Review*, vol. 74, pp. 548–552, Sept. 1948. pages 122
- [107] S. Warshaw, “The β -Spectrum of C14,” *Physical Review*, vol. 80, pp. 111–112, Oct. 1950. pages 122
- [108] A. Moljk and S. Curran, “Beta Spectra of C14 and S35,” *Physical Review*, vol. 96, pp. 395–398, Oct. 1954. pages 122
- [109] V. V. Kuzminov and N. J. Osetrova, “Precise measurement of ^{14}C beta spectrum by using a wall-less proportional counter,” *Physics of Atomic Nuclei*, vol. 63, pp. 1292–1296, July 2000. pages 122

- [110] P. Maris, J. Vary, P. Navrátil, W. Ormand, H. Nam, and D. Dean, "Origin of the Anomalous Long Lifetime of ^{14}C ," *Physical Review Letters*, vol. 106, p. 202502, May 2011. pages 122
- [111] D. Robson, "A new cluster model interpretation of the anomalous lifetime of ^{14}C ," *The European Physical Journal A*, vol. 47, p. 95, Aug. 2011. pages 122

List of publications

- *Recoil terms in allowed nuclear β decays between mirror and triplet nuclei*
V. De Leebeek; T. Porobic; G. Soti, F. Wauters; N. Severijns
to be submitted to **Physical Review C**
- *Measurement of the ^{67}Cu β -asymmetry parameter*
G. Soti; F. Wauters; M. Breitenfeldt; P. Finlay; A. Knecht; U. Koster;
I.S. Kraev; T. Porobic; I.S. Towner; Zákoucký, D; N. Severijns
to be submitted to **Physical Review C**
- *Performance of Geant4 in simulating particle detector response in the energy range below 1 MeV*
G. Soti; F. Wauters; M. Breitenfeldt; P. Finlay; A. Knecht; I.S. Kraev; T. Porobic, V; D. Zákoucký; N. Severijns
accepted for publication in **Nuclear Instruments and Methods, Section A**
- *Magnetic Dipole Moment of the Doubly-Closed-Shell Plus One Proton Nucleus ^{49}Sc*
Ohtsubo, T.; Stone, N.; Stone, J.; Towner, I.; Bingham, C.; Gaulard, C.; Köster, U.; Muto, S.; Nikolov, J.; Nishimura, K.; Simpson, G.; Soti, G.; Veskovic, M.; Walters, W.; Wauters, F.
Physical Review Letters 109 (2012) 032504
- *Hyperfine field and hyperfine anomalies of copper impurities in iron*
Golovko, V. V.; Wauters, F.; Cottenier, S.; Breitenfeldt, M.; De Leebeek, V.; Roccia, S; Soti, G.; Tandecki, M.; Traykov, E; Van Gorp, S.; Zakoucky, D; Severijns, N.
Physical Review C 84 (2011) 014323
- *A compact radio frequency quadrupole for ion bunching in the WITCH experiment*
Traykov, E; Beck, M; Breitenfeldt, M; Delahaye, P; De Leebeek, V;

Friedag, P; Herlert, A; Geeraert, N; Heirman, W; Lønne, P.-I; Mader, J; Roccia, S; Soti, G; Tandecki, M; Timmermans, M; Thiboud, J; Van Gorp, S; Wauters, F; Weinheimer, C; Zákoucký, D; Severijns, N.

Nuclear Instruments and Methods, Section A 648 (2011)

- *Computer controls for the WITCH experiment*
Tandecki, M.; Beck, D; Beck, M; Brand, H; Breitenfeldt, M.; De Leebeeck, V.; Friedag, P; Herlert, A; Kozlov, V; Mader, J; Roccia, S.; Soti, G.; Traykov, E; Van Gorp, S.; Wauters, F; Weinheimer, Ch; Zakoucky, D; Severijns, N.
Nuclear Instruments and Methods, Section A 629 (2011) 396-405
- *SIMBUCA, using a graphics card to simulate Coulomb interactions in a Penning trap*
Van Gorp, S.; Breitenfeldt, M.; De Leebeeck, V.; Roccia, S.; Soti, G.; Tandecki, M.; Traykov, E.; Wauters, F.; Beck, M.; Friedag, P.; Mader, J.; Weinheimer, C.; Herlert, A.; Kozlov, V.; Zakoucky, D.; Iitaka, T.; Severijns, N.
Nuclear Instruments and Methods, Section A 638 (2011) 192-200
- *Half-life of ^{221}Fr in Si and Au at 4 K and at millikelvin temperatures*
Wauters, F.; Verstichel, B.; Breitenfeldt, M.; De Leebeeck, V.; Kozlov, V. Yu.; Kraev, I.; Roccia, S.; Soti, G.; Tandecki, M.; Traykov, E.; Van Gorp, Simon; Zakoucky, D.; Severijns, N.
Physical Review C 82 (2010) 064317
- *Precision measurements of the ^{60}Co β -asymmetry parameter in search for tensor currents in weak interactions*
Wauters, F; Kraev, I; Zákoucký, D; Beck, M; Breitenfeldt, M; De Leebeeck, V; Golovko, V. V; Kozlov, V. Yu; Phalet, T; Roccia, S; Soti, G; Tandecki, M; Towner, I. S; Traykov, E; Van Gorp, S; Severijns, N.
Physical Review C 82 (2010) 055502

FACULTY OF SCIENCE
DEPARTMENT OF PHYSICS AND ASTRONOMY
NUCLEAR AND RADIATION PHYSICS
Celestijnenlaan 200D box 2418
B-3001 Heverlee

